

Copyright is owned by the Author of the thesis. Permission is given for a copy to be downloaded by an individual for the purpose of research and private study only. The thesis may not be reproduced elsewhere without the permission of the Author.

Pattern Formation in Electrically Coupled  
Pacemaker Cells

A thesis presented in partial fulfillment of the  
requirements for the degree of

Doctor of Philosophy

in

Mathematics

at Massey University, Manawatū,  
New Zealand.

Hammed Olawale Fatoyinbo

عبد الحميد أولاولي فتوينبو

December 2020

# Dedication

To my wife

*Rashidat Omowunmi Ajala*

and daughter

*Labeebah Anjolaoluwa Hammed*

# Acknowledgements

All praises are to Allah who tells us: “*Then remember Me; I will remember you. Be grateful to Me, and do not reject Me.*” (Surah Al-Baqarah: 152)

I express my sincere thanks to Dr. Richard G. Brown, Dr. David J. W. Simpson and Assoc. Prof. Bruce van Brunt for supervising this research, and for their advice, suggestions and feedback throughout this research.

I am grateful to Prof. Hinke Osinga (University of Auckland) for her financial support and help during my visit to her research group. Our discussion improved my understanding of bifurcation analysis. I also appreciate Dr. Andrus Giraldo Munoz (University of Auckland) for his help with numerical computation in AUTO.

Thanks to my parents and siblings for their prayers and support over the years. Thanks to my wife, Rashidat O. Ajala, for her advice and encouragement for all matters. She also helped me with the proofreading of my work. Also to my daughter, Labeebah A. Hammed, thank you for making me happy always. I am greatly indebted to the Raheem family and Adeyinkas for their unconditional support.

I also want to express my appreciation to my friends and colleagues: Abidemi Afeez, Christian Offen, Muhammad Al-Sultani, Michael McVeagh, Sishu Shankar Muni, Abdulquadri Alaka, Reny Sam Kuruvila and a host of others. I would also like to thank the Massey Muslim Society, Nigerian Community in Palmerston North and African Students Association at Massey University.

Finally, I want to thank the School of Fundamental Sciences, Massey University for funding my research and financial support to attend local and international conferences.

# Published Work

**Fatoyinbo, H.O.**, Brown, R.G., Simpson, D.J.W., & van Brunt, B. Numerical Bifurcation Analysis of Pacemaker Dynamics in a Model of Smooth Muscle Cells. *Bull. Math. Biol.* 82, 95 (2020). <https://doi.org/10.1007/s11538-020-00771-6>

# Conference Presentations

## Contributed Talks

1. Stability of Travelling Waves in a Model of Pacemaker Cells. ANZIAM Conference 2021.
2. Stability Analysis of Traveling Wave Solutions in a Model of Coupled Pacemaker Cells, NZ Math and Stat Postgraduate Conference 2020. ([Abstract](#)).
3. Spatiotemporal Dynamics in Spontaneous Excitable Cells. SMB Annual Meeting (Online) 2020. ([Abstract](#)).
4. Spatiotemporal Pattern Formation in a Model of Electrically Coupled Smooth Muscle Cells. ANZIAM Conference 2020.
5. Spatiotemporal Pattern Formation in a Model of Electrically Coupled Smooth Muscle Cells. NZMS Colloquium 2019. ([Slides](#)).
6. Emergence of Spatiotemporal Patterns in Pacemaker Coupled Excitable Cells. NZMS Colloquium 2018. ([Slides](#)).
7. Pattern Formation in Pacemaker Dynamics of Coupled Excitable Cells. NZ Math and Stat Postgraduate Conference 2018.

## Poster Presentations

1. Stability of Travelling Waves in Electrically Coupled Smooth Muscle Cells. SMB 2021 ([Abstract](#))
2. Spatiotemporal Chaos: Complex Dynamics in a Model of Coupled Smooth Muscle Cells. Dynamics Days Europe (Online) 2020. ([poster](#))
3. Spatiotemporal Pattern Formation in a Model of Electrically Coupled Smooth Muscle Cells. NZMS 2019 (won **second** prize). ([poster](#))

# Abstract

In this thesis we study electrical activity in smooth muscle cells in the absence of external stimulation. The main goal is to analyse a reaction-diffusion system that models the dynamical behaviour where adjacent cells are coupled through passive electrical coupling. We first analyse the dynamics of an isolated muscle cell for which the model consists of three first-order ordinary differential equations. The cell is either excitable, nonexcitable, or oscillatory depending on the model parameters. To understand this we reduce the model to two equations, nondimensionalise, then perform a detailed numerical bifurcation analysis of the nondimensionalised model. One parameter bifurcation diagrams reveal that even though there is no external stimulus the cell can exhibit two fundamentally distinct types of excitability. By computing two-parameter bifurcation diagrams we are able to explain how the cell transitions between the two types of excitability as parameters are varied.

We then study the full reaction-diffusion system first through numerical integration. We show that the system is capable of exhibiting a wide variety of spatiotemporal behaviours such as travelling pulses, travelling fronts, and spatiotemporal chaos. Through a linear stability analysis we are able to show that the spatiotemporal patterns are not due to diffusion-driven instability as is often the case for reaction-diffusion systems. It is as a consequence of the nonlinear dynamics of the reaction terms and coupling effect of diffusion. The precise mechanism is not yet well understood, this will be subject of future work. We then examine travelling wave solutions in detail. In particular we show how they relate to homoclinic and heteroclinic solutions in travelling wave coordinates. Finally we review spectral stability analysis for travelling waves and compute the essential spectrum of travelling waves in our system.



# List of Figures

1.1	(a) Spot patterns on the Amur leopard, <i>Panthera pardus orientalis</i> . Reproduced from (Warby, 2015) (b) Wind ripples in sand dunes. Reproduced from (BLMCalifornia, 2012) (c) Pigmentation patterns on seashell, <i>oliva porphyria</i> . Reprinted by permission from Springer Nature from (Meinhardt, 2003) . . . .	2
1.2	Examples of Turing patterns: (A) Spot pattern. (B) Stripe pattern. (C) Hole pattern. (D-F) The Turing patterns shown in 3D form corresponding to patterns A-C. Reproduced from (Xu et al., 2017). . . . .	3
1.3	A crosssectional view of an arterial wall showing the three layers: the intima, SMCs and endothelial cells (ECs), where $p$ is the pressure normal to the vessel wall and $\tau$ is the shear stress. Reprinted by permission from Springer Nature from (Hahn and Schwartz, 2009). . . . .	4
1.4	Classification of ion channels. Reproduced from (Ratan, 2018). . . . .	6
1.5	A schematic representation of an action potential . . . . .	7
1.6	The equivalent circuit representation of a cell membrane with $n$ ion channels. . . . .	8
1.7	Phase planes showing the dynamics of the fast activation variable $V$ and the slow variable $N$ before, at, and after the saddle-node on an invariant circle (SNIC) bifurcation. . . . .	12
1.8	Phase planes showing the dynamics of the fast activation variable $V$ and the slow variable $N$ before, at, and after the Hopf bifurcation. . . . .	13

1.9	(a) The snapshot of the $\alpha$ -profile for (I) travelling front; (II) travelling pulse; (III) chaotic response (b) Space-time plot of the reactant $\alpha$ for four different parameter values. Reproduced from (Merkin et al., 1996) with permission from the Royal Society of Chemistry. . . . .	17
1.10	(a) Snapshots of the membrane potentials of gap junction-coupled $80 \times 80$ class $I^*$ neurons for different values of the gap junction strength (b) Space-time plot of membrane potentials of 20 neurons of class $I^*$ with the two neighbors by gap junctions. The vertical and horizontal directions indicate respectively the neuron position, and the time. Reprinted from (Fujii and Tsuda, 2004) with permission from Elsevier. . . . .	19
1.11	The switching sequences of spatiotemporal patterns in layers I and II. Both layers are initially in the STC state. Panel (a) and (b) differ by randomly initial conditions. Reprinted with permission from (Hartle and Wackerbauer, 2017). Copyright (2020) by the American Physical Society. . . . .	21
1.12	Spatiotemporal dynamics for bidirectional synaptic coupling between in layers I and II. Example for (a) a swapping event; (b) reinitiation of STC; and (c) a fast switching sequence. Reprinted with permission from (Hartle and Wackerbauer, 2017). Copyright (2020) by the American Physical Society . . . . .	21
2.1	Equivalent circuit representation of cell membrane with three ionic channels.	26
2.2	Schematic representation of a smooth muscle cell coupled electrically to adjacent cells through gap junctions. . . . .	26
2.3	The plots of $n_\infty$ against $Ca_i$ for three different values of the membrane potential $v$ . . . . .	29

2.4	Time series of (2.1.1)–(2.1.8) for the (a) membrane potential, (b) fraction of opening $K^+$ channels, (c) potassium and calcium currents and (d) free cytoplasmic calcium concentration with initial conditions, $(v, n, Ca_i) = (-50\text{mV}, 0, 0\text{nM})$ , and parameter values in Table 2.1. . . . .	32
2.5	Time series of the membrane potential $v$ when the three conductances are blocked. The parameters used are those of Table 2.2 except (a) the leak channel is blocked ( $g_L = 0$ ); (b) the $Ca^{2+}$ channel is blocked ( $g_{Ca} = 0$ ); (c) the $K^+$ channel is blocked ( $g_K = 0$ ). . . . .	33
2.6	Time series of the membrane potential $v$ for (a) $v_1 = -35\text{mV}$ ; (b) $v_1 = -25\text{mV}$ ; (c) $v_1 = -19\text{mV}$ . Other parameters as in Table. 2.1. . . . .	34
2.7	Time series of the membrane potential $v$ for (a) $v_6 = -35\text{mV}$ ; (b) $v_6 = -25\text{mV}$ ; (c) $v_6 = -2\text{mV}$ . Other parameters as in Table. 2.1. . . . .	34
2.8	A plot of $v_3(\text{mV})$ against time for solutions to (2.1.1)–(2.1.8) with the parameters of Table 2.1. . . . .	36
2.9	Time series of the membrane potential $v$ for $v_1$ (a) $v_1 = -35\text{mV}$ ; (b) $v_1 = -25\text{mV}$ ; (c) $v_1 = -19\text{mV}$ . Other parameters as in Table. 2.2. . . . .	37
2.10	Time series of the membrane potential $v$ for (a) $v_3 = -31\text{mV}$ ; (b) $v_3 = -21\text{mV}$ ; (c) $v_3 = 2\text{mV}$ . Other parameters as in Table. 2.2. . . . .	37
2.11	Time series of the membrane potential $V$ for nondimensionalised model (2.2.6)–(2.2.7) with the parameters values in Table 2.2. . . . .	41
2.12	Time evolution of the membrane potential $V$ for (a) $\bar{v}_1 = -0.4375$ ; (b) $\bar{v}_1 = -0.3125$ ; (c) $\bar{v}_1 = -0.2375$ . Other parameters as in Table. 2.2. . . . .	41

2.13	Time evolution of the membrane potential $V$ for (a) $\bar{v}_3 = -0.3875$ ; (b) $\bar{v}_3 = -0.2625$ ; (c) $\bar{v}_3 = 0.025$ . Other parameters as in Table. 2.2. . . . .	42
2.14	(a) The $(V, N)$ phase plane for the nondimensionalised model (2.2.6)–(2.2.7) with parameters as in Table. 2.2. The blue curve is a stable periodic orbit. The magenta and orange curves are the nullclines for $V$ and $n$ . The black curves are the solution trajectories. The red circle is unstable equilibrium. . . . .	45
2.15	The $(V, N)$ phase plane for the nondimensionalised model (2.2.6)–(2.2.7) with (a) $\bar{v}_1 = -0.4375$ ; (b) $\bar{v}_1 = -0.3125$ ; (c) $\bar{v}_1 = -0.25$ ; The blue and red curve is a stable periodic orbit. The magenta and orange curves are the nullclines for $V$ and $N$ . The black curves are the solution trajectories. The blue and red circles are stable and unstable equilibria. The red and green curves in (c) are the stable and unstable manifolds of the saddle point. Other parameters as in Table. 2.2. . . . .	47
2.16	The $(V, N)$ phase plane for the nondimensionalised model (2.2.6)–(2.2.7) with (a) $\bar{v}_3 = -0.3875$ ; (b) $\bar{v}_3 = -0.2625$ ; (c) $\bar{v}_3 = 0.025$ ; The blue curve is a stable periodic orbit. The magenta and orange curves are the nullclines for $V$ and $N$ . The black curves are the solution trajectories. The blue and red circles are stable and unstable equilibria. Other parameters as in Table. 2.2. . . . .	48

3.1	Bifurcation diagrams of (a) the full model (2.1.1)–(2.1.8) with $v_1$ as the bifurcation parameter, (b) the reduced model (2.2.1)–(2.2.2) with $v_1$ as the bifurcation parameter and (c) the nondimensionalised model (2.2.6)–(2.2.7) with $\bar{v}_1$ as the bifurcation parameter. The remaining parameter values are given in Tables 2.1 and 2.2. Panel (d) shows the period of the oscillations in Fig. 3.1c for the nondimensionalised model. Black [magenta] curves correspond to equilibria [limit cycles]. Solid [dashed] curves correspond to stable [unstable] solutions. HB: Hopf bifurcation; SN: saddle-node bifurcation (of an equilibrium); SNC: saddle-node bifurcation of a limit cycle; SNIC: saddle-node on an invariant circle bifurcation. . . . .	59
3.2	(a) A bifurcation diagram of the nondimensionalised model (2.2.6)–(2.2.7) with $\bar{v}_3$ as the bifurcation parameter and other parameter values as given in Table 2.2. (b) A plot of the periodic oscillations as a function of parameter $\bar{v}_3$ . The labels and other conventions are as in Fig. 3.1. . . . .	60
3.3	A bifurcation diagram of the nondimensionalised model (2.2.6)–(2.2.7) with (a) $\psi$ ; (b) $\bar{v}_L$ as the bifurcation parameter, and other parameter values as given in Table 2.2. The labels and other conventions are as in Fig. 3.1. . . .	61
3.4	A two-parameter bifurcation diagram of the nondimensionalised model (2.2.6)–(2.2.7) in the $(\bar{v}_1, \bar{v}_3)$ -plane for the parameter values of Table 2.2. The values of $\bar{v}_3$ in $l_1, l_2, l_3, l_4, l_5$ and $l_6$ are 0.45, 0.25, $-0.047$ , $-0.088$ , $-0.26$ and $-0.32$ , respectively. The black curves are the loci of codimension-one bifurcations labelled as follows: HB: Hopf bifurcation, SN: saddle-node bifurcation (or SNIC), HC: homoclinic bifurcation, and SNC: saddle-node bifurcation of limit cycle. The labels for the codimension-two bifurcations are explained in Table 3.2. The invariant sets that exist in each region are listed in Table 3.3. . . .	63

3.5	(a) An enlargement of Fig. 3.4 showing lines $l_1$ and $l_2$ . The filled diamond is a Bogdanov-Takens bifurcation. (b) A one-parameter bifurcation diagram along $l_1$ with $\bar{v}_3 = 0.45$ . (c) A one-parameter bifurcation diagram along $l_2$ with $\bar{v}_3 = 0.25$ . HB: Hopf bifurcation, SN: saddle-node bifurcation, SNC: saddle-node bifurcation of a limit cycle, HC: homoclinic bifurcation. . . . .	66
3.6	(a) An enlargement of Fig. 3.4 showing lines $l_3$ and $l_4$ . The filled circle is a non-central saddle-node homoclinic bifurcation. (b) A one-parameter bifurcation diagram along $l_3$ with $\bar{v}_3 = -0.047$ . (c) A one-parameter bifurcation diagram along $l_4$ with $\bar{v}_3 = -0.088$ . HB: Hopf bifurcation, SN: saddle-node bifurcation, SNC: saddle-node bifurcation of a limit cycle, SNIC: saddle-node on an invariant circle bifurcation, HC: homoclinic bifurcation. . . . .	68
3.7	A phase portrait of the nondimensionalised model (2.2.6)–(2.2.7) on line $l_3$ at $\bar{v}_3 = -0.047$ showing tristability. The blue and red curves are stable and unstable limit cycles. The magenta and orange curves are the nullclines for $N$ and $V$ . The black curves are the solution trajectories. The blue and red circles are stable and unstable equilibria. . . . .	69
3.8	(a) An enlargement of Fig. 3.4 showing lines $l_5$ and $l_6$ (b) An enlargement of panel (a). (c) A one-parameter bifurcation diagram along $l_5$ with $\bar{v}_3 = -0.26$ . (d) An enlargement of panel (c). HB: Hopf bifurcation, SN: saddle-node bifurcation, SNC: saddle-node bifurcation of a limit cycle. . . . .	70
3.9	A one-parameter bifurcation diagram along $l_6$ with $\bar{v}_3 = -0.32$ (shown in Figs. 3.4 and 3.8a). HB: Hopf bifurcation. . . . .	71

3.10	A two-parameter bifurcation diagram of the nondimensionalised model (2.2.6)–(2.2.7) in the $(\bar{v}_1, \bar{v}_L)$ -plane. Other parameter values as in Table 2.2; (b) and (c) are enlargements of Fig. 3.10a. The labels and conventions are as in Fig. 3.4, Table 3.2 and Table 3.3. . . . .	73
3.11	Further bifurcation diagrams of (2.2.6)–(2.2.7). The values of the remaining parameters as in Table 2.2. . . . .	75
3.12	A two-parameter bifurcation diagram of the nondimensionalised model (2.2.6)–(2.2.7) in the $(\bar{g}_{Ca}, \bar{g}_L)$ -plane. Other parameter values as in Table 2.2; The labels and conventions are as in Fig. 3.4, Table 3.2 and Table 3.3. . . . .	76
3.13	Bifurcation diagrams of (2.2.6)–(2.2.7) with other parameter values as given in Table 2.2. Solid (dashed) black curves represent stable (unstable) steady states. Solid (dashed) magenta curves denote the stable (unstable) limit cycles. HB: Hopf bifurcation, SNC: saddle-node of limit cycles. . . . .	77
3.14	A two-parameter bifurcation diagram of the nondimensionalised model (2.2.6)–(2.2.7) in the $(\bar{v}_1, \bar{v}_3)$ -plane. Other parameter values as in Table 2.2; (b) is enlargement of (a). The labels and conventions are as in Fig. 3.4, Table 3.2 and Table 3.3. . . . .	78
4.1	(a) Space-time plot of the membrane potential $V$ ; (b)–(d) Spatial distribution of $V$ at times $\tau = 2, 20, 250$ . The parameter values are as in Table 2.2. . . .	88
4.2	Space-time plots of the membrane potential $V$ . (b)–(g): $\bar{v}_1 = -0.325, -0.265, -0.25, -0.248, -0.240, \text{ and } -0.230$ , respectively. Other parameters are fixed as in Table 2.2. . . . .	91

4.3	Spatial distribution of the membrane potential $V$ for times $\tau = 3, 15, 50, 125, 250, 500$ in Fig. 4.2e. . . . .	92
4.4	Space-time plots of the membrane potential $V$ . (b)–(g): $\bar{v}_3 = -0.3462, -0.3019, -0.2813, -0.23842, -0.1725,$ and $-0.05565,$ respectively. Other parameters are fixed as in Table 2.2. . . . .	94
4.5	Space-time plots of the membrane potential $V$ . (b)–(g): $\psi = 0.1, 0.12, 0.13, 0.2, 0.3,$ and $0.5,$ respectively. Other parameters are fixed as in Table 2.2. The solution transitions from propagating pulses travelling in opposite direction to complex spatiotemporal patterns to fronts travelling in opposite direction. . . . .	96
4.6	Solution profiles at time $\tau = 300$ showing the transitions from travelling pulses to spatiotemporal chaos and to fronts. . . . .	97
4.7	Space-time plots of the membrane potential $V$ . (a)–(f): $\bar{v}_1 = -0.325, -0.265, -0.25, -0.248, -0.246,$ and $-0.245,$ respectively. Other parameters are fixed as in Table 2.2 and $\epsilon = 0.025.$ . . . . .	99
4.8	Space-time plot of the membrane potential $V$ at $\bar{v}_1 = -0.255$ with a straight line as the initial perturbation. . . . .	100
4.9	Space-time plot of the membrane potential $V$ for simulation time $\tau = 1000$ at $\psi = 0.12$ with a straight line as the initial perturbation. . . . .	100
4.10	Space-time plots of the membrane potential $V$ with two Gaussian pulses centered at $X = \pm 1,$ respectively. (a)–(f): $\bar{v}_1 = -0.325, -0.265, -0.250, -0.248, -0.240,$ and $-0.230,$ respectively. Other parameters are fixed as in Table 2.2. . . . .	102



4.11	Space-time plots of the membrane potential $V$ for simulation time $\tau = 500$ with two Gaussian pulses centred at $X = \pm 1$ , respectively. (a)–(f): $\psi = 0.1, 0.12, 0.13, 0.2, 0.3,$ and $0.5$ , respectively. Other parameters are fixed as in Table 2.2. The solution transitions from propagating pulses travelling in opposite direction to complex spatiotemporal patterns to fronts travelling in opposite direction. . . . .	103
4.12	Space-time plots of the membrane potential $V$ for simulation time $\tau = 500$ at $\psi = 0.2$ with two Gaussian pulses centered at (a) $X = \pm 1$ with distance between the point sources $\rho_{\text{diff}} = 2$ ; (b) $X = \pm 2$ with distance between the point sources $\rho_{\text{diff}} = 4$ . . . . .	104
5.1	A schematic diagram showing three different types of travelling waves and their corresponding trajectories in the phase space of the TWODE system. The black dots correspond to equilibria. . . . .	109
5.2	(a) The solution profile of (2.2.6)–(2.2.7) and the travelling pulse $V(\zeta)$ with $c = 0.006116$ (b) Corresponding homoclinic trajectory representing the pulse in (a) connecting the asymptotic state $(V, W, N) = (-0.7148, 0, 0.001764)$ to itself in the $(V, W, N)$ phase space. The parameters are $\psi = 0.1, D = 0.0001, c = 0.006116$ . . . . .	111
5.3	(a) The solution profile of (2.2.6)–(2.2.7) and travelling front $V(\zeta)$ with $c = 0.006116$ (b) Corresponding heteroclinic trajectory representing the front in (a) connecting the asymptotic state $(V, W, N) = (-0.2935, 0, 0.1559)$ to $(V, W, N) = (-0.7148, 0, 0.001764)$ in the $(V, W, N)$ phase space. The parameters are $\psi = 0.1, D = 0.0001, c = 0.006116$ . . . . .	113

5.4	$V$ and $N$ nullclines for the nondimensionalised model (2.2.6)–(2.2.7) at $\bar{v}_1 = -0.225$ . Magenta and black curves represent the $V$ -nullcline, and $N$ -nullcline, respectively. The blue and red filled circles are the steady states, A (stable), B and C (unstable). Other parameter values as in Table 2.2. . . . .	122
5.5	Essential spectra of steady states A, B, and C for $\bar{v}_1 = -0.225$ with $c = 0.006116$ .	124
5.6	(a)–(b) Essential spectrum of steady state C for $\bar{v}_1 = -0.45$ with $c = 0.006116$ .	124
5.7	(a) A travelling pulse solution (b) The essential spectrum of the pulse with wave speed $c = 0.006116$ and $D = 0.0001$ . . . . .	125
5.8	(a) A travelling front that connects homogeneous steady states $V = -0.2891$ to $V = -0.7141$ . (b)–(c) Essential spectra of the front for asymptotic state $P_-$ and $P_+$ with wave speed $c = 0.0043$ . . . . .	127
5.9	(a) A space-time plot of modulated front to (2.2.6)–(2.2.7) at $(\bar{v}_1, \psi) = (-0.2466, 0.3)$ (b) The essential spectrum of the front for asymptotic state $P_-$ . . . . .	128

# List of Tables

2.1	Model parameter values are taken from Gonzalez-Fernandez and Ermentrout (1994). . . . .	30
2.2	Parameter values for the nondimensionalised model (2.2.6)–(2.2.7). . . . .	40
2.3	Definition of the nondimensional model variables and parameters. . . . .	40
2.4	Classification of equilibrium in planar systems . . . . .	43
3.1	Abbreviations and notations of codimension-one bifurcations. . . . .	58
3.2	Abbreviations and notations of codimension-two bifurcations. . . . .	62
3.3	A summary of the eight different combinations of equilibria and limit cycles that arise in Fig. 3.4 and its magnifications, Figs. 3.5a, 3.6a, 3.8a, and 3.8b. . . . .	64

# Contents

<b>Dedication</b>	<b>i</b>
<b>Acknowledgements</b>	<b>ii</b>
<b>Publications</b>	<b>iii</b>
<b>Conference Presentations</b>	<b>iv</b>
<b>Abstract</b>	<b>vi</b>
<b>List of Figures</b>	<b>vii</b>
<b>List of Tables</b>	<b>xvii</b>
<b>1 Introduction</b>	<b>1</b>
1.1 Pattern Formation . . . . .	1
1.2 Excitability and Action Potentials . . . . .	4
1.3 Conductance-Based Models . . . . .	7
1.4 Wave Propagation in Excitable Media . . . . .	11
1.5 Examples of Spatiotemporal Patterns in Excitable Media . . . . .	15
1.5.1 Wave-induced Chaos in an Autocatalytic Chemical System . . . . .	15

1.5.2	Chaotic Itinerancy in Type I Neurons . . . . .	18
1.5.3	Spatiotemporal Chaos in Synaptically Coupled Neurons . . . . .	19
1.6	Aims and Outline of the Thesis . . . . .	22
<b>2</b>	<b>A Mathematical Model for Pacemaker Dynamics in Smooth Muscle Cells</b>	<b>24</b>
2.1	Model Formulation . . . . .	27
2.2	Dynamics of an Isolated Smooth Muscle Cell . . . . .	30
2.2.1	Model reduction . . . . .	35
2.2.2	Nondimensionalisation . . . . .	38
2.3	Linear Stability and Phase Plane Analyses . . . . .	42
2.3.1	Linear Stability Analysis of Equilibria . . . . .	42
2.3.2	Phase Plane Analysis . . . . .	44
2.4	Discussion . . . . .	50
<b>3</b>	<b>Transitions between Types of Excitability</b>	<b>52</b>
3.1	Numerical Continuation and Bifurcation Techniques . . . . .	52
3.1.1	An Introduction to Bifurcation Theory . . . . .	53
3.2	Codimension-One Bifurcation Analysis . . . . .	57
3.3	Codimension-Two Bifurcation Analysis . . . . .	61
3.3.1	Bifurcations in $(\bar{v}_1, \bar{v}_3)$ -plane . . . . .	62

3.3.2	Bifurcations in $(\bar{v}_1, \bar{v}_L)$ -plane . . . . .	69
3.4	Effect of Ion Conductances on Pacemaker Dynamics . . . . .	72
3.4.1	Pacemaker Dynamics in the Absence of Leak Conductance . . . . .	76
3.5	Discussion . . . . .	78
<b>4</b>	<b>Analysis of Coupled Model</b>	<b>80</b>
4.1	Linear Stability Analysis . . . . .	80
4.2	Numerical Method . . . . .	84
4.2.1	Boundary Conditions . . . . .	85
4.2.2	Initial Conditions . . . . .	86
4.3	Numerical Simulations . . . . .	87
4.3.1	Spatiotemporal Patterns with varying $\bar{v}_1$ . . . . .	89
4.3.2	Spatiotemporal Patterns with varying $\bar{v}_3$ . . . . .	90
4.3.3	Spatiotemporal Patterns with varying $\psi$ . . . . .	93
4.3.4	Effect of Changing the Initial Perturbation . . . . .	95
4.3.5	Simulations with Two-Point Source . . . . .	98
4.4	Discussion . . . . .	101
<b>5</b>	<b>Travelling Wave Analysis of the Reaction-Diffusion System</b>	<b>106</b>
5.1	Existence of Travelling Waves via Wave Speed Analysis . . . . .	106

5.2	Stability Analysis of Travelling Waves . . . . .	112
5.2.1	Spectral Analysis . . . . .	114
5.2.2	Spectra of Different Wave Types . . . . .	117
5.2.3	Model Analysis . . . . .	119
5.3	Discussion . . . . .	128
<b>6</b>	<b>Conclusion</b>	<b>130</b>
6.1	Future Work . . . . .	133
	<b>References</b>	<b>134</b>
<b>A</b>	<b>Appendix</b>	<b>146</b>
A.1	Statement of Contribution . . . . .	146
A.2	AUTO-07p Code . . . . .	147
A.3	MATLAB Code . . . . .	151

# 1. Introduction

In this work we discuss spatiotemporal pattern formation in electrically coupled smooth muscle cells under the influence of changes in transmural pressure, that is, the pressure gradient across the vessel wall. In this chapter, we briefly review pattern formation mechanisms and summarise how the spatial patterns observed in nature are reproduced in experiments and mathematical models.

In Sec. 1.2 we give overview of excitable cells, in particular the smooth muscle cell, and discuss relevant electrophysiological processes including excitability and an action potential. Then in Sec. 1.3 we review conductance based models, and provide some classical models. Coupling of adjacent cells in excitable media via reaction-diffusion system adjacent cells is discussed in Sec. 1.4. In Sec. 1.5 we review existing reaction-diffusion models with similar unusual patterns observed in our numerical simulations. Finally the thesis outline is provided in Sec. 1.6.

## 1.1 Pattern Formation

Pattern formation is a developmental process through which complex structures and shapes form in nature. Examples of the resulting spatial patterns include complex patterning of animal coats (Murray, 2003), wind ripples in sand dunes (Chaplain et al., 1999), and geometric designs on seashells (Meinhardt, 2003), see Fig. 1.1. Several experiments have been performed to reproduce these patterns and mathematical models have been used to numerically replicate patterning processes. The main type of mathematical model used to generate spatial patterns is a *reaction-diffusion* system. The framework for pattern formation theory originates with Alan Turing's seminal paper "*The Chemical Basis of Morphogenesis*" (Turing, 1952). In his research, he applied a reaction-diffusion system to explain how



diffusion-driven instability in chemical reactions under certain conditions result in nonhomogeneous spatial patterns now known as *Turing patterns*. Although Turing's work was initially criticised, some years later De Kepper's group in France experimentally confirmed his hypothesis (De Kepper et al., 1991). They observed Turing-type spatial patterns in the chemical oscillatory reaction known as the Belousov-Zhabotinsky reaction.

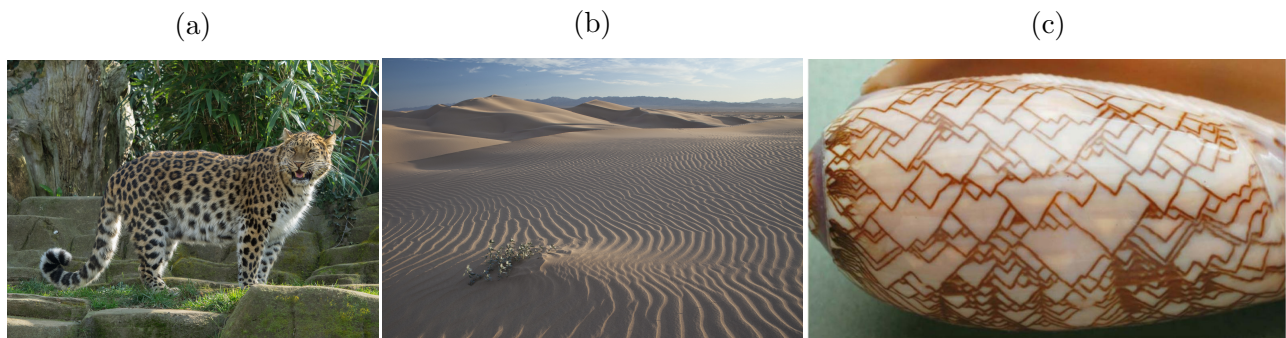


Figure 1.1: (a) Spot patterns on the Amur leopard, *Panthera pardus orientalis*. Reproduced from (Warby, 2015) (b) Wind ripples in sand dunes. Reproduced from (BLMCalifornia, 2012) (c) Pigmentation patterns on seashell, *oliva porphyria*. Reprinted by permission from Springer Nature from (Meinhardt, 2003)

Subsequently, pattern formation has received great interest and Turing patterns have been observed in many interdisciplinary studies. In ecology, the popular Lotka-Volterra model for two interacting species exhibits both Turing and non-Turing patterns when a diffusion term is incorporated in the model (Banerjee and Banerjee, 2012; Shi and Ruan, 2015; Liu et al., 2020). In epidemiology, spatial patterns have been observed in diffusive epidemic models designed to investigate the spread and control of infectious diseases (Jia et al., 2018; Chang et al., 2020). Various spatiotemporal patterns have been observed in cellular dynamics due to electrophysiological processes in cells and tissues (Izhikevich, 2007; Keener and Sneyd, 2009). Also, spatial patterns have been generated in a variety of physical and mechanical systems (Paul et al., 2003; Perez-Londoño et al., 2010). Turing patterns include stripes, hexagons, spirals, spots, spheres, see Fig. 1.2.

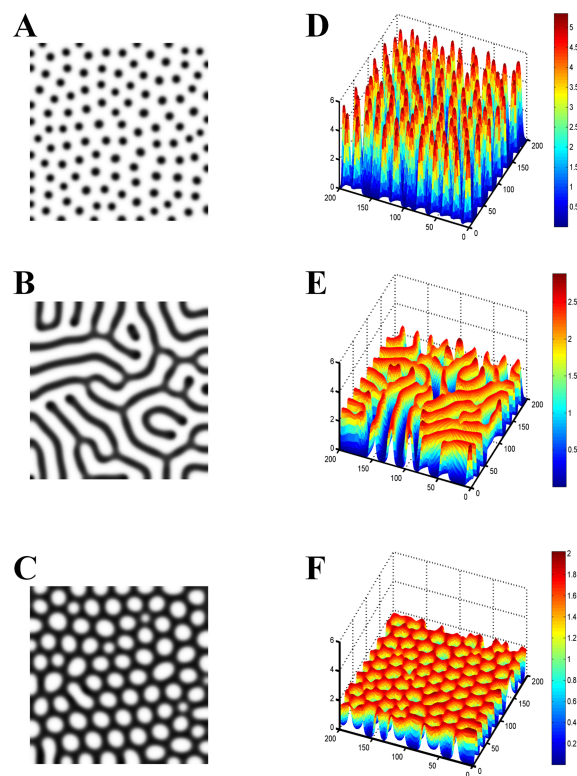


Figure 1.2: Examples of Turing patterns: (A) Spot pattern. (B) Stripe pattern. (C) Hole pattern. (D-F) The Turing patterns shown in 3D form corresponding to patterns A-C. Reproduced from (Xu et al., 2017).

## 1.2 Excitability and Action Potentials

Cellular dynamics refer to the behavior of cells in living organisms. The cells are classified as excitable (examples include neurons, muscle, and some endocrine cells) or non-excitable (such as fibroblasts and adipocytes). The interactions among these cells result in different cellular and biological processes such as cell organisation (Murray, 2003), secretion of hormones and T-cell activation (Keener and Sneyd, 2009), muscle contraction (Shaikh et al., 2011), and cell signalling (Izhikevich, 2007). Excitable cells have the ability to be electrically excited when subject to a stimulus. During the course of this research, we explored the dynamical behaviour of excitable cells, in particular smooth muscle cells.

Smooth muscle cells (SMCs) are widely spread across various organs and tubes in the body. For example, they are found in arteries, blood vessels, veins, and urinary tracts. An artery is a functional unit in cardiovascular system which helps to regulate blood flow. Its wall consists of three main layers: the intima (outer layer), SMCs (middle layer), and endothelial cells (inner layer). Fig. 1.3 is a cross-sectional view of an arterial wall showing the three layers.

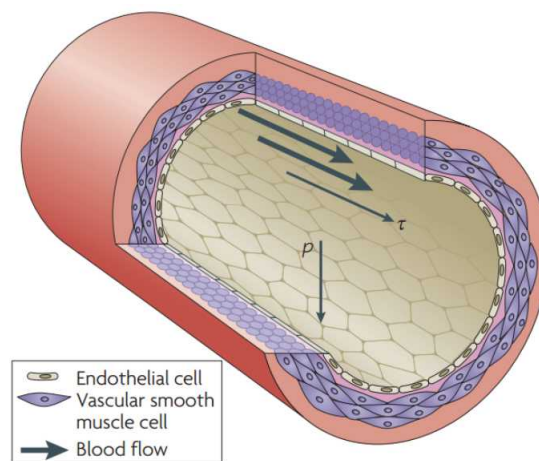


Figure 1.3: A crosssectional view of an arterial wall showing the three layers: the intima, SMCs and endothelial cells (ECs), where  $p$  is the pressure normal to the vessel wall and  $\tau$  is the shear stress. Reprinted by permission from Springer Nature from (Hahn and Schwartz, 2009).

Moreover, just like the other cell types (neurons, endocrine, and skeletal cells) the SMC, when stimulated by an external stimulus, can generate a large electrical signal and contracts in response. The tendency of a cell to respond to a stimulus in this way is referred to as *excitability*. A detailed understanding of excitability requires knowledge of the relevant electrophysiological processes, and these have been widely studied in neuroscience, and other related disciplines (Sneyd et al., 1995; Koenigsberger et al., 2004; Ermentrout and Terman, 2008; Shaikh et al., 2011; McCobb and Zeeman, 2016).

The cell membrane of a SMC separates solutions of different ions from its internal and external environments. These include calcium ions ( $\text{Ca}^{2+}$ ), potassium ions ( $\text{K}^+$ ), sodium ions ( $\text{Na}^+$ ), chloride ions ( $\text{Cl}^-$ ), and organic anions ( $\text{OA}^-$ ). These ions flow in and out of the cell membrane through membrane proteins known as ion channels. Ion channels come in a variety of different forms. The most common types of ion channel in the cell membrane are the gated and leak channels. Most of the gated ion channels are highly selective, so they allow only specific types of ion to pass through, while the leak channels are non-selective. For example, the sodium channels are only permeable to  $\text{Na}^+$ . The gated channels are classified into three sub-types: ligand-gated channels, voltage-gated channels, and mechanically-gated channels, see Fig. 1.4.

All gated channels change from an open state to a closed state, and vice-versa, in response to stimuli. The ligand-gated channels open or close in response to the binding of a ligand, which is a chemical messenger such as a neurotransmitter. The activation of the voltage-gated ion channels is regulated by changes in the voltage across the membrane. The mechanically-gated channels are activated in response to mechanical stimuli or pressure.

The concentrations of  $\text{K}^+$  and  $\text{OA}^-$  inside the cell are higher than on the outside. In contrast, the concentrations of  $\text{Ca}^{2+}$  and  $\text{Cl}^-$  are higher on the outside than on the inside. The difference in the concentrations between the outside and inside of the cell results in a concentration gradient which determines the resting membrane potential of the cell membrane

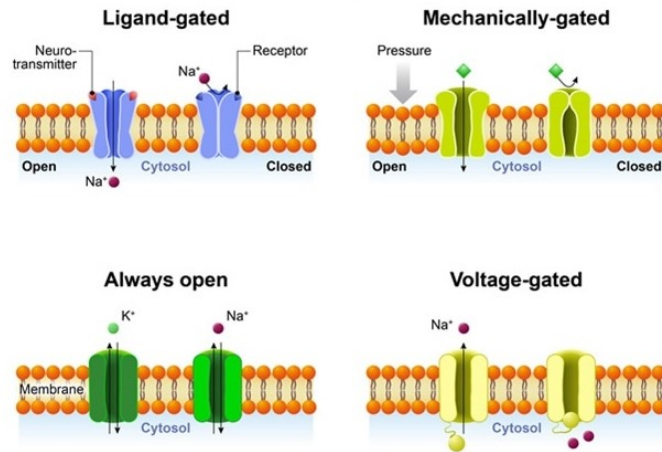


Figure 1.4: Classification of ion channels. Reproduced from (Ratan, 2018).

(McCobb and Zeeman, 2016). The passage of ions through the voltage-gated ion channels leads changes in the membrane potential. A positive feedback effect from voltage-gated channels can lead to a spike in voltage known as an action potential. During this process, the membrane potential is rapidly depolarised, then repolarised as the ion permeabilities change with the opening and closing of ion channels. When the membrane is highly permeable to  $\text{Ca}^{2+}$ , there is influx of  $\text{Ca}^{2+}$  and the membrane potential becomes more positive than it is at the resting potential, hence the membrane is depolarised. When the membrane is highly permeable to  $\text{K}^{+}$ , there is efflux of  $\text{K}^{+}$  which leads to the repolarisation of the cell. At some point, the membrane potential becomes more negative than it is at the resting potential and the membrane is hyperpolarised such that it will not respond to any stimuli until when it is back to the resting potential. The period of hyperpolarisation is known as the refractory period. Fig. 1.5 shows different phases of an action potential during excitability.

During the electrophysiological process, another cellular event that may occur is the propagation of the action potential along the vessel wall. The propagation of action potential plays a vital role in cell to cell communication between SMCs. The excitation of a particular SMC may trigger action potentials in neighbouring SMCs as a result of spatial propagation of action potential. In this research, we will be considering electrical coupling among

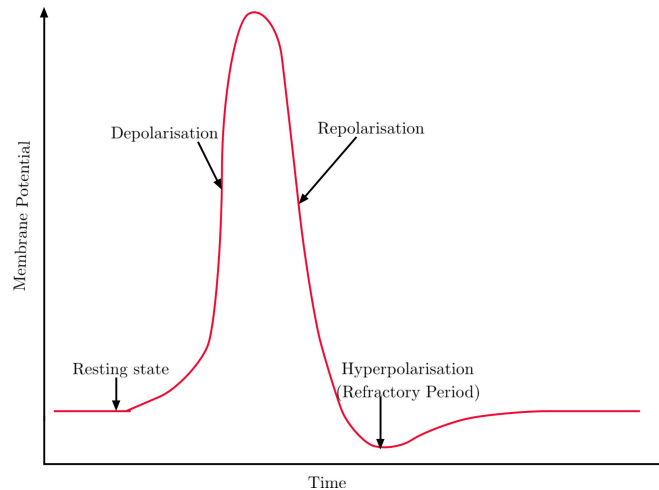


Figure 1.5: A plot of an action potential. It shows different stages in the production of an action potential.

SMCs through gap junctions, the intercellular channels that allow passage of ions between connected cells. To understand the dynamics of the action potential and its properties in excitable cells the activity of the cell membrane can be interpreted as an electrical circuit. The set-up of the cell membrane as an electric circuit and its mathematical description is discussed in the next section.

### 1.3 Conductance-Based Models

The electrophysiological activities in the cell membrane of an excitable cell are often described as an electric circuit. This representation is called the *conductance-based model*. The cell membrane acts as an electrical insulator with resistance and capacitance, thus it is modelled as a capacitor in parallel with a number of resistors. The equivalent circuit representation of cell membrane with  $n$  types of ionic channels is shown in Fig. 1.6.

The dynamics of the conductance-based model is governed by Kirchhoff's law. This says that the total current, flowing across the cell membrane is the sum of the membrane capacitive

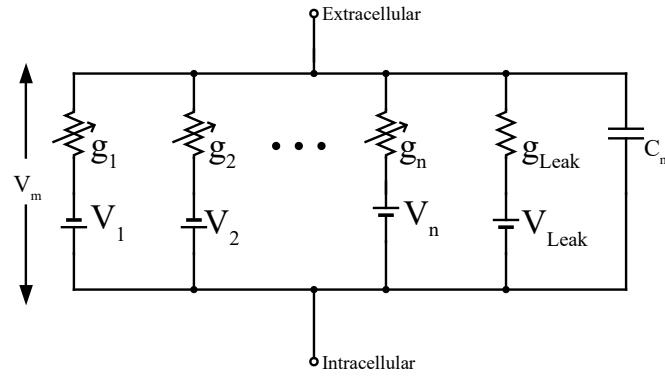


Figure 1.6: The equivalent circuit representation of cell membrane with  $n$  ion channels.  $g_i$  and  $V_i$  are the  $i$ -th maximal conductance and reversal potential of ionic channels, where  $i = 1, 2, \dots, n$ .  $C_m$  is the cell membrane capacitance.  $g_{\text{Leak}}$  and  $V_{\text{Leak}}$  are the maximal conductance and reversal potential for the leak channel

current and all the ionic currents, defined as:

$$I_{\text{app}} = C \frac{dV}{dt} + I(V, P_j), \quad (1.3.1)$$

where  $I_{\text{app}}$  is the total membrane current,  $C$  is the membrane capacitance,  $V$  is the membrane potential,  $P_j$  is the  $j$ -th gating variable (i.e. the fraction of open  $j$ -th ion channels) and

$$I(V, P_j) = \sum_i g_i Q_i (V - V_i), \quad (1.3.2)$$

where  $g_i$  is the maximal conductances for the  $i$ -th ionic currents,  $V_i$  is the reversal potentials ion  $i$ , the voltage at which there is no net flow of a particular ion from the internal and external part of the cell membrane. When there is no external applied current,  $I_{\text{app}} = 0$ , and that is the case we are interested in . Finally,  $Q_i$ , the proportion of open  $i$ -th channels is defined to be:

$$Q_i = m_i^a h_i^b, \quad (1.3.3)$$

where  $m_i$  is the probability that activation gate is in open state (sometimes denoted by  $n$  for  $\text{K}^+$ ),  $h_i$  is the probability that inactivation gate is in open state,  $a$  is the number of

activation gates and  $b$  is the number of inactivation gates per channels (Izhikevich, 2007). The activation and inactivation gates control the electrical conductance of ion channels. For the leak currents,  $Q = 1$  since the leak channels are independent of voltage. The equation for the gating variables is of the form:

$$\frac{dP_j}{dt} = \omega(V) \left( \tilde{P}_j(V) - P_j \right), \quad (1.3.4)$$

where  $\omega(V)$  is a rate constant,  $\tilde{P}_j(V)$  is an activation function that corresponds to the fraction of  $j$ -th ion channels that are open at steady state.

Many mathematical models have been developed to describe the behaviour of SMCs and other excitable cells. The pioneering Hodgkin-Huxley model, developed by A. L. Hodgkin and A. F. Huxley (1952), concerned electrical impulses along a squid giant axon. This model consists of two voltage-dependent channels,  $\text{Na}^+$  and  $\text{K}^+$  and the leak channels which are voltage independent. Consequently the model consists of four first-order differential equations with the current equation defined as:

$$I_{app} = C \frac{dV}{dt} + g_K n^4 (V - V_K) + g_{\text{Na}} m^3 h (V - V_{\text{Na}}) + g_L (V - V_L), \quad (1.3.5)$$

while the equations for the gating variables are similar to (1.3.4). Comparing (1.3.5) to (1.3.3), the Hodgkin-Huxley model has a  $\text{K}^+$  channel with four  $\text{K}^+$  activation gates, and a  $\text{Na}^+$  channel with three activation and one inactivation  $\text{Na}^+$  gates. Their investigation showed that the squid giant axon responds to electrical stimuli by generating an action potential due to changes in membrane potential with respect to alteration of ions through the ionic channels.

The Hodgkin-Huxley model laid the foundation for other biological neuron models. FitzHugh and Nagumo developed a two dimensional model which is a simplified prototype of Hodgkin-Huxley model (Fitzhugh, 1961; Nagumo et al., 1962). Another variant of Hodgkin-Huxley



model is the Morris-Lecar model which was developed to model the excitability of a barnacle giant muscle fiber (Morris and Lecar, 1981). The model has two voltage-dependent channel types like the squid giant axon, but in this case, they are  $\text{Ca}^{2+}$  and  $\text{K}^+$  channels, neither of which inactivates. Thus, for the Morris-Lecar model, the current equation is given as:

$$I_{app} = C \frac{dV}{dt} + g_K n (V - V_K) + g_{\text{Na}} m (V - V_{\text{Ca}}) + g_L (V - V_L), \quad (1.3.6)$$

this model has two gating variables, one each for the  $\text{Ca}^{2+}$  and  $\text{K}^+$  channels respectively, and the gating variables equations are similar to (1.3.4). Other well known models include the Connor-Stevens model (Connor and Stevens, 1971), the Wang-Buzsaki model (Wang and Buzsáki, 1996).

In any of these models, if there are no additional current sources like the electrode injected current, that is  $I_{app} = 0$ , then excitability is absent. But it has been shown that some excitable cells sometimes can spontaneously become excitable and elicit self-sustained (periodic) oscillations. Such dynamics are referred to as *pacemaker dynamics* (González-Miranda, 2014). The spontaneous excitability of such systems is the motivation for this research. Specifically, we will explore pacemaker dynamics in a prototype of the Morris-Lecar model with no induced current.

Excitability plays important role in understanding electrophysiological activity in excitable cells. It is associated with mode of transitions from excitable state to periodic oscillations. Hodgkin (1948) classified excitability into type I and II on the onset of oscillations. He described the differences based on the frequency-current relationship, for type I the frequency curve is continuous and discontinuous for type II. Mathematically, Rinzel and Ermentrout (1999) used bifurcation theory to distinguish between the types of excitability. They showed that periodic oscillation in type I excitability arises via a saddle-node on invariant circle (SNIC) bifurcation, and in the type II excitability the periodic oscillation arises via a Hopf

bifurcation. It has been established in many studies that the Morris-Lecar model (1981) exhibits both types excitability depending on how the physiological parameters are varied (references).

The Morris-Lecar model consists of two variables, a fast activation variable  $V$  and a slower variable  $N$ . The dynamical behaviour of the model is explained through the interaction of the two variables, this can be visualised by plotting  $V$  against  $N$  in the phase space. The intersection of the  $V$ - and  $N$ -nullclines corresponds to the equilibrium point, that is, the point in the phase space where  $V$  and  $N$  are constant.

In type I excitability, the  $V$ - and  $N$ -nullclines intersect at three points, corresponding to the three equilibria of the system, one stable denoted by A (sink), and two unstable denoted by B (saddle point) and C (source), respectively. Stimulation moves the  $V$ -nullcline up, thus pushing the equilibria A and B closer to one another. Increasing the stimulation, the two equilibria A and B collide and disappear at a saddle-node bifurcation, and an infinite period limit cycle appears. These dynamics are shown in Fig. 1.7.

In type II excitability, the  $V$ - and  $N$ -nullclines intersect at one point, corresponding to a unique equilibrium. This equilibrium is a spiral sink (i.e stable). Stimulation moves the  $V$ -nullcline upward, thus the equilibrium loses stability and appears a small amplitude limit cycle through a Hopf bifurcation. Further increasing the stimulation causes the amplitude of oscillation to grow. These dynamical behaviours are shown in Fig. 1.8

## 1.4 Wave Propagation in Excitable Media

Signals generated by cell excitation can propagate spatially through the cell population. This gives rise to what is known mathematically as a *travelling wave*. Intercellular communication between neighbouring cells is important in a vast number of physiological processes, for

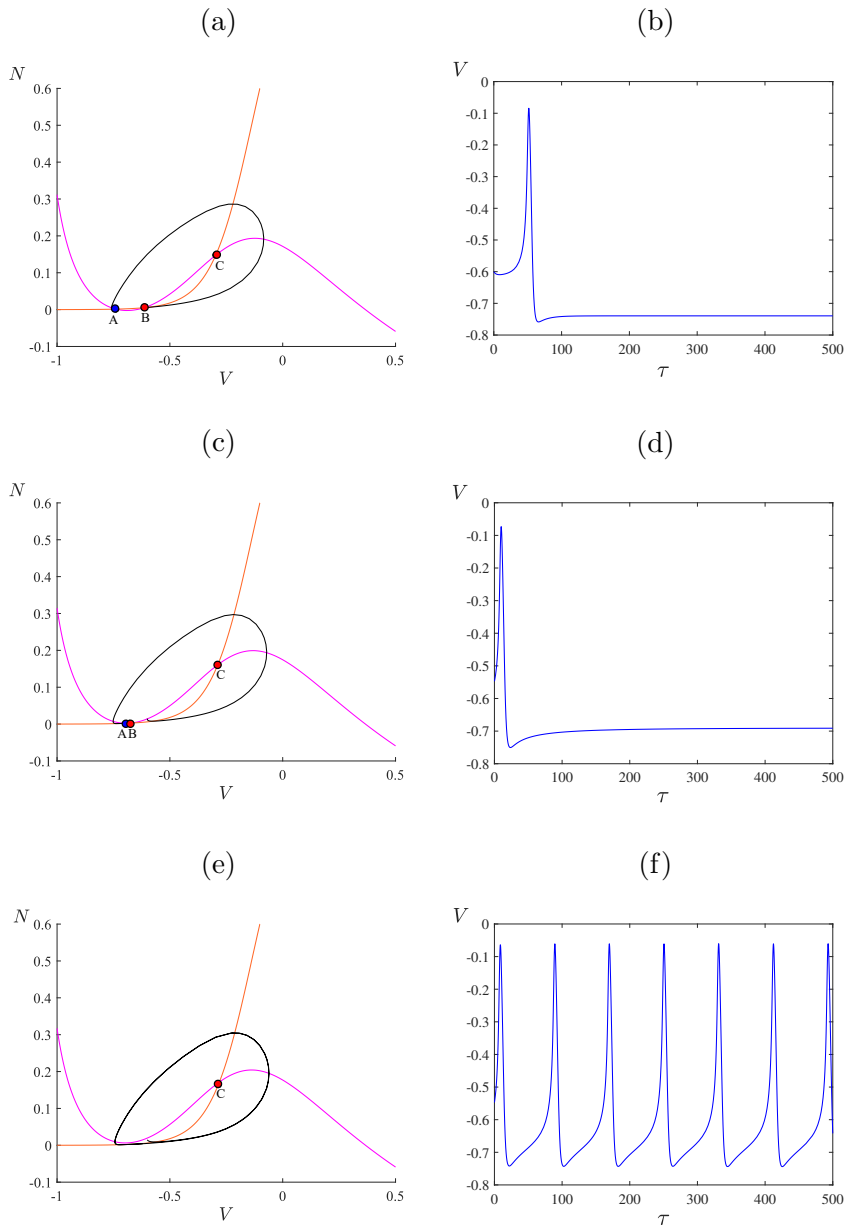


Figure 1.7: Phase planes showing the dynamics of the fast activation variable  $V$  and the slow variable  $N$  before, at, and after the saddle-node on an invariant circle (SNIC) bifurcation.

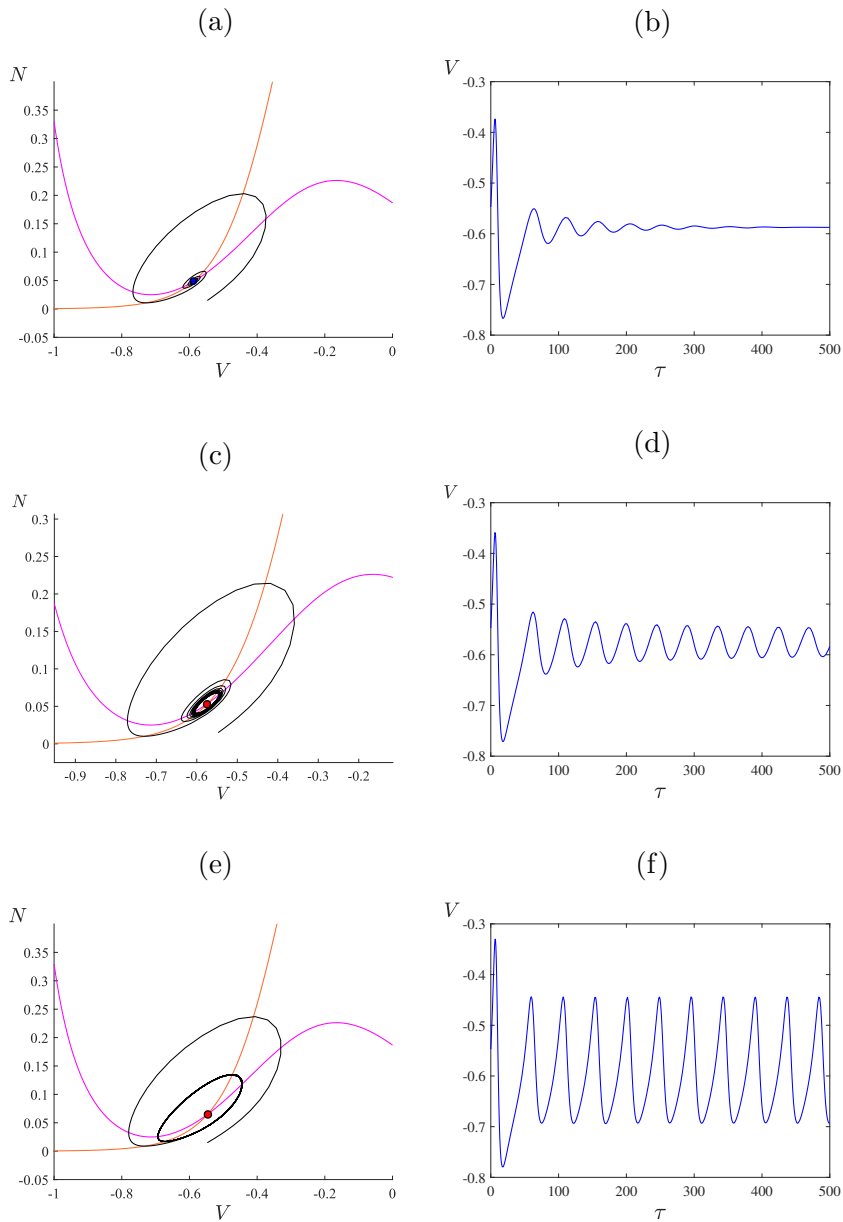


Figure 1.8: Phase planes showing the dynamics of the fast activation variable  $V$  and the slow variable  $N$  before, at, and after the Hopf bifurcation.

example propagation of signals through the vessel wall of SMCs causes vasomotion, the contraction and relaxation of the blood vessel wall, which regulates blood flow across the cell population.

The process of communication between neighbouring cells of an excitable medium via local coupling is diffusion-like, hence this nonlinear dynamical behaviour can be represented mathematically in the form of a reaction-diffusion system. Reaction-diffusion systems are parabolic partial differential equations (PDEs) consisting of diffusion and reaction terms. They are of the form:

$$\frac{\partial \mathbf{U}}{\partial t} = D \nabla^2 \mathbf{U} + \mathbf{g}(\mathbf{U}), \quad (1.4.1)$$

where  $\mathbf{U}(x, t)$  describes the state of the system,  $D$  is the matrix of diffusivities,  $\nabla^2$  is the Laplace operator, and  $\mathbf{g}(\mathbf{U})$ , captures the reaction kinetics.

Reaction-diffusion systems have been widely used as a framework for understanding pattern formation theory in many areas of research, for example: in chemistry, the Schnakenberg model (Schnakenberg, 1979); in ecology, the Holling-Tanner model (Banerjee and Banerjee, 2012); and the Fitzhugh-Nagumo model (Fitzhugh, 1961), among others. Examples of wave propagation observed in spatially excitable media are travelling fronts and pulses (in one-dimension), spiral waves (in two-dimensions) and scroll waves (in three-dimensions). Our interest is to study wave dynamics in an excitable reaction-diffusion system of pacemaker SMCs through electrical coupling, so we will briefly review some previous studies on wave propagation in spatially excitable media in next section.

## 1.5 Examples of Spatiotemporal Patterns in Excitable Media

Spatiotemporal patterns often arise in models of excitable media under the influence of small perturbations to a homogeneous steady state. The transition from a homogeneous steady state to a spatial patterns is an example of an instability or bifurcation. Stationary and complex patterns have been observed in many models of excitable media.

In this section we briefly review some results of spatiotemporal patterns in reaction-diffusion systems of excitable media. Our numerical results produce unusual spatial patterns, and so we surveyed the literature to find other examples that look like these. Here we focus on models that have spatiotemporal patterns similar to our results. Another interesting point is that they come from quite a wide array of disciplines. While different models involve vastly different reaction kinetics, the basic spatiotemporal behaviour observed through theoretical and numerical analysis is often similar. In particular we discuss the existence of irregular patterns in chemical systems and transitions between travelling pulses and spatiotemporal chaos in synaptically coupled neurons.

### 1.5.1 Wave-induced Chaos in an Autocatalytic Chemical System

The spatiotemporal patterns in a model for a continuous-flow unstirred reactor (CFUR) was examined by Merkin *et al.* (1996) through coupling of chemical reactions with molecular diffusion. The model is a representation of chemical feedback between two chemical species defined as reactant A and autocatalyst B. They assumed that the overall reactions can be described by cubic autocatalysis such that the model equations for the evolution of the

concentrations within the reactor in dimensionless form are given by

$$\frac{\partial \alpha}{\partial \tau} = \delta \nabla^2 \alpha + 1 - \alpha - \mu \alpha \beta^2, \quad (1.5.1a)$$

$$\frac{\partial \beta}{\partial \tau} = \nabla^2 \beta + \beta_0 - \phi \beta + \mu \alpha \beta^2, \quad (1.5.1b)$$

where  $\alpha$  and  $\beta$  are concentrations of the reactant A and autocatalyst B,  $\delta$  is the ratio of diffusion coefficients, and  $\mu$ ,  $\beta_0$  and  $\phi$  are constants. In one spatial dimension,  $\nabla^2 = \frac{\partial^2}{\partial x^2}$ . Equations (1.5.1a)–(1.5.1b) are subjected to zero-flux boundary conditions

$$\frac{\partial \alpha}{\partial x} = \frac{\partial \beta}{\partial x} = 0; \text{ at } x = 0 \text{ and } x = x_0, \quad (1.5.2)$$

and initial conditions

$$\alpha(x, \tau = 0) = 1; \text{ for all } x, \quad (1.5.3a)$$

$$\beta(x, \tau = 0) = 0; \text{ for } \sigma < x < x_0$$

$$\beta(x, \tau = 0) = g_0(x); \text{ for } 0 < x < \sigma, \quad (1.5.3b)$$

with typically,  $g_0 = 1$  for  $0 < x < \sigma$ .

Numerical simulations of system (1.5.1a)–(1.5.1b) in one spatial dimension produce different spatiotemporal behaviours including propagating fronts and pulses, and irregular spatiotemporal patterns. A front solution is observed whenever the value of  $\mu$  is greater than a certain saddle-node bifurcation and, connects the stable steady state  $(\alpha_{ss}^0, \beta_{ss}^0) = (1, 0)$  to another steady state  $(\alpha_{ss}^+, \beta_{ss}^+)$ . A pulse solution connects  $(\alpha_{ss}^0, \beta_{ss}^0)$  to itself. Examples of these are shown in Fig. 1.9a. Merkin and Sadiq (1996) explored in detail the properties of the travelling fronts and pulses over a wider parameter range. For values of  $\mu$  beyond a Hopf bifurcation,  $(\alpha_{ss}^+, \beta_{ss}^+)$  is unstable. In this case a propagating front from  $(\alpha_{ss}^0, \beta_{ss}^0)$  to  $(\alpha_{ss}^+, \beta_{ss}^+)$  is observed but the system returns back towards the stable state  $(\alpha_{ss}^0, \beta_{ss}^0)$  in some region

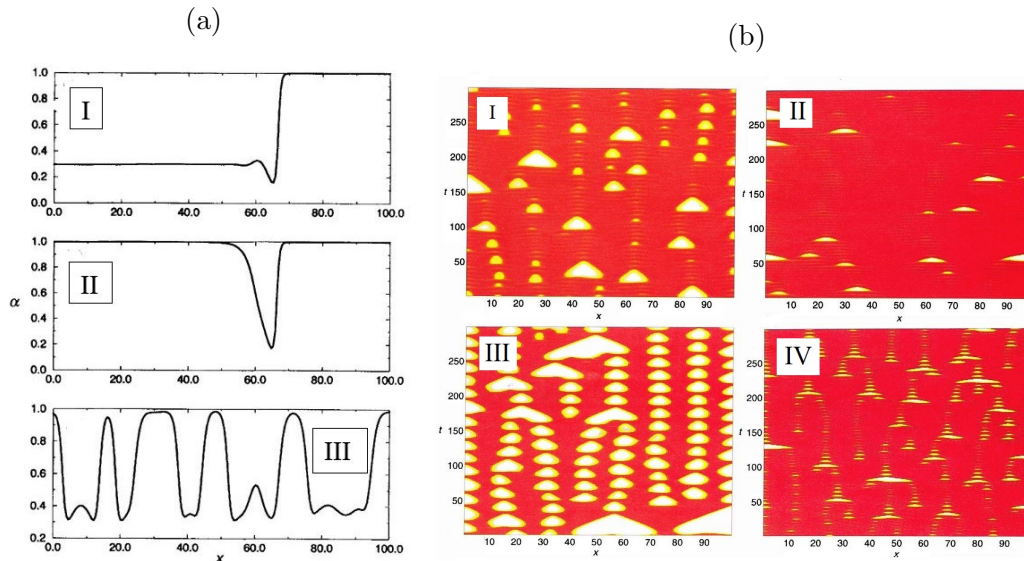


Figure 1.9: (a) The snapshot of the  $\alpha$ -profile for (I) travelling front; (II) travelling pulse; (III) chaotic response (b) Space-time plot of the reactant  $\alpha$  for four different parameter values. Reproduced from (Merkin et al., 1996) with permission from the Royal Society of Chemistry.

and this initiates further reaction-diffusion fronts propagating back to  $(\alpha_{ss}^0, \beta_{ss}^0)$ . Repetition of this process at different regions in the domain can be interpreted as the cause for irregular spatiotemporal patterns in the system. Fig. 1.9a III shows a snapshot of such behaviour.

Fig. 1.9b shows the long term behaviour of the reactant  $\alpha$  for four different parameter values. The white and red regions correspond to high and low concentrations of  $\alpha$ , respectively. The white regions are values close to the  $(\alpha_{ss}^0, \beta_{ss}^0)$  state. For Fig. 1.9b I, III and IV, the system is far from the Hopf bifurcation so the steady state  $(\alpha_{ss}^+, \beta_{ss}^+)$  has a strong repulsive effect. This causes the system to evolve back rapidly to the vicinity of  $(\alpha_{ss}^0, \beta_{ss}^0)$ . In Fig. 1.9b II, the system is close to the Hopf bifurcation so  $(\alpha_{ss}^+, \beta_{ss}^+)$  has a weak repulsive effect. Here, the system stays longer in the vicinity of this state before making an excursion towards  $(\alpha_{ss}^0, \beta_{ss}^0)$ , that is, it goes to  $(\alpha_{ss}^0, \beta_{ss}^0)$  much less frequently. Merkin et al. (1996) showed that the complex dynamics observed in the system satisfied some criteria for chaos. This included loss of spatial correlation and sensitivity to initial conditions and for this reason the complex structures in Fig. 1.9b are characterised as spatiotemporal chaos. However,



the mechanism for generating complex spatiotemporal structures in this system does not depend on equal diffusivity of chemical species compared to previous studies of systems analogous to (1.5.1a)–(1.5.1b) where unequal diffusivity of chemical species is required for the complex spatiotemporal structures to be observed (Pearson, 1993; Petrov and Showalter, 1994; Reynolds et al., 1994).

## 1.5.2 Chaotic Itinerancy in Type I Neurons

The emergence of spatiotemporal chaos in a network of neurons diffusively coupled by gap-junctions was reported in (Fujii and Tsuda, 2004). The collective behaviour of interneurons in the neocortex was modelled using a Morris-Lecar formulation to study cortical activity. The focus of this study was on the population of Type I neurons in which the action potential is produced through a saddle-node bifurcation. It is further claimed that Type I neurons, when coupled by gap junctions, exhibit extensive spatiotemporal chaos in some parameter regions. The neurons when isolated exhibit regular firings, hence the emergence of chaotic behaviour is due to coupling.

Numerical results of membrane potential of  $80 \times 80$  coupled neurons for different values of the gap junction conductance  $g_{GJ}$  is shown in Fig. 1.10a. The results shown are parameter regions close to the saddle-node bifurcation. Fig. 1.10b is a contour map of time series of the membrane potential. It shows creations and annihilations of chaotic waves that result from successive phase shifts in the activity of neighbouring neurons. Here a wave with a short time lag is considered to be synchronised, so transitions between synchronised and desynchronised states is chaotic in both space and time.

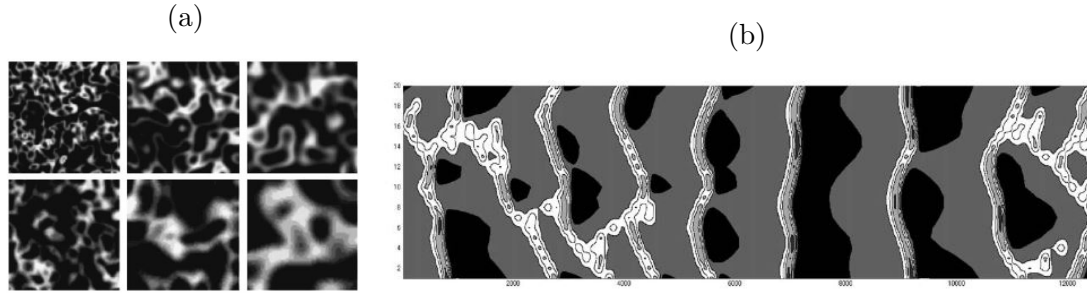


Figure 1.10: (a) Snapshots of the membrane potentials of gap junction-coupled  $80 \times 80$  class  $I^*$  neurons for different values of the gap junction strength (b) Space-time plot of membrane potentials of 20 neurons of class  $I^*$  with the two neighbors by gap junctions. The vertical and horizontal directions indicate respectively the neuron position, and the time. Reprinted from (Fujii and Tsuda, 2004) with permission from Elsevier.

### 1.5.3 Spatiotemporal Chaos in Synaptically Coupled Neurons

Hartle and Wackerbauer (2017) observed transitions from spatiotemporal chaos to travelling pulse solutions in numerical simulations of two synaptically coupled layers of neurons modelled using the Morris-Lecar equations. Each layer represents a ring network of  $N$ -diffusively coupled neurons such that each neuron in a layer is connected synaptically to every neuron in the other layer. The state of the  $i$ -th neuron ( $i = 1, \dots, N$ ) in layer  $k$  ( $k = \text{I, II}$ ) is given by the membrane potential,  $V_i^k$ , and the fraction of open potassium channels,  $n_i^k$ . These are governed by the differential equations

$$\begin{aligned} \frac{dV_i^k}{dt} &= \frac{1}{C_m} (I - I_i^{\text{ion},k} - I_i^{\text{syn},k}) + D\Delta_i^k, \\ \frac{dn_i^k}{dt} &= \tau_i^k (n_i^{\text{ss},k} - n_i^k), \end{aligned} \tag{1.5.4}$$

where  $C_m$  is the membrane capacitance,  $I$  is the applied current,  $I_i^{\text{ion}}$  is the ionic current, and  $I_i^{\text{syn}}$  is the synaptic current (per unit area). The electrical coupling between neighbouring neurons is modelled with the diffusion operator,  $\Delta_i^k = V_{i-1}^k - 2V_i^k + V_{i+1}^k$ , and  $D$  is the diffusive coupling strength. Also  $\tau$  determines the time constant for opening/closing of potassium channels and  $n_i^{\text{ss}}$  is the fraction of open potassium channels at steady state. The

synaptic current for neuron  $i$  in network  $k$  is given by

$$I_i^{\text{syn},k} = g \sum_{l=I, l \neq k}^{II} \sum_{j=1}^N w_{ji}^{lk} s_{ji}^{lk} (V_i^k - V_s), \quad (1.5.5)$$

where  $g$  is the conductance of the synapse and  $w_{ji}^{lk}$  is the synaptic coupling sensor and  $s_{ji}^{lk}$  is the fraction of open channels in the synaptic cleft between presynaptic neuron  $j$  in layer  $l$  and postsynaptic neuron  $i$  in layer  $k$ .

Numerical simulations were conducted for a network of 50 identical, excitable neurons within each layer. The results showed that the system switches spatiotemporal patterns within and between layers I and II. The resulting patterns contain spatiotemporal chaos (STC), regular and erratic propagating pulses, and rest states. In Fig. 1.11 a, both layers begin as STC, then as time progresses layer I remains in STC state while the dynamics in layer II switches to a stripe pattern. At a later time the dynamics in layer I switches from STC to a narrow pulse and layer II collapse to a rest state. In Fig. 1.11 b, the STC in layer II changes to erratic pulses while the STC in layer I persists. After some time, the STC in layer I changes to propagating pulse while STC in layer II is reinitiated and later changes to pulse. Similar behaviours have been observed in [Keplinger and Wackerbauer \(2014\)](#) where an isolated layer is considered. The transient STC is associated with nearby saddle-bifurcations and the existence of a chaotic saddle. More complex behaviours are observed between layers, for example, a significant reduction in the activity of the neurons in one layer causes pulse destabilisation and reinitiation of STC in the other layer. This behaviour is also observed with bidirectional coupling. An example is shown in Fig. 1.12 where a swapping of states between layers as well as reinitiation of STC is observed.

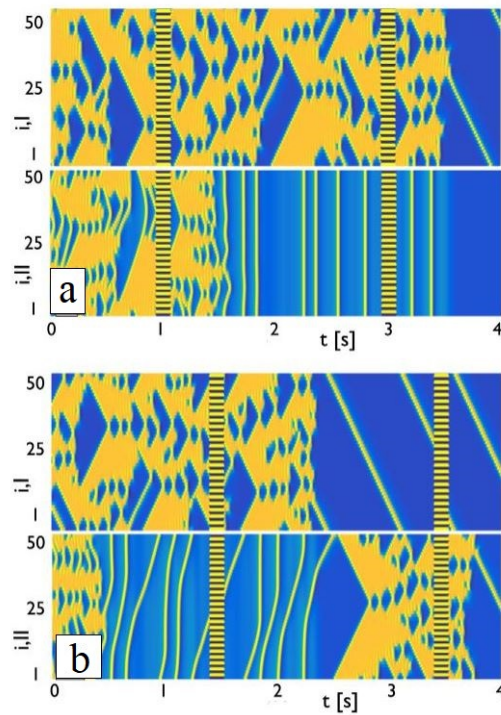


Figure 1.11: The switching sequences of spatiotemporal patterns in layers I and II. Both layers are initially in the STC state. Panel (a) and (b) differ by randomly initial conditions. Reprinted with permission from (Hartle and Wackerbauer, 2017). Copyright (2020) by the American Physical Society.

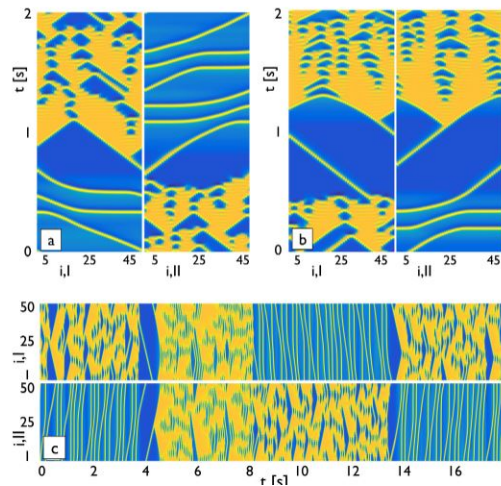


Figure 1.12: Spatiotemporal dynamics for bidirectional synaptic coupling between in layers I and II. Example for (a) a swapping event; (b) reinitiation of STC; and (c) a fast switching sequence. Reprinted with permission from (Hartle and Wackerbauer, 2017). Copyright (2020) by the American Physical Society

## 1.6 Aims and Outline of the Thesis

As described above, pacemaker cells are excitable cells that can generate action potentials in the absence of external stimulation. Despite many experimental and theoretical studies on pacemaker dynamics in SMCs, little is known about cell-to-cell communication. For this reason an in-depth investigation of the mechanisms causing this behaviour could give valuable insights into how populations of SMCs work as a network. Previous studies of pacemaker dynamics have discussed mechanisms for the generation of action potential in an isolated SMC (Gonzalez-Fernandez and Ermentrout, 1994), however, a precise explanation for the development of spatial patterns in coupled-cell systems has not been studied extensively. In this research we study pacemaker dynamics in coupled SMCs using a one-dimensional reaction-diffusion model.

The rest of the thesis is organised as follows. In Chapter 2 we present the reaction-diffusion system to study the dynamics of the membrane potential in a vessel wall of SMCs, and investigate the propagation of action potential between adjacent cells. We analyse the pacemaker dynamics of an isolated SMC to reveal properties of excitable cells in the model. Here we also reduce and nondimensionalise the model for further analysis. We discuss the stability properties of equilibrium points.

In Chapter 3 we briefly describe bifurcations and define some terms associated to bifurcations in excitable cells. We perform a bifurcation analysis to show that the dynamics of the model remains qualitatively similar after model reduction. Transitions between types of excitability is explained using two-parameter bifurcation diagrams. We identify codimension-two bifurcations and parameter regimes in which the SMC exhibits each type of excitability.

In Chapter 4 we numerically study solutions to the reaction-diffusion system formulated in Chapter 2. We review necessary conditions for Turing (diffusion-driven) instability and show that the spatiotemporal patterns observed in the model are not due to Turing instability. We

also discuss the numerical methods and present different types of spatiotemporal patterns behaviour that may occur with variation of model parameters.

Next, existence and stability analyses of travelling waves solutions to the reaction-diffusion system is given in Chapter 5. We introduce spectral stability analysis and numerically compute the essential spectrum to summarise the stability properties of equilibrium points and the travelling waves found in the travelling waves system. Finally Chapter 6 provides a summary and suggests directions for future work.

## 2. A Mathematical Model for Pacemaker Dynamics in Smooth Muscle Cells

Electro-mechanical coupling (EMC) in muscle cells is a process by which electrical excitation in response to external stimulation results in contraction of the cell. The excitation is mediated by the influx of extracellular  $\text{Ca}^{2+}$  through voltage-gated  $\text{Ca}^{2+}$  channels and  $\text{Ca}^{2+}$  release from the cell's internal  $\text{Ca}^{2+}$  store, the sarcoplasmic reticulum (SR). The elevation of the intracellular  $\text{Ca}^{2+}$  concentration causes muscle contraction. The underlying mechanisms involved in EMC activity of some smooth muscle cell (SMC) types have been the subject of numerous mathematical modelling and computational simulation studies. For example, EMC activity in gastric (Aliev et al., 2000; Corrias and Buist, 2007, 2008), bowel (Miftakhov et al., 1996), uterine (Rihana et al., 2009; Tong et al., 2011), mesenteric (Berra-Romani et al., 2005), jejunal (Poh et al., 2012) and arterial (Jacobsen et al., 2007; Cha et al., 2008) SMCs have been modelled by incorporating the dynamics of intracellular calcium concentration and ionic channels in the model.

Pacemaker cells are cells that evoke spontaneous electrical activities in some tissues and organs in the body. Examples of pacemaker cells are: Purkinje fibers, sinoatrial (SA) node, interstitial cell of Cajal (ICC). They are vital in regulating the activities of tissues in the body. For example, the cardiac pacemaker cells control the pumping of blood in the heart. Also, the ICC generates spontaneous rhythmic activity and regulates gut contraction in the gastrointestinal tract. Under normal physiological conditions, SMCs do not oscillate mechanically in the absence of external sources. However several exceptions have been observed experimentally where cells oscillate spontaneously. This cellular behaviour is known

---

as *pacemaker dynamics*. A number of experimental studies have shown that arterial SMCs can exhibit pacemaker EMC due to changes in the vessel's transmural pressure (Johansson and Somlyo, 1980; Harder, 1984, 1987; Ran et al., 2019). Mclean and Sperelakis (1977) studied the spontaneous contraction of cultured vascular SMCs in chick embryos. Lusamvuku et al. (1979) observed spontaneous electrical activity in rabbit cerebral arteries exposed to high pressure. Harder (1984) examined cellular mechanisms of the myogenic response, the pressure-induced contraction of blood vessels to regulate blood flow, in feline middle cerebral arteries by recording intracellular electrical activity of arterial muscle cells upon elevation of transmural pressure. It was observed that the blood vessels contract and spontaneous firing occurs as the arterial blood pressure is increased. Also Osol and Halpern (1988) observed that the spontaneous cyclic oscillations and EMC activity in cerebral arteries from genetically hypertensive rats depend on transmural pressure and temperature *in vitro*.

There are a number of detailed mathematical models for the dynamics of SMCs, their formulation depends on the number and types of voltage-gated ion channels in the cell membranes. Based on experimental observations, the ion channels coordinating the EMC activity in SMCs of feline cerebral arteries are the voltage-gated  $\text{Ca}^{2+}$  channel, voltage-gated  $\text{K}^+$  ion channel and the leak ion channel (Casteels et al., 1977; Harder, 1984; Nelson et al., 1990). Following experimental observations, Gonzalez-Fernandez and Ermentrout (1994) developed a model to study the dynamics of pacemaker vasomotion in SMCs of small arteries. Since the EMC activity does not depend on changes in the concentration of extracellular  $\text{Na}^+$ , their model formulation is based on the Morris-Lecar model (1981). Fig. 2.1 shows the equivalent circuit of the cell membrane with the leak,  $\text{K}^+$ , and  $\text{Ca}^{2+}$  ion channels.

The SMCs are coupled through gap junctions which can be one of three types:  $\text{Ca}^{2+}$ , inositol triphosphate ( $\text{IP}_3$ ) or membrane potential (electrical). A schematic representation of electrically coupled SMCs is shown in Fig. 2.2.

The focus of this research is to study the collective dynamics of electrically coupled pacemaker



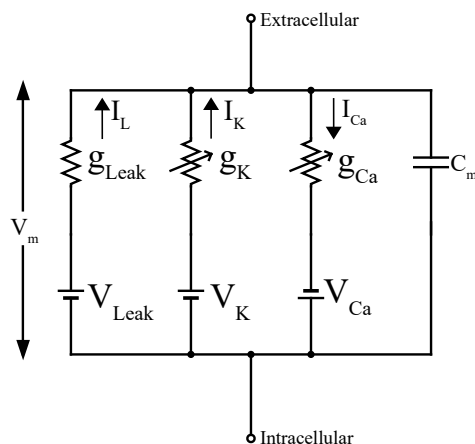


Figure 2.1: Equivalent circuit representation of cell membrane with three ionic channels.  $I_L$ ,  $I_K$  and  $I_{Ca}$  are the leak, potassium and calcium currents.  $C_m$  is the cell membrane capacitance.

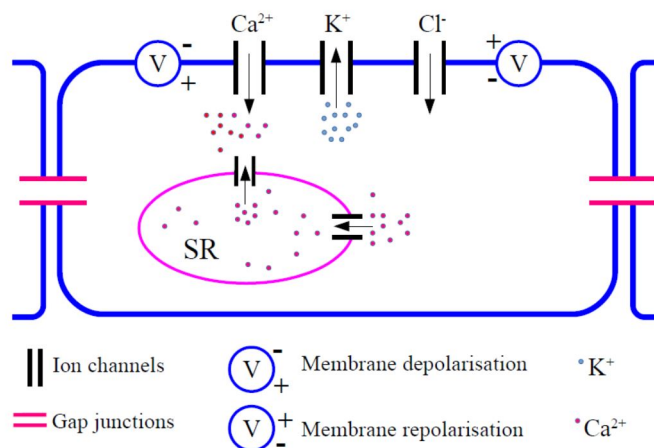


Figure 2.2: Schematic representation of a smooth muscle cell coupled electrically to adjacent cells through gap junctions.

SMCs. The electrical coupling between neighbouring cells in excitable media is commonly modelled as a reaction-diffusion system, for example in neurons (Hodgkin and Huxley, 1952; Hartle and Wackerbauer, 2017). Thus, in the remainder of this chapter, we will formulate a reaction-diffusion system model to investigate pacemaker EMC activity in SMCs via membrane potential coupling. We will analyse the dynamical behaviour of an isolated cell given by the reaction terms and our focus will be on the dynamics of the membrane potential. An analysis of the behaviour of solutions that may exist in the systems will be investigated numerically.

## 2.1 Model Formulation

We propose a reaction-diffusion system to model the dynamics of a population of coupled SMCs through passive electrical coupling of adjacent cells. The reaction term in the model is based on a model developed by Gonzalez-Fernandez and Ermentrout (1994). It contains three variables: the membrane potential,  $v(x, t)$ , the fraction of open  $K^+$  channels,  $n(x, t)$ , and the cytosolic concentration of calcium  $Ca_i(x, t)$ . The differential equation for the membrane potential is:

$$C \frac{\partial v}{\partial t} = D \frac{\partial^2 v}{\partial x^2} - g_L(v - v_L) - g_K n(v - v_K) - g_{Ca} m_\infty(v)(v - v_{Ca}), \quad -\infty < x < \infty, \quad (2.1.1)$$

where  $D \geq 0$  is the diffusion coefficient,  $g_L, g_K$ , and  $g_{Ca}$  are conductances per unit area for the leak, potassium and calcium currents respectively, while  $v_L, v_K$ , and  $v_{Ca}$  are the corresponding Nernst reversal potentials (equilibrium potentials). Also  $C$  is the cell membrane capacitance per unit area and

$$m_\infty(v) = \frac{1}{2} \left( 1 + \tanh \left( \frac{v - v_1}{v_2} \right) \right), \quad (2.1.2)$$

is the fraction of open  $\text{Ca}^{2+}$  channels at steady state, where  $v_1$  is the voltage associated with the opening of half the population of  $\text{Ca}^{2+}$  channels and  $v_2$  measures the spread of the distribution (Gonzalez-Fernandez and Ermentrout, 1994). The differential equation for calcium is:

$$\frac{\partial \text{Ca}_i}{\partial t} = (-\alpha g_{\text{Ca}} m_\infty(v)(v - v_{\text{Ca}}) - k_{\text{Ca}} \text{Ca}_i) \rho, \quad (2.1.3)$$

where  $\alpha = \frac{1}{2\beta V_{\text{cell}} F}$ ,  $V_{\text{cell}}$  is the cell volume,  $\beta$  is the fraction of cell volume occupied by the cytosol,  $F$  is the Faraday constant, and  $k_{\text{Ca}}$  is the rate constant for cytosolic calcium concentration. The parameter  $\rho$  models  $\text{Ca}^+$  buffering, given by:

$$\rho = \frac{(K_d + \text{Ca}_i)^2}{(K_d + \text{Ca}_i)^2 + K_d B_T}, \quad (2.1.4)$$

where  $K_d$  is the ratio of backward and forward binding rates for the calcium and buffer reaction (Sala and Hernandez-Cruz, 1990) and  $B_T$  is the total concentration of the buffers. Lastly the differential equation for the fraction of open potassium channels is:

$$\frac{\partial n}{\partial t} = \lambda_n(v) (n_\infty(v, \text{Ca}_i) - n), \quad (2.1.5)$$

where  $\lambda_n$ , the maximum rate for opening the  $\text{K}^+$  channels, is defined as:

$$\lambda_n = \phi_n \cosh\left(\frac{v - v_3}{2v_4}\right), \quad (2.1.6)$$

where  $\phi_n$  is the rate constant for the kinetics of the  $\text{K}^+$  channel and  $v_3$  and  $v_4$  have similar effects as  $v_1$  and  $v_2$  for the  $\text{Ca}^{2+}$  channel respectively. The function  $n_\infty$  provides the steady state value for  $n$  and is defined as:

$$n_\infty(v, \text{Ca}_i) = \frac{1}{2} \left( 1 + \tanh\left(\frac{v - v_3(\text{Ca}_i)}{v_4}\right) \right), \quad (2.1.7)$$

with

$$v_3(\text{Ca}_i) = -\frac{v_5}{2} \tanh \frac{\text{Ca}_i - \text{Ca}_3}{\text{Ca}_4} + v_6, \quad (2.1.8)$$

where  $\text{Ca}_3$  and  $\text{Ca}_4$  have similar effects as  $v_1$  and  $v_2$  respectively, and  $v_5$  and  $v_6$  are parameters. The plots of  $n_\infty$  against  $\text{Ca}_i$  for three different values of the membrane potential  $v$  are shown in Fig 2.3.

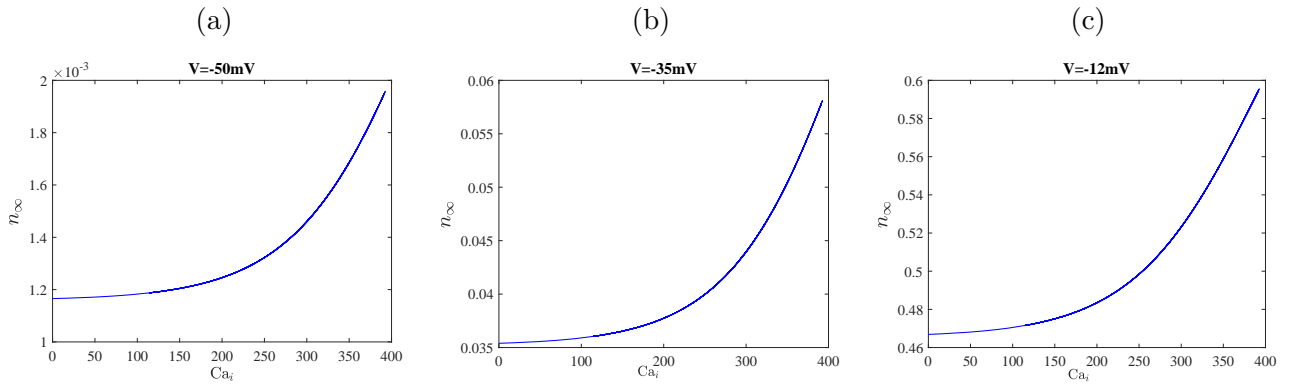


Figure 2.3: The plots of  $n_\infty$  against  $\text{Ca}_i$  for three different values of the membrane potential  $v$ .

To fully specify the reaction-diffusion system, it remains for us to impose boundary and initial conditions. Since we are interested in self-organised patterns, we use no-flux boundary conditions,

$$\frac{\partial v}{\partial x} = \frac{\partial \text{Ca}_i}{\partial x} = \frac{\partial n}{\partial x} = 0, \quad \forall x \in \partial\Omega \quad (2.1.9)$$

where  $\Omega$  is the spatial domain with boundary  $\partial\Omega$ . We will mostly be interested in behaviour far from the boundary. The initial conditions are

$$v(x, 0) = v_0(x), \quad \text{Ca}_i(x, 0) = \text{Ca}_{i0}(x), \quad \text{and} \quad n(x, 0) = n_0(x) \quad \forall x \in \Omega \quad (2.1.10)$$

for some given functions  $v_0(x)$ ,  $\text{Ca}_{i0}(x)$  and  $n_0(x)$ . The parameter values of Gonzalez-

Fernandez and Ermentrout (1994) are listed in Table 2.1.

Table 2.1: Model parameter values are taken from Gonzalez-Fernandez and Ermentrout (1994).

Parameter	Value	Unit
$v_1$	-22.5	mV
$v_2$	25.0	mV
$v_4$	14.5	mV
$v_5$	8.0	mV
$v_6$	-15.0	mV
$Ca_3$	400.0	nM
$Ca_4$	150.0	nM
$\phi_n$	2.664	$s^{-1}$
$v_L$	-70.0	mV
$v_K$	-90.0	mV
$v_{Ca}$	80.0	mV
$C$	$1.9635 \times 10^{-14}$	$C \text{ mV}^{-1}$
$g_L$	$7.854 \times 10^{-14}$	$C \text{ s}^{-1} \text{ mV}^{-1}$
$g_K$	$3.1416 \times 10^{-13}$	$C \text{ s}^{-1} \text{ mV}^{-1}$
$g_{Ca}$	$1.57 \times 10^{-13}$	$C \text{ s}^{-1} \text{ mV}^{-1}$
$K_d$	$1.0 \times 10^3$	nM
$B_T$	$1.0 \times 10^5$	nM
$\alpha$	$7.9976 \times 10^{15}$	$\text{nM } C^{-1}$
$\beta$	$5.5 \times 10^{-1}$	
$V_{\text{cell}}$	$1.1781 \times 10^{-9}$	$\text{cm}^3$
$F$	$9.6487 \times 10^4$	$C \text{ mole}^{-1}$
$k_{Ca}$	$1.3567537 \times 10^2$	$s^{-1}$

## 2.2 Dynamics of an Isolated Smooth Muscle Cell

We begin our analysis with the study of electrical activity in an isolated SMC by investigating the local dynamics of system (2.1.1)–(2.1.8), with  $D = 0$  in (2.1.1). The numerical simulations described below were carried out in MATLAB using the ode45 solver, which uses a variable step-size Runge-Kutta method. Fig. 2.4 shows a time series of the system for the parameter values of Table 2.1 and a typical initial condition. The repetitive spiking of action potentials observed in Fig. 2.4a reveals the pacemaker EMC activity of the SMC. Fig. 2.4c

shows the time evolution of the potassium  $I_K$  and calcium  $I_{Ca}$  currents. It is observed that  $I_K$  lags  $I_{Ca}$  as this effect is observed in the action potentials in Fig. 2.4a. The mechanical stimulation of the SMC results in fluxes of  $Ca^{2+}$  into the cell membrane through the voltage-gated  $Ca^{2+}$  channels and the sarcoplasmic reticulum, causing the depolarisation of the cell membrane resulting in an increase of the membrane potential. As time progresses, the  $K^+$  channels are activated resulting in efflux of  $K^+$ , causing the repolarisation of the cell membrane and consequent decrease in membrane potential. Nelson et al. (1990) reported that in some SMCs  $Ca^{2+}$  does not have a threshold, hence, as observed here, the depolarisation process repeats itself and the system oscillates.

The voltage-gated ion channels play an important role in the physiological response of excitable cells, especially in the generation of action potentials (Ermentrout et al., 2004; Izhikevich, 2007). Therefore, understanding their effects on pacemaker dynamics is highly important in physiology. For example, blocking of specific ion channels is a technique used for treating and managing physiological disorders like Alzheimer's disease and atrial fibrillation. To gain an insight into the role of ion channels on the pacemaker dynamics of the SMC model (2.1.1)–(2.1.8), we block the conductances for the leak,  $Ca^{2+}$ , and  $K^+$  currents in turn. Over a range of parameter values considered, we found that pacemaker activity persists if the leak current conductance  $g_L$  is blocked i.e.  $g_L = 0$ , but is absent if the  $Ca^{2+}$  and  $K^+$  currents are blocked (Fig. 2.5 shows an example). This tells us that the  $Ca^{2+}$  and  $K^+$  currents are required for pacemaker activity in the model.

It has been shown that variation of model parameters can result in a wide variety of electrical activity in an isolated cell, including resting, simple or complex oscillations. In non-pacemaker models, the external current is usually considered as a tuning parameter (or bifurcation parameter) because it ostensibly simulates the cell (Morris and Lecar, 1981; Tsumoto et al., 2006; Zhao and Gu, 2017). Some previous works on pacemaker models have considered the ion channels conductance (González-Miranda, 2014) and effective reversal

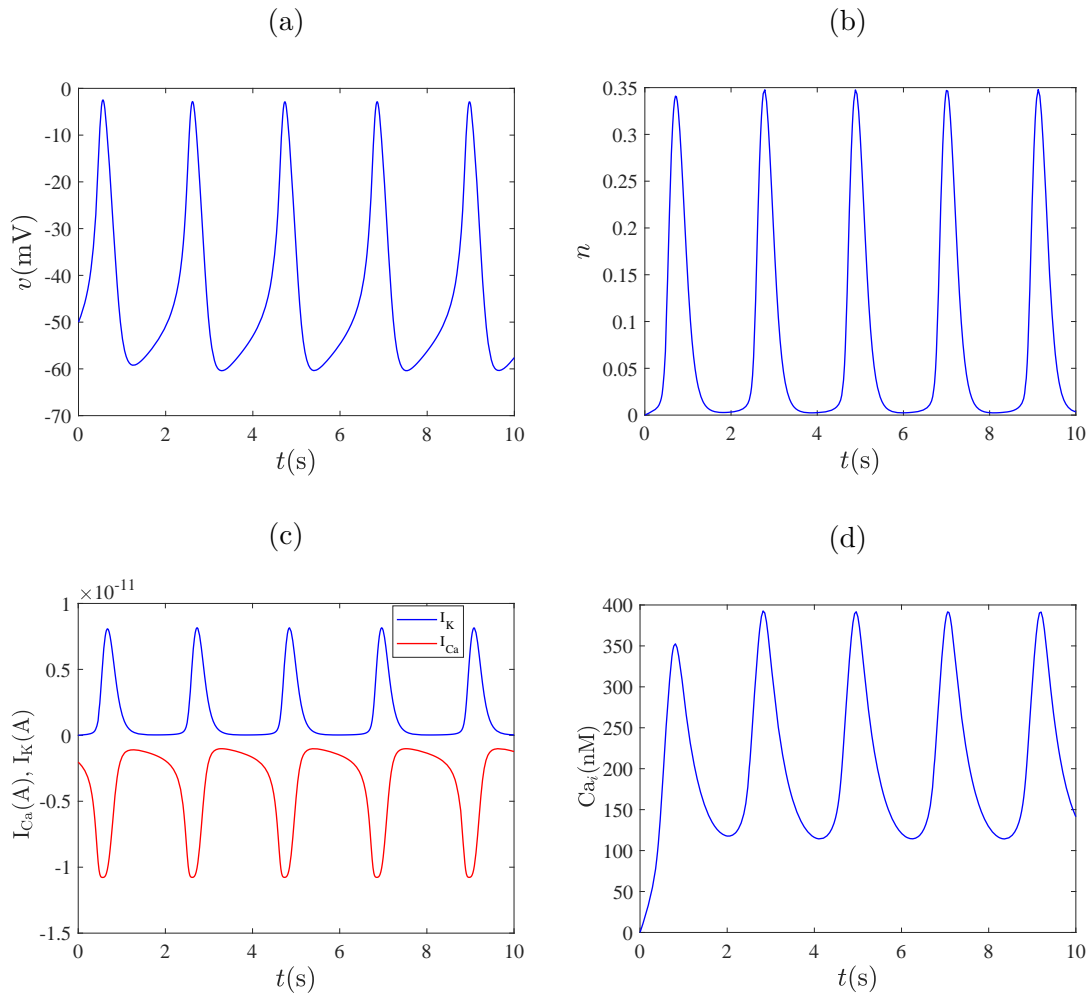


Figure 2.4: Time series of (2.1.1)–(2.1.8) for the (a) membrane potential, (b) fraction of opening  $K^+$  channels, (c) potassium and calcium currents and (d) free cytoplasmic calcium concentration with initial conditions,  $(v, n, Ca_i) = (-50\text{mV}, 0, 0\text{nM})$ , and parameter values in Table 2.1.

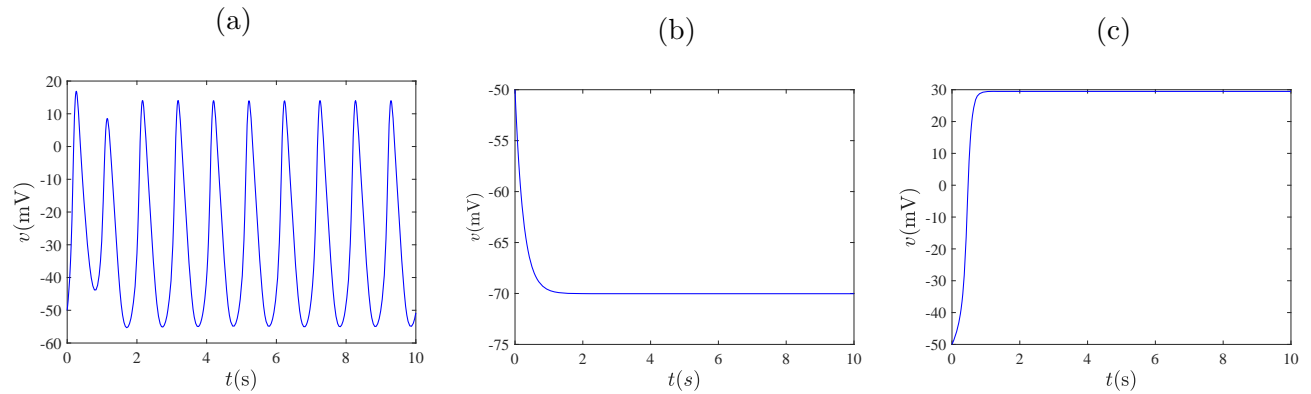


Figure 2.5: Time series of the membrane potential  $v$  when the three conductances are blocked. The parameters used are those of Table 2.2 except (a) the leak channel is blocked ( $g_L = 0$ ); (b) the  $\text{Ca}^{2+}$  channel is blocked ( $g_{\text{Ca}} = 0$ ); (c) the  $\text{K}^+$  channel is blocked ( $g_K = 0$ ).

potential (Duan et al., 2008) as tuning parameters. We now want to reproduce some of these behaviours in our pacemaker model by modulating parameters associated with the ion currents and gating variables, specifically we modulate pressure dependent parameters,  $v_1$  and  $v_6$ . We use values of  $v_1$  between  $-40\text{mV}$  and  $-10\text{mV}$ , and values of  $v_6$  between  $-40\text{mV}$  and  $0\text{mV}$ . These parameter values have been measured in experimental analysis of spontaneous electrical activity in arterial SMCs (Harder, 1984). For the range of values of  $v_1$  and  $v_6$  considered in this thesis, the solutions to system (2.1.1)–(2.1.8) either converge to a steady state or an oscillatory state which correspond to absence or presence of pacemaker EMC in the SMC, respectively. The time evolution of the membrane potential for three different values of  $v_1$  are depicted in Fig. 2.6, and  $v_6$  in Fig. 2.7. These dynamics are consistent with previous studies on non-pacemaker (Morris and Lecar, 1981; Tsumoto et al., 2006) and pacemaker dynamics (Chay, 1985; Duan et al., 2008; González-Miranda, 2014).

To gain more understanding on how the values of the parameters affect the qualitative dynamics we first perform dimension reduction. This will reduce the number of variables to two, making the system more amenable to analysis but at the cost of introducing some approximations. In the next section we will find a suitable reduced model to approximate (2.1.1)–(2.1.8), which from now on will be referred to as the *full model*.



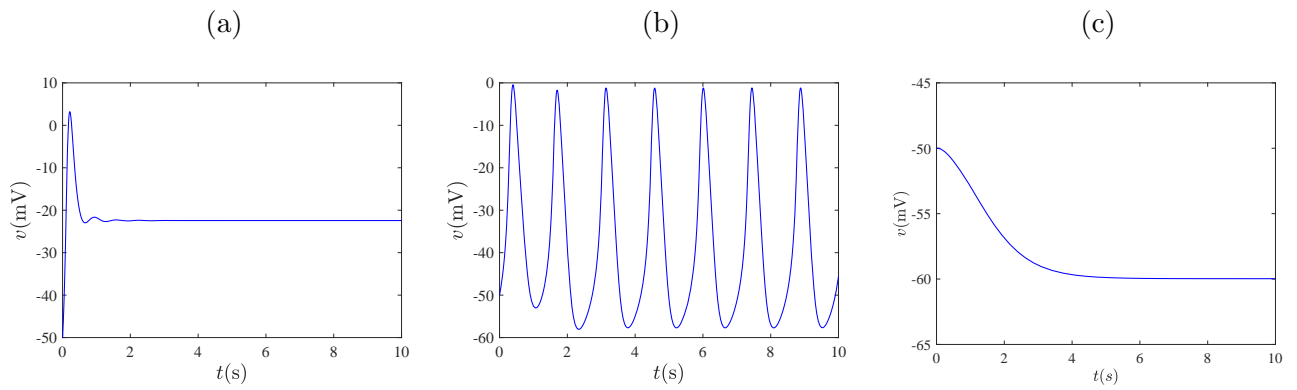


Figure 2.6: Time series of the membrane potential  $v$  for (a)  $v_1 = -35\text{mV}$ ; (b)  $v_1 = -25\text{mV}$ ; (c)  $v_1 = -19\text{mV}$ . Other parameters as in Table 2.1.

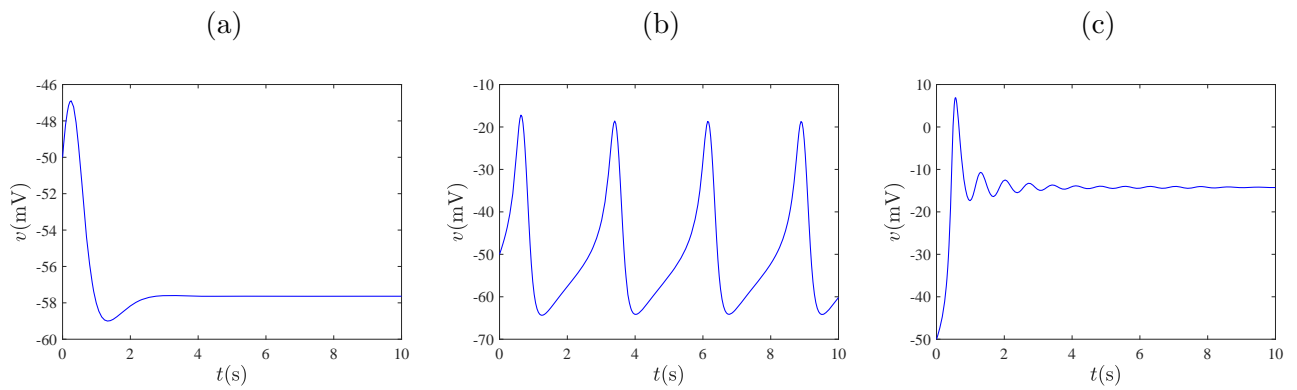


Figure 2.7: Time series of the membrane potential  $v$  for (a)  $v_6 = -35\text{mV}$ ; (b)  $v_6 = -25\text{mV}$ ; (c)  $v_6 = -2\text{mV}$ . Other parameters as in Table 2.1.

### 2.2.1 Model reduction

Mathematical models of physiological processes often contain large numbers of state variables whose inclusion is due to biophysical considerations but which are not of significant importance to the underlying dynamics, mathematically. Thus, removing such variables may have little or no effect on the dynamics under consideration but yield a simplified model that retains the essential properties of the original model. Different methods of model reduction have been widely used, for example, quasi-steady-state approximations and geometric singular perturbation theory (Keener and Sneyd, 2009). Based on observations of simulations of the model (2.1.1)–(2.1.8) there is no specific reduction method that can be applied directly due to the fact there is no obvious separation into fast and slow dynamics between the state variables.

We will use a heuristic approach to reduce the full model to two equations. Our reduction is based on the behaviour of the time-varying function  $v_3$ . Equation (2.1.8) shows that the value of  $v_3$  has the upper and lower bounds  $v_6 + \frac{v_5}{2}$  and  $v_6 - \frac{v_5}{2}$ , respectively. Using the parameter values of Table 2.1 and a numerical solution to system (2.1.1)–(2.1.8) after transient dynamics have decayed, we see from Fig. 2.8 that the value of  $v_3$  spends a high proportion of time close to its upper bound. Similar behaviour is observed across a wide range of parameter values. This motivates a reduction by fixing  $v_3$  to the value of its upper bound. We thus replace (2.1.8) with  $v_3 = v_3^*$ , where  $v_3^* = v_6 + \frac{v_5}{2}$ . The assumption of constant  $v_3$  reduces the number of variables to two because now  $v$  and  $n$  are decoupled from  $\text{Ca}_i$ . Making  $v_3$  constant effectively takes the calcium dependence out of the potassium channel behaviour, thereby decoupling the calcium dynamics from the system. The calcium channel modelling is therefore effectively just done by the calcium current in the membrane

potential equation. The reduced system is

$$C \frac{\partial v}{\partial t} = D \frac{\partial^2 v}{\partial x^2} - g_L(v - v_L) - g_K n(v - v_K) - g_{ca} m_\infty(v)(v - v_{ca}), \quad (2.2.1)$$

$$\frac{\partial n}{\partial t} = \lambda_n(v) (n_\infty(v) - n), \quad (2.2.2)$$

where

$$n_\infty(v) = \frac{1}{2} \left( 1 + \tanh \left( \frac{v - v_3^*}{v_4} \right) \right), \quad (2.2.3)$$

$$\lambda_n(v) = \phi_n \cosh \left( \frac{v - v_3^*}{2v_4} \right), \quad (2.2.4)$$

and  $m_\infty(v)$  is unchanged from (2.1.2), the boundary and initial conditions remain as in (2.2.11) and (2.1.10). In the absence of diffusion (i.e. with  $D = 0$ ) the reduced model is equivalent to the Morris-Lecar model (1981) without external current.

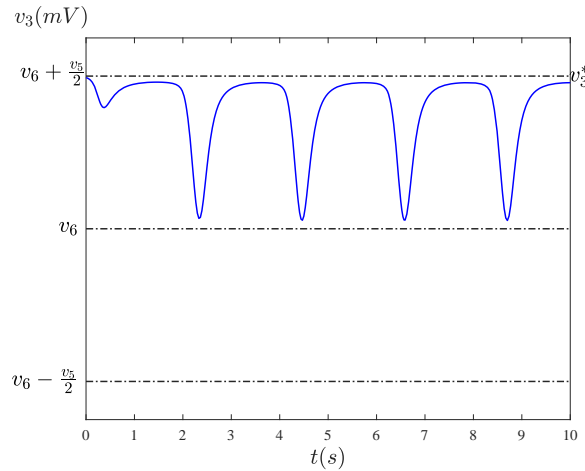


Figure 2.8: A plot of  $v_3$ (mV) against time for solutions to (2.1.1)–(2.1.8) with the parameters of Table 2.1.

In order for the reduced model to be useful, it should capture the essential dynamical behaviour of the original model, meaning the time series and bifurcation structure of the reduced model should be qualitatively similar to those of the original model. For the range of values of  $v_1$  and  $v_3$  considered in this thesis, the dynamics of the reduced model behave

similarly to the full model, and this supports the  $v_3 = v_3^*$  approximation. For the purpose of comparison, Figs. 2.9 and 2.10 illustrate the time evolution of the membrane potential  $v$  for the reduced model (2.2.1)–(2.2.2) for values of  $v_1$  and  $v_3$  corresponding to the values of  $v_1$  and  $v_6$  considered in the case of the full model. We see that Figs. 2.9 and 2.10 are similar qualitatively to Figs. 2.6 and 2.7, respectively. This shows that the full model (2.1.1)–(2.1.8) can be well approximated by the reduced model (2.2.1)–(2.2.2). Before proceeding to analysis of the reduced model, we further simplify (2.2.1)–(2.2.2) by reducing the number of system parameters through dimensional analysis.

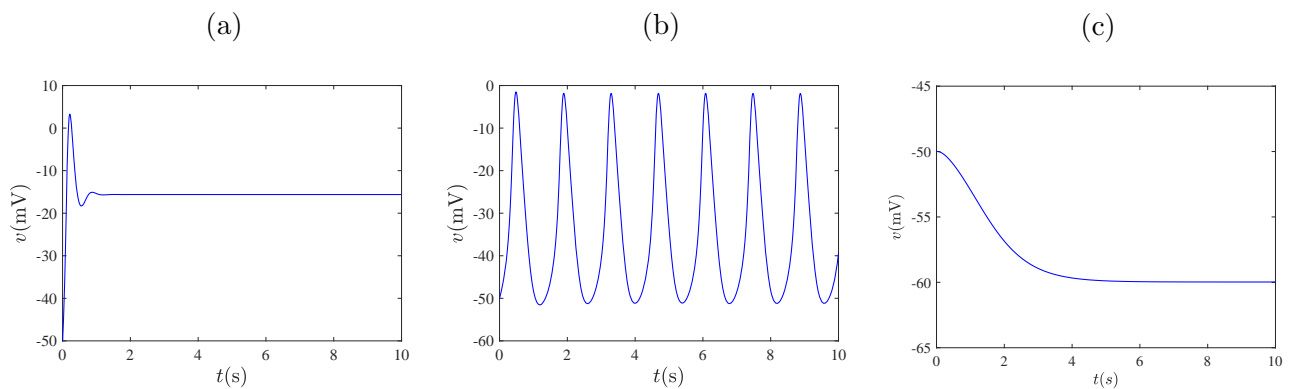


Figure 2.9: Time series of the membrane potential  $v$  for  $v_1$  (a)  $v_1 = -35\text{mV}$ ; (b)  $v_1 = -25\text{mV}$ ; (c)  $v_1 = -19\text{mV}$ . Other parameters as in Table. 2.2.

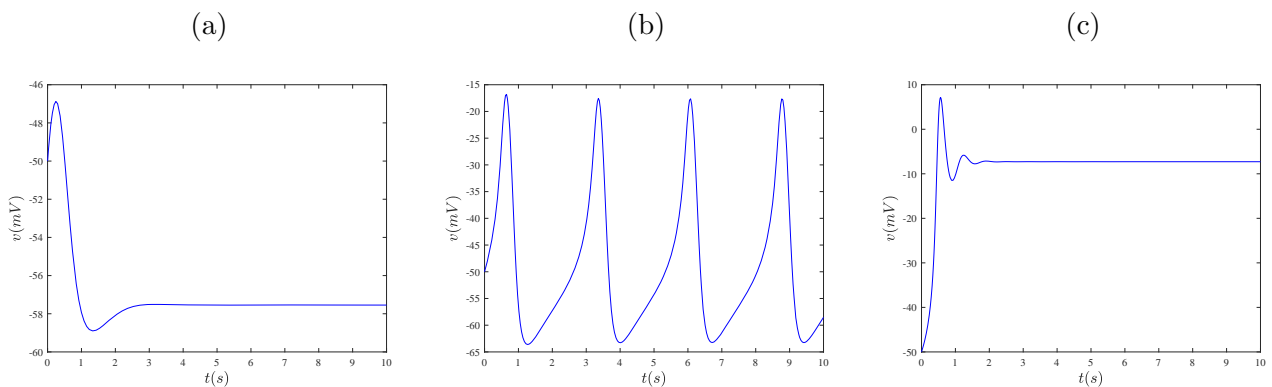


Figure 2.10: Time series of the membrane potential  $v$  for (a)  $v_3 = -31\text{mV}$ ; (b)  $v_3 = -21\text{mV}$ ; (c)  $v_3 = 2\text{mV}$ . Other parameters as in Table. 2.2.

### 2.2.2 Nondimensionalisation

Nondimensionalisation is the process of eliminating dimensions of variables in a mathematical model. Scaling of model variables is used to transform a dimensional model to a nondimensional form. In physiological models, different variables can evolve on different time-scales and this plays a vital role in the generation of action potential. A suitable rescaling of the variables reveals their relative sizes and time constants of the system. The process involves choosing characteristic scales for the variables, and rewriting the dependent and independent variables in terms of  $\mathcal{O}(1)$  quantities by multiplying the variables with their corresponding characteristic scale (Murray, 2003; Logan, 2006) and then grouping variables and parameters of similar magnitudes.

We nondimensionalise (2.2.1)–(2.2.2) by introducing dimensionless variables  $V$  and  $\tau$ . Let

$$v = VQ_v, \quad t = \tau Q_t, \quad (2.2.5)$$

for some characteristic voltage  $Q_v$  and time  $Q_t$ . To choose values for  $Q_v$  and  $Q_t$  we first observe that the range of the action potential is  $v_K \leq v \leq v_{Ca}$  (see Table 2.1 and Fig. 2.4a). Hence the maximum variation of the action potential is less than  $v_{Ca} - v_K = 170\text{mV}$ . This value is roughly the same order of magnitude as  $v_{Ca}$  therefore we choose the characteristic voltage  $Q_v$  to be  $v_{Ca}$ . Simple choices for the characteristic time include  $Q_t = \frac{C}{g_K} = 0.0625\text{s}$  and  $Q_t = \frac{1}{\phi_n} = 0.3754\text{s}$ . We choose  $Q_t = \frac{C}{g_K}$  for the characteristic time because it is faster than  $\frac{1}{\phi_n}$ . Substituting  $Q_v = v_{Ca}$  and  $Q_t = \frac{C}{g_K}$  into (2.2.1)–(2.2.2) produces the dimensionless version of the model:

$$\frac{\partial V}{\partial \tau} = D \frac{\partial^2 V}{\partial X^2} - \bar{g}_L(V - \bar{v}_L) - \bar{g}_K N(V - \bar{v}_K) - \bar{g}_{Ca} M_\infty(V)(V - 1), \quad -\infty < X < \infty, \quad (2.2.6)$$

$$\frac{\partial N}{\partial \tau} = \lambda(V)(N_\infty(V) - N), \quad (2.2.7)$$

where

$$M_\infty(V) = \frac{1}{2} \left( 1 + \tanh \left( \frac{V - \bar{v}_1}{\bar{v}_2} \right) \right), \quad (2.2.8)$$

$$N_\infty(V) = \frac{1}{2} \left( 1 + \tanh \left( \frac{V - \bar{v}_3}{\bar{v}_4} \right) \right), \quad (2.2.9)$$

$$\lambda(V) = \psi \cosh \left( \frac{V - \bar{v}_3}{2\bar{v}_4} \right), \quad (2.2.10)$$

and

$$\bar{g}_r = \frac{g_r}{g_K}, \quad \bar{v}_r = \frac{v_r}{v_{Ca}}, \quad \psi = \frac{C}{g_K} \phi_n, \quad \bar{D} = \frac{C}{g_K} D \quad r = L, K, Ca, 1, 2, 3, 4.$$

The no-flux boundary conditions are,

$$\frac{\partial V}{\partial X} = \frac{\partial N}{\partial X} = 0, \quad \forall X \in \partial\Omega, \quad (2.2.11)$$

and the initial conditions are

$$V(X, 0) = V_0(X) \quad \text{and} \quad N(X, 0) = N_0(X), \quad \forall X \in \Omega \quad (2.2.12)$$

for some given functions  $V_0(X)$  and  $N_0(X)$ . The parameter values for model (2.2.6)–(2.2.7) are given in Table 2.2.

The time series of the membrane potential for the nondimensionalised model (2.2.6)–(2.2.7) in the absence of diffusion term with parameter values in Table 2.2 is shown Fig. 2.11. The oscillatory behaviour observed is similar to the reduced and full model (see Fig. 2.4a). Also, the time evolution for selected values of  $\bar{v}_1$  is shown in Fig. 2.12 and  $\bar{v}_3$  in Fig. 2.13. The values of  $\bar{v}_1$  and  $\bar{v}_3$  correspond to the values of  $v_1$  and  $v_3$  used in Figs. 2.9 and 2.10 for the reduced model (2.2.1)–(2.2.2), and  $v_1$  and  $v_6$  in Figs. 2.6 and 2.7 for the full model (2.1.1)–(2.1.8). Notice that the time series of the nondimensionalised model (Figs. 2.12 and 2.13) are scaled versions of those of the reduced model (Figs. 2.9 and 2.10) because the two systems

Table 2.2: Parameter values for the nondimensionalised model (2.2.6)–(2.2.7).

Parameter	Value
$\bar{v}_1$	−0.2813
$\bar{v}_2$	0.3125
$\bar{v}_3$	−0.1380
$\bar{v}_4$	0.1812
$\psi$	0.1665
$\bar{v}_L$	−0.875
$\bar{v}_K$	−1.125
$\bar{g}_L$	0.25
$\bar{g}_K$	1.0
$\bar{g}_{Ca}$	0.4997
$\bar{D}$	0.0001

Table 2.3: Definition of the nondimensional model variables and parameters.

Variables and Parameters	Definition
$V$	Membrane potential
$N$	Fraction of open $K^+$ channels
$T$	Time
$M_\infty(V)$ [ $N_\infty(V)$ ]	Fraction of open $Ca^{2+}$ [ $K^+$ ] channels at steady state
$\bar{g}_L, \bar{g}_{Ca}, \bar{g}_K$	Conductance for leak, $Ca^{2+}$ and $K^+$
$\bar{v}_L, \bar{v}_K$	Equilibrium potential for $Ca^{2+}$ and $K^+$
$\bar{v}_1$	The potential at which $Ca^{2+}$ channels is half opened
$\bar{v}_2$	The potential at which $K^{2+}$ channels is half opened
$\psi$	Rate constant for kinetics of $K^+$ channel
$\bar{v}_3, \bar{v}_4$	Tuning parameters for steady state
$\lambda(V)$	Voltage dependence associated with the opening of $K^+$ channels

differ only by the change of variables (2.2.5). As noted in the previous section, the reduced model provides a good approximation to the dynamics of the *full model*. Thus we use the nondimensionalised model (2.2.6)–(2.2.7) for further study.

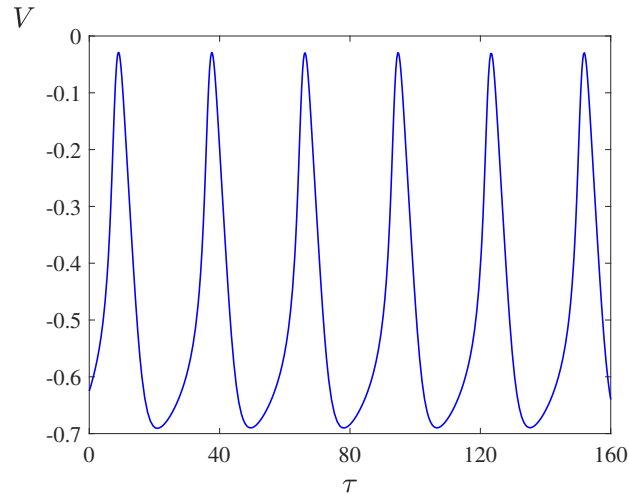


Figure 2.11: Time series of the membrane potential  $V$  for nondimensionalised model (2.2.6)–(2.2.7) with the parameters values in Table 2.2.

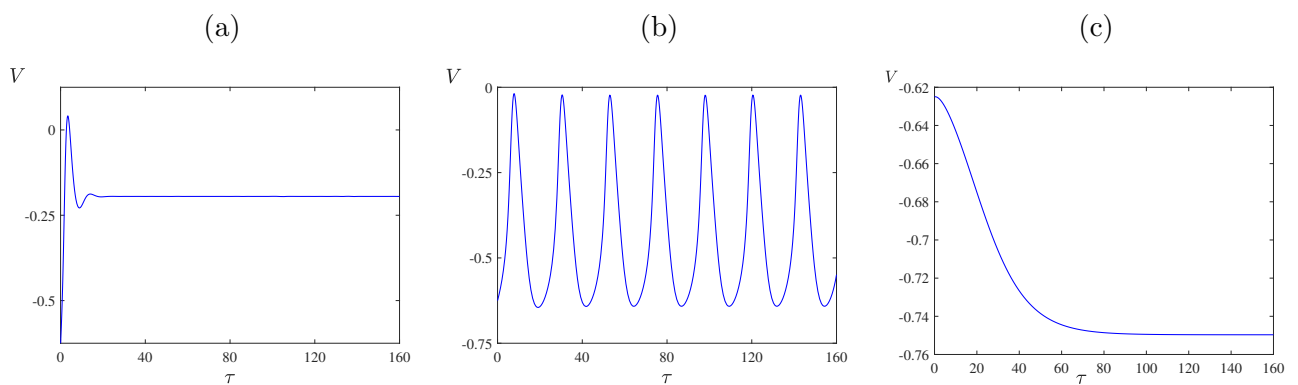


Figure 2.12: Time evolution of the membrane potential  $V$  for (a)  $\bar{v}_1 = -0.4375$ ; (b)  $\bar{v}_1 = -0.3125$ ; (c)  $\bar{v}_1 = -0.2375$ . Other parameters as in Table 2.2.



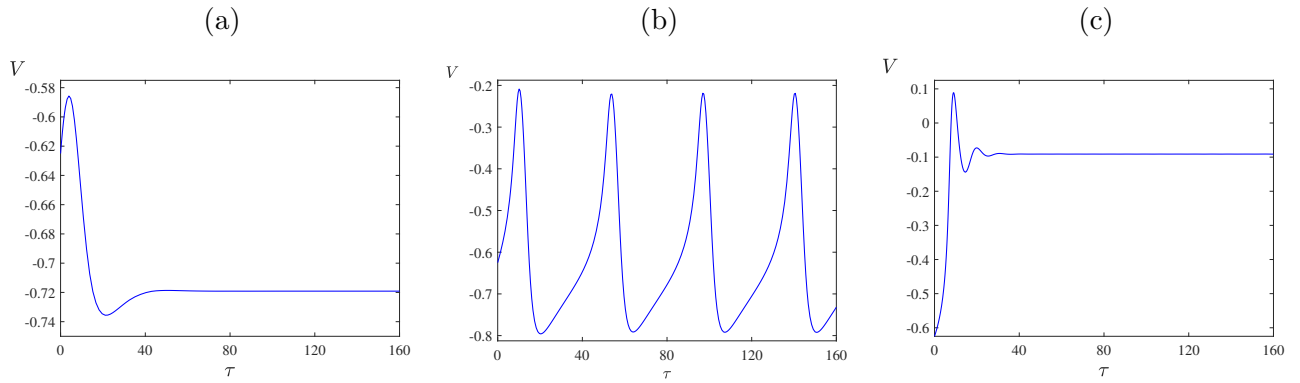


Figure 2.13: Time evolution of the membrane potential  $V$  for (a)  $\bar{v}_3 = -0.3875$ ; (b)  $\bar{v}_3 = -0.2625$ ; (c)  $\bar{v}_3 = 0.025$ . Other parameters as in Table. 2.2.

## 2.3 Linear Stability and Phase Plane Analyses

### 2.3.1 Linear Stability Analysis of Equilibria

In dynamical system, an equilibrium or steady state corresponds to the value or point at which the state variable does not change. In terms of membrane dynamics, the equilibrium corresponds to the point where the transmembrane current is zero and the membrane voltage is unchanged.

Suppose  $(V^*, N^*)$  is an equilibrium of system

$$\frac{dV}{dT} = f(V, N), \quad \frac{dN}{dT} = g(V, N), \quad (2.3.1)$$

that is,  $f(V^*, N^*) = 0$  and  $g(V^*, N^*) = 0$ .

**2.3.1 Definition.** The equilibrium  $(V^*, N^*)$  is said to be *Lyapunov stable* (or *stable*) if for every neighbourhood  $P \subset \mathbb{R}^2$  of  $(V^*, N^*)$  there exists a neighbourhood  $Q \subset \mathbb{R}^2$  of  $(V^*, N^*)$  such that for every initial point  $(V_{\text{init}}, N_{\text{init}}) \in Q$  the solution to (2.3.1) is contained in  $P$  for all  $t \geq 0$ . If  $(V^*, N^*)$  is not Lyapunov stable it is said to be *unstable*.

**2.3.2 Definition.** The equilibrium  $(V^*, N^*)$  is said to be *asymptotically stable* if it is Ly-

punov stable and there exists a neighbourhood  $U \subset \mathbb{R}^2$  of  $(V^*, N^*)$  such that for every initial point  $(V_{\text{init}}, N_{\text{init}}) \in U$  the solution to (2.3.1) converges to  $(V^*, N^*)$  as  $t \rightarrow \infty$ .

In general, the stability properties of an equilibrium in multidimensional are investigated by computing the eigenvalues of the Jacobian matrix evaluated at the equilibrium, say  $J_{(V^*, N^*)}$ . Suppose  $\lambda_i, i = 1, 2, \dots, j, \in \mathbb{C}$  is the set of eigenvalues of  $J_{(V^*, N^*)}$ , then the sign of  $\lambda_i$  determines the stability type of  $(V^*, N^*)$ .

**2.3.3 Definition.** The equilibrium  $(V^*, N^*)$  of (2.3.1) is said to be stable if and only if all the eigenvalues of  $J_{(V^*, N^*)}$  have negative real parts. The equilibrium is unstable if at least one of the eigenvalues has a positive real part.

For planar systems, equilibria can be classified based on their eigenvalues in relation to the values of trace,  $\tau$ , and determinant,  $\delta$ , of  $J_{(V^*, N^*)}$  (Hirsch et al., 2013). The classification of the equilibrium is shown in Table 2.4.

Table 2.4: Classification of equilibrium in planar systems

$\tau, \delta$	Eigenvalues	Equilibrium
$\tau < 0, \delta > \frac{\tau^2}{4}$	$\lambda_{1,2}$ are complex with negative real parts	Stable focus
$\tau > 0, \delta > \frac{\tau^2}{4}$	$\lambda_{1,2}$ are complex with positive real parts	Unstable focus
$\tau < 0, \delta < \frac{\tau^2}{4}$	$\lambda_2 < \lambda_1 < 0$ $\lambda_{1,2}$ are real and negative	Stable node
$\tau > 0, \delta < \frac{\tau^2}{4}$	$0 < \lambda_2 < \lambda_1$ $\lambda_{1,2}$ are real and positive	Unstable node
$\delta < 0$	$\lambda_2 < 0 < \lambda_1$ $\lambda_{1,2}$ are real with opposite sign	Saddle (Unstable)

### 2.3.2 Phase Plane Analysis

The phase plane is the set of all states of a two-dimensional dynamical system. In the phase plane we can visualise the evolution of the system for many different initial conditions by plotting a phase portrait. This consists of sufficiently many trajectories (particular solutions) to produce a clear picture. Alternatively a vector field shows the magnitude and direction in which the system will evolve from any initial condition in the phase plane.

Nullclines are curves in the phase plane along which the derivative of one of the system variable is zero. For an autonomous system of ODEs:  $\frac{dX}{dt} = F(X, Y)$  and  $\frac{dY}{dt} = G(X, Y)$ , the nullclines for  $X$  and  $Y$  are set of points in the phase plane such that  $\frac{dX}{dt} = 0$ ,  $\frac{dY}{dt} = 0$ . Algebraically, these correspond to  $F(X, Y) = 0$  and  $G(X, Y) = 0$ , respectively. Any intersection of  $X$  and  $Y$  nullclines is an equilibrium  $(X^*, Y^*)$  of the system.

For the nondimensionalised model (2.2.6)–(2.2.7), the  $V$ -nullcline is given by the following function

$$N = \frac{-\bar{g}_L(V - \bar{v}_L) - \bar{g}_{ca}M_\infty(V - 1)}{\bar{g}_K(V - \bar{v}_K)}, \quad (2.3.2)$$

and the  $N$ -nullcline is given by

$$N = N_\infty(V) = \frac{1}{2} \left( 1 + \tanh \left( \frac{V - \bar{v}_3}{\bar{v}_4} \right) \right). \quad (2.3.3)$$

Figure 2.14 shows the phase plane for the model (2.2.6)–(2.2.7) with respect to parameter values in Table 2.2. The figure includes sample trajectories, the vector field and the  $V$  and  $N$  nullclines. The  $V$ -nullcline is magenta and the  $N$ -nullcline is orange in Fig. 2.14, they intersect at the equilibrium  $(V^*, N^*) = (-0.2573, 0.2119)$ . This equilibrium is an unstable focus; nearby trajectories spiral away from  $(V^*, N^*)$ . The periodic oscillations

in Fig. 2.11 corresponds to the closed trajectory or loop coloured blue in Fig. 2.14, and is known as periodic orbit. As seen in Fig. 2.14, the periodic orbit is stable, so it attracts nearby trajectories (in fact with the given parameter values all trajectories converge to the periodic orbit except the equilibrium  $(V^*, N^*)$ ).

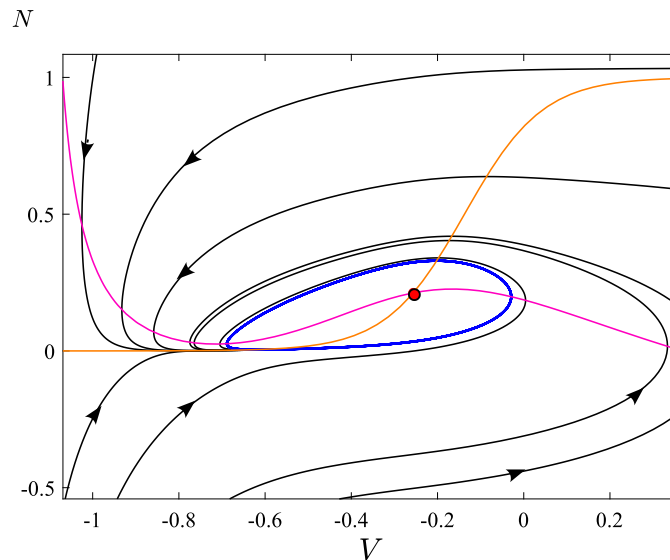


Figure 2.14: (a) The  $(V, N)$  phase plane for the nondimensionalised model (2.2.6)–(2.2.7) with parameters as in Table 2.2. The blue curve is a stable periodic orbit. The magenta and orange curves are the nullclines for  $V$  and  $n$ . The black curves are the solution trajectories. The red circle is unstable equilibrium.

The phase plane for the selected values of  $\bar{v}_1$  in Fig. 2.12 is shown in Figure 2.15. First with  $\bar{v}_1 = -0.4375$  we have Fig. 2.15a,  $(V^*, N^*) = (-0.1952, 0.3472)$ . It is observed that nearby trajectories spiral toward the equilibrium confirming that the equilibrium is stable. Fig. 2.15b depicts the phase plane for  $\bar{v}_1 = -0.3125$ . Here the equilibrium is unstable and surrounded by a stable periodic orbit (as in Fig. 2.14). For  $\bar{v}_1 = -0.22$ , the phase plane is shown in Fig. 2.15c. Here the nullclines intersect at three points,  $(V_1^*, N_1^*) = (-0.3329, 0.1032)$ ,  $(V_2^*, N_2^*) = (-0.5168, 0.015)$ , and  $(V_3^*, N_3^*) = (-0.7801, 0.0008)$ . Therefore, this value of  $\bar{v}_1$  there exist three equilibria in the system. The equilibria  $(V_1^*, N_1^*)$  and  $(V_2^*, N_2^*)$  are unstable. Specifically  $(V_1^*, N_1^*)$  is an unstable focus while  $(V_2^*, N_2^*)$  is a saddle. The red and green curves

in Fig. 2.15c are the stable and unstable manifolds of  $(V_2, N_2)$ . Trajectories near  $(V_3^*, N_3^*)$  converge to this equilibrium confirming it is stable.. As an overall observation, increasing the value of  $\bar{v}_1$  causes a downward shift of the  $V$ -nullcline while the  $N$ -nullcline is unaffected (and this can be readily understood from (2.3.2) and (2.3.3)).

Figure 2.16 provides analogous pictures for the selected values of  $\bar{v}_3$  in Fig. 2.13. Fig. 2.16a depicts the phase plane for when  $\bar{v}_3 = -0.3875$ , nullclines intersect at the stable equilibrium  $(V^*, N^*) = (-0.7191, 0.0251)$ . When  $\bar{v}_3 = -0.2625$ , the nullclines intersect at the repelling focus  $(V^*, N^*) = (-0.4451, 0.1176)$  and there exists a stable periodic orbit, Fig. 2.16b. Finally with  $\bar{v}_3 = 0.025$ , see Fig. 2.16c, the nullclines intersect at the stable equilibrium  $(V^*, N^*) = (-0.0911, 0.2173)$  much like in panel a. Observe that increasing the value of  $\bar{v}_3$  causes a rightward shift of the  $N$ -nullcline while the  $V$ -nullcline remains unchanged.

The equilibria obtained in Figs. 2.14, 2.15, and 2.16 can also be classified via the nature of the eigenvalues. For the nondimensionalised model (2.2.6)–(2.2.7) the derivatives of the  $f(V, N)$  and  $g(V, N)$  evaluated at  $(V^*, N^*)$  are

$$f_V = \left[ -\bar{g}_L - \bar{g}_K N^* - \frac{\bar{g}_{Ca}}{2\bar{v}_2} \left( 1 - \tanh^2 \left( \frac{V^* - \bar{v}_1}{\bar{v}_2} \right) \right) (V^* - \bar{v}_{Ca}) - \frac{\bar{g}_{Ca}}{2} \left( 1 + \tanh \left( \frac{V^* - \bar{v}_1}{\bar{v}_2} \right) \right) \right],$$

$$f_N = -\bar{g}_K (V^* - \bar{v}_K),$$

$$g_V = \frac{\psi}{2\bar{v}_4} \left[ \left\{ \frac{1}{2} \left( 1 + \tanh \left( \frac{V^* - \bar{v}_3}{\bar{v}_4} \right) \right) - N^* \right\} \sinh \left( \frac{V^* - \bar{v}_3}{2\bar{v}_4} \right) \right]$$

$$+ \frac{\psi}{2\bar{v}_4} \left[ \cosh \left( \frac{V^* - \bar{v}_3}{2\bar{v}_4} \right) \left( 1 - \tanh^2 \left( \frac{V^* - \bar{v}_3}{\bar{v}_4} \right) \right) \right],$$

$$g_N = -\psi \cosh \left( \frac{V^* - \bar{v}_3}{2\bar{v}_4} \right).$$

For the parameter values in Table 2.2,  $(V^*, N^*) = (-0.2573, 0.2119)$ . The Jacobian matrix

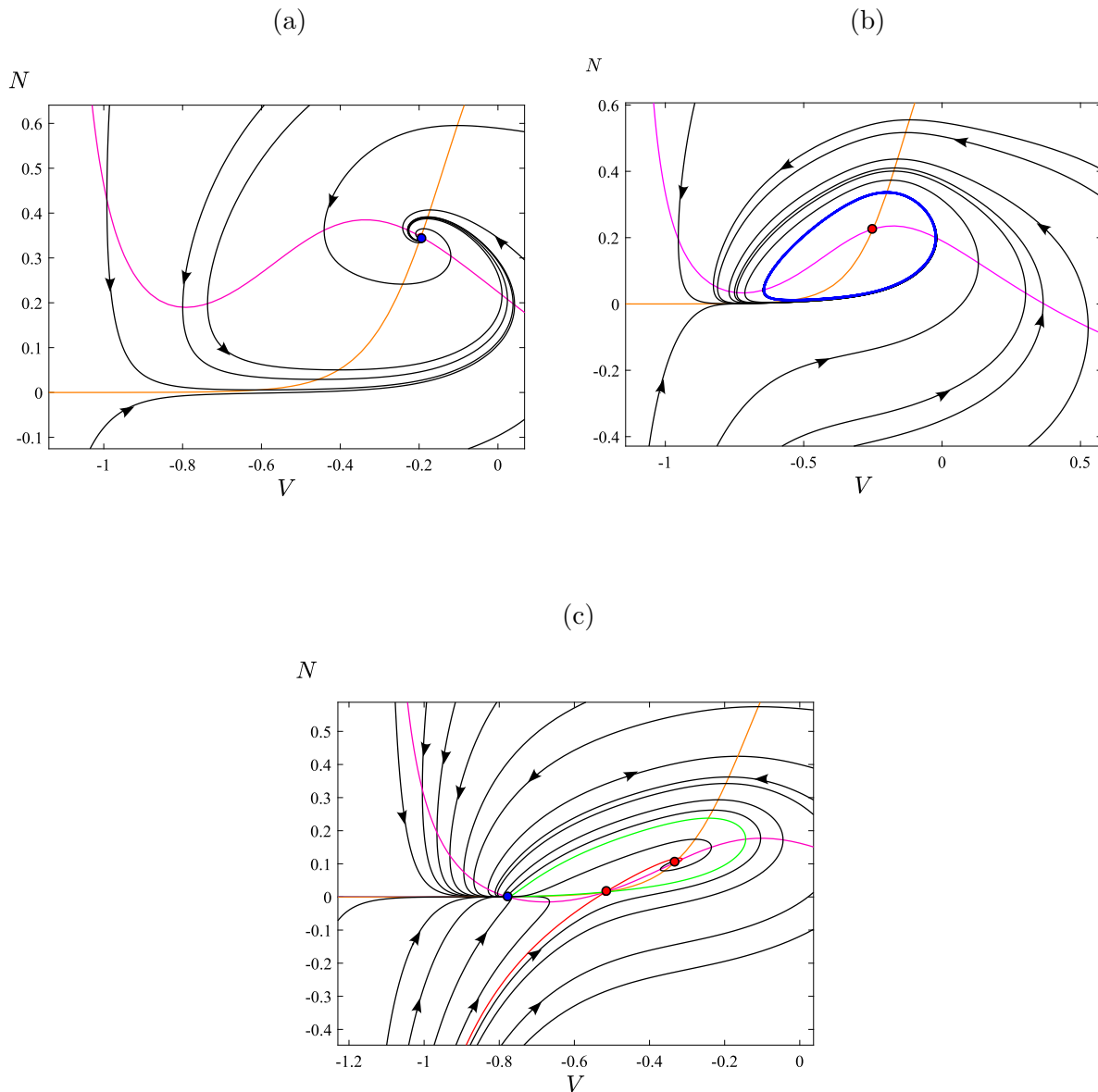


Figure 2.15: The  $(V, N)$  phase plane for the nondimensionalised model (2.2.6)–(2.2.7) with (a)  $\bar{v}_1 = -0.4375$ ; (b)  $\bar{v}_1 = -0.3125$ ; (c)  $\bar{v}_1 = -0.25$ ; The blue and red curve is a stable periodic orbit. The magenta and orange curves are the nullclines for  $V$  and  $N$ . The black curves are the solution trajectories. The blue and red circles are stable and unstable equilibria. The red and green curves in (c) are the stable and unstable manifolds of the saddle point. Other parameters as in Table. 2.2.

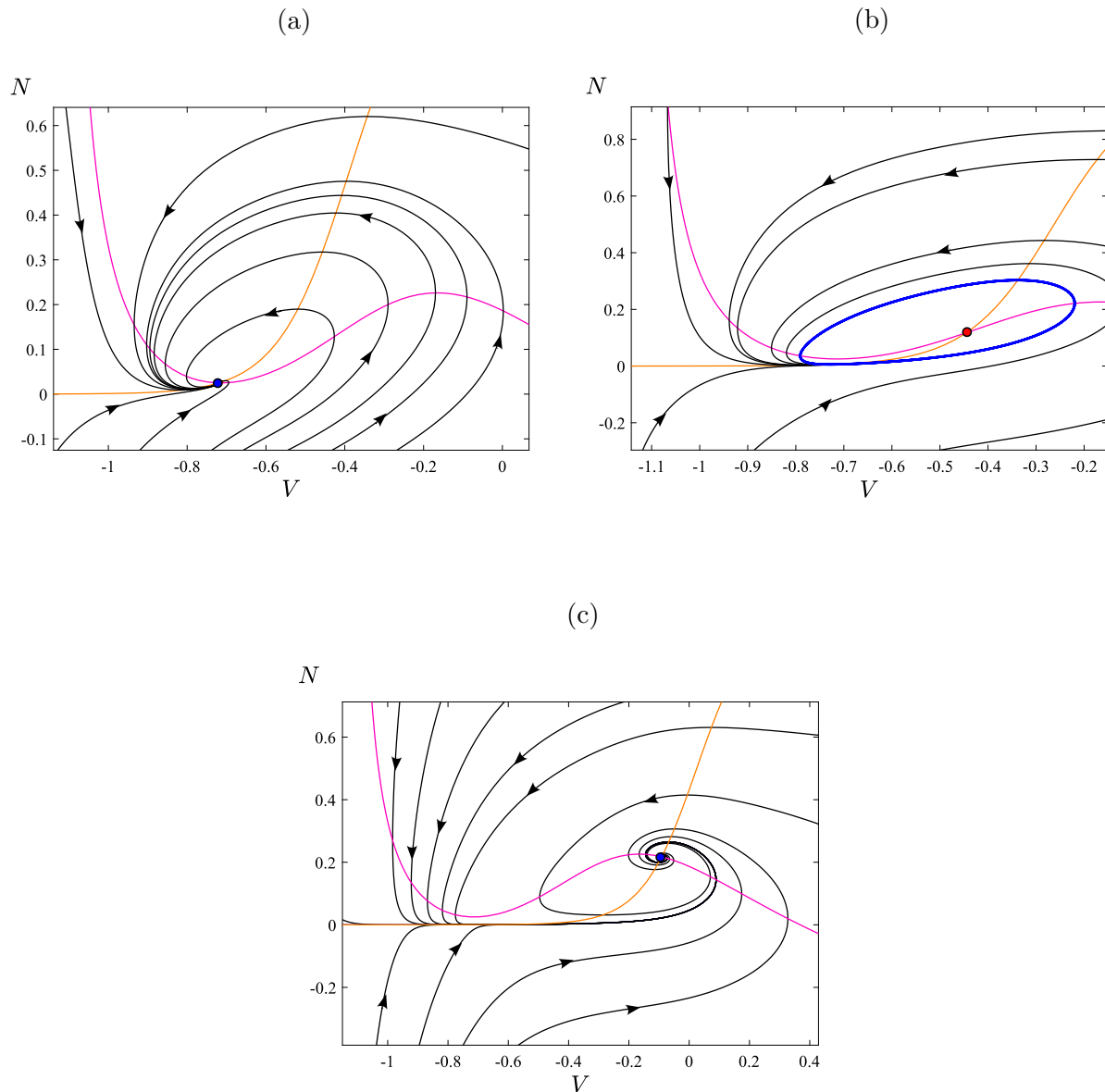


Figure 2.16: The  $(V, N)$  phase plane for the nondimensionalised model (2.2.6)–(2.2.7) with (a)  $\bar{v}_3 = -0.3875$ ; (b)  $\bar{v}_3 = -0.2625$ ; (c)  $\bar{v}_3 = 0.025$ ; The blue curve is a stable periodic orbit. The magenta and orange curves are the nullclines for  $V$  and  $N$ . The black curves are the solution trajectories. The blue and red circles are stable and unstable equilibria. Other parameters as in Table. 2.2.

evaluated at  $(V^*, N^*)$  is

$$J = \begin{pmatrix} 0.2678 & -0.8680 \\ 0.3236 & -0.1756 \end{pmatrix}, \quad (2.3.4)$$

whose eigenvalues,  $\lambda_{1,2} = 0.0461 \pm 0.4814i$ , are complex with positive real parts, thus  $(V^*, N^*)$  is an unstable focus.

Next, we consider cases for different values of  $\bar{v}_1$  with other parameter values as in Table 2.2:

- Case 1:  $\bar{v}_1 = -0.4375$ , the equilibrium is  $(V^*, N^*) = (-0.1952, 0.3472)$ . The Jacobian matrix is

$$J = \begin{pmatrix} -0.4576 & -0.9298 \\ 0.4217 & -0.1686 \end{pmatrix}, \quad (2.3.5)$$

and its corresponding eigenvalues,  $\lambda_{1,2} = -0.3131 \pm 0.6093i$ , are complex with negative real parts. Thus, the equilibrium is a stable focus.

- Case 2:  $\bar{v}_1 = -0.3125$ , the equilibrium is  $(V^*, N^*) = (-0.2494, 0.2262)$ . The Jacobian matrix is

$$J = \begin{pmatrix} 0.2208 & -0.8756 \\ 0.3370 & -0.1744 \end{pmatrix}, \quad (2.3.6)$$

and its corresponding eigenvalues,  $\lambda_{1,2} = 0.0232 \pm 0.5060i$ , are complex with positive real parts, therefore, the equilibrium is an unstable focus.

- Case 3:  $\bar{v}_1 = -0.25$ , the system has three equilibria:

- $(V_1^*, N_1^*) = (-0.3329, 0.1032)$ , the Jacobian matrix evaluated is

$$J = \begin{pmatrix} 0.4207 & -0.7911 \\ 0.1955 & -0.1914 \end{pmatrix}, \quad (2.3.7)$$

its corresponding eigenvalues,  $\lambda_{1,2} = 0.1146 \pm 0.2470i$ , are complex with positive real parts, therefore, the equilibrium is an unstable focus.



ii.  $(V_2^*, N_2^*) = (-0.5168, 0.015)$ , the Jacobian matrix evaluated is

$$J = \begin{pmatrix} 0.2198 & -0.6086 \\ 0.0437 & -0.2658 \end{pmatrix}, \quad (2.3.8)$$

its corresponding eigenvalues,  $\lambda_1 = 0.1146$  and  $\lambda_2 = -0.2029$ , are real with one positive and one negative, therefore, it is a saddle point which is always unstable.

iii.  $(V_3^*, N_3^*) = (-0.7801, 0.0008)$ , the Jacobian matrix is

$$J = \begin{pmatrix} -0.1148 & -0.3449 \\ 0.0046 & -0.5038 \end{pmatrix}, \quad (2.3.9)$$

and its corresponding eigenvalues,  $\lambda_1 = -0.1189$  and  $\lambda_2 = -0.4996$ , are both real and negative, therefore, it is a stable node.

Note that the stability properties of the equilibria for (2.2.6)–(2.2.7) are in agreement with the results found geometrically via the phase plane analysis. For example, when  $\bar{v}_1 = -0.25$ , there are two unstable (unstable focus and a saddle) and a stable (node) equilibria as observed in Fig. 2.15c, respectively.

## 2.4 Discussion

In this chapter we formulated a reaction-diffusion system for pacemaker SMCs coupled through electrical gap junctions based on the model of [Gonzalez-Fernandez and Ementrout \(1994\)](#). We studied the system in the absence of diffusion which corresponds to an isolated SMC where the interactions between ion fluxes, in particular  $\text{Ca}^{2+}$  and  $\text{K}^+$ , results in spontaneous oscillations. We established importance of both  $\text{Ca}^{2+}$  and  $\text{K}^+$  currents on to this oscillations by blocking the three different channels in turn. Upon varying pressure dependent parameters, the model exhibits various dynamical

---

features, such as a rest, or quiescent state, and an oscillatory state, observed in the conventional (non-pacemaker) models for excitable cells.

For further analysis we reduced the full model (2.1.1)–(2.1.8) to two dimensions and performed a nondimensionalisation. We found that this reduction did not significantly alter the qualitative dynamics. By performing phase plane analyses of the nondimensionalised system, (2.2.6)–(2.2.7), we found that the values of the parameters  $\bar{v}_1$  and  $\bar{v}_3$  affect the number and stability of equilibria. This motivates the bifurcation analysis presented in the next chapter.

# 3. Transitions between Types of Excitability

In the previous chapter we observed different dynamical behaviours of model (2.2.6)–(2.2.7) for different values of the parameters and investigated the stability properties of the equilibria. The phase plane analysis qualitatively provided some information about how solutions of the system change due to variation of parameters. In this chapter we seek to improve our understanding of how the dynamics changes with the parameter values via a numerical bifurcation analysis.

In Sec. 3.1 we give an overview of numerical continuation technique and provide an introduction to bifurcation theory emphasizing topics most relevant for excitable cells. Then in Sec. 3.2 we analyse changes to dynamics of (2.2.6)–(2.2.7) as one of four different key parameters of the model are varied in turn. We perform a two-parameter bifurcation analysis to show transitions between types of excitability in Sec. 3.3. In Sec. 3.4 we study the effects of some other parameters, specifically the conductances associated with the three ion channels and briefly explore pacemaker dynamics in the model in the absence of leak conductance. Finally Sec. 3.5 provides a summary and discussion.

## 3.1 Numerical Continuation and Bifurcation Techniques

Numerical continuation is a method in which the solutions of a nonlinear system of equations are followed through the path of an existing solution as a parameter is varied. This technique has been widely used in dynamical systems to study steady state

and periodic solutions, and their stability and transition to more complex behaviour as parameters are varied in various systems. Different algorithms have been developed to compute a family or path of solutions numerically, these include Newton's method, the natural parameter continuation and the arclength and pseudo-arc length continuation method, and Moore-Penrose continuation (Doedel et al., 1991a,b; Kuznetsov, 1995; Allgower and Georg, 2003). Most of these algorithms use the predictor-corrector method and have been implemented using numerical continuation software and packages such as DDE-BIFTOOL (Engelborghs et al., 2002), MATCONT (Govaerts et al., 2011), AUTO (Doedel et al., 2012), XPPAUT (Ermentrout, 2002).

In this thesis we use AUTO 07P for the numerical continuation and bifurcation analysis of our system. This uses orthogonal collocation and pseudo-arclength continuation to solve ordinary differential equations as a bifurcation parameter varies. AUTO 07P computes bifurcations of equilibria and periodic solutions in one parameter. It is able to detect various kinds of bifurcations and folds, switch to and compute the bifurcated branches, and allows us to follow the loci of the bifurcations and folds in two and three parameters to detect codimension-2 bifurcation points.

### 3.1.1 An Introduction to Bifurcation Theory

As the parameters of a dynamical system are varied in a continuous fashion, a bifurcation is said to occur if, roughly speaking, the dynamics of the system changes in a fundamental way. This is made more precise by using the notion of topological equivalence.

Consider a one-parameter system

$$\dot{x} = f(x; \alpha) \tag{3.1.1}$$

with variable  $x(t) \in \mathbb{R}^n$  and  $\alpha \in \mathbb{R}$ . Throughout this section we assume  $f$  is a smooth

function of  $x$  and  $\alpha$ . The various results in this section require different degrees of smoothness (see Kuznetsov (1995)). We do not detail this here as our model (from Sec. 2.1) is  $C^\infty$ . By the Picard-Lindelöf Theorem (see for instance Meiss (2007)) solutions to (3.1.1) exist and are unique and so can be written as a *flow*  $\varphi_t(x)$ . In the following definition it is assumed for simplicity that  $\varphi_t(x)$  is defined for all  $t \in \mathbb{R}$ . Recall that a *homeomorphism* is a continuous, one-to-one, onto function with a continuous inverse.

**3.1.1 Definition.** Let  $\alpha_1, \alpha_2 \in \mathbb{R}$ . The systems  $\dot{x} = f(x; \alpha_1)$  and  $\dot{x} = f(x; \alpha_2)$  are said to be *topologically equivalent* if there exists a homeomorphism  $h : \mathbb{R}^n \rightarrow \mathbb{R}^n$  and a continuous function  $\tau : \mathbb{R}^n \times \mathbb{R} \rightarrow \mathbb{R}$  that is increasing in  $t$  such that

$$h(\varphi_{\tau(x,t)}(x; \alpha_1)) = \varphi_t(h(x); \alpha_2), \quad (3.1.2)$$

for all  $x \in \mathbb{R}^n$  and all  $t \in \mathbb{R}$ .

The orbits of topologically equivalent systems display the same ‘structure’ in phase space. The function  $\tau$  allows orbits of the two systems to evolve at different speeds (if (3.1.2) is satisfied with  $\tau(x, t) = t$  the systems are said to be *conjugate*).

**3.1.2 Definition.** A value  $\alpha^* \in \mathbb{R}$  is said to be a *bifurcation* value of (3.1.1) if for all  $\delta > 0$  there exists  $\alpha_1 \in \mathbb{R}$  with  $|\alpha_1 - \alpha^*| < \delta$  such that  $\dot{x} = f(x; \alpha^*)$  and  $\dot{x} = f(x; \alpha_1)$  are not topologically equivalent.

Bifurcations can be classified as either local or global, depending, as these words suggest, on the size of phase space that is affected. Local bifurcations include bifurcations at which an equilibrium  $x^*$  becomes non-hyperbolic. This means that the Jacobian matrix  $J = Df(x^*)$  has a zero or purely imaginary eigenvalue. We now list local bifurcations that are common in excitable media.

- Saddle-node bifurcation: This occurs when  $J$  has a zero eigenvalue. At the bifurcation two equilibria collide and annihilate. For this reason the bifurcation is also sometimes called a fold or limit point.
- Hopf bifurcation: This occurs when  $J$  attains a pair of purely imaginary eigenvalues. For a two-dimensional system an equilibrium changes stability at a Hopf bifurcation and a limit cycle is created that exists on one side of the bifurcation. If the limit cycle is stable (and existing when the equilibrium is unstable) the Hopf bifurcation is said to be supercritical; if the limit cycle is unstable (and existing when the equilibrium is stable) the Hopf bifurcation is said to be subcritical. In higher dimensions the stable and unstable manifolds of the equilibrium change dimension and a limit cycle is created in the same way.
- Saddle-node of limit cycle bifurcation: This is simply a saddle-node bifurcation of a limit cycle and occurs when a Floquet multiplier (these are analogous to eigenvalues of equilibria) associated with the limit cycle (these are analogous to eigenvalues of equilibria) attains the value 1. At the bifurcation two limit cycles collide and annihilate.
- Period doubling bifurcation: This occurs when a Floquet multiplier associated with a limit cycle attains the value -1. At the bifurcation the limit cycle changes stability (or more precisely its stable and unstable manifold change dimension) and a limit cycle of twice the period is created. It is common for an infinite sequence of period-doubling bifurcations to occur over a finite range of parameter values. This is called a period-doubling cascade and is a common ‘route to chaos’, particularly for physiological systems.

The following two global bifurcations involve the collision of an equilibrium with a limit cycle and are of critical importance to the system studied in this thesis.

- Homoclinic bifurcation: This occurs when the stable and unstable manifolds of

a saddle equilibrium intersect. The intersection implies the existence of an orbit homoclinic to the equilibrium. For two-dimensional systems, generically a unique limit cycle is created on one side of the bifurcation (with period tending to infinity at the bifurcation because the limit cycle tends to the homoclinic orbit). In higher dimensions, homoclinic bifurcations can signal the onset of chaos, say if the equilibrium is a saddle-focus satisfying Shilnikov's condition (Kuznetsov, 1995).

- Saddle-node on an invariant circle (SNIC) bifurcation: This is a saddle-node bifurcation at which there exists an orbit homoclinic to the (non-hyperbolic) equilibrium. Generically a unique limit cycle is created on the side of the bifurcation where there are no equilibria locally, and with period tending to infinity at the bifurcation. It is also known as saddle-node infinite period (SNIPER) bifurcation.

A bifurcation analysis plays an essential part in understanding the dynamics of physiological models. Bifurcation diagrams are plots with a parameter of the system on the horizontal axis and a variable of the system (or sometimes some other useful measure) on the vertical axis. They consistently show the loss of stability of equilibria, the start and end of oscillations, and also depict how bifurcating branches are generated (Rinzel and Ermentrout, 1999; Govaerts et al., 2011; Shilnikov, 2012).

Under parameter variation excitable cells can transit from an excitable or rest state to an oscillatory regime in different ways and this can be nicely characterised using bifurcation theory. Rinzel and Ermentrout (1999) classify excitability into Type I and II based on the bifurcation type at the onset of firing. The classification is consistent with the original classification of Hodgkin (1948) where he studied the firing rate of a neuron relative to the injected current. In Type I excitability, the transition is through a saddle-node on an invariant circle (SNIC) bifurcation. The frequency of oscillations begin at an arbitrarily low value, and as the parameter is varied to move away from the bifurcation, the frequency of oscillations increases. This is because the period of

the corresponding limit cycle tends to infinity at a SNIC bifurcation (as discussed above). In contrast, for Type II excitability the transition from rest to an oscillatory state is through a Hopf bifurcation, in this case the oscillations emerge with non-zero frequency.

Transitions between types of excitability can be induced by some external factors such as external current (Tsumoto et al., 2006), addition of conductance (Drion et al., 2015), autapse (Zhao and Gu, 2017), and temperature (Xing et al., 2020). The classical Morris-Lecar model (1981) can exhibit both types of excitability. This has been well studied in the literature using a two-parameter bifurcation analysis (Rinzel and Ermentrout (1999); Govaerts and Sautois (2005)). The codimension-two bifurcations associated with a change between the two types of excitability were identified by Tsumoto et al. (2006) and Zhao and Gu (2017). Also, Duan et al. (2008) performed a similar two-parameter bifurcation analysis of the Chay neuronal model.

Despite many studies of pacemaker activity in SMCs, there does not appear to have been any detailed analysis about the types of excitability that can be exhibited. In the next section we show that our model can indeed exhibit both Type I and II excitability.

## 3.2 Codimension-One Bifurcation Analysis

Here we investigate how the dynamics of (2.2.6)–(2.2.7) change as we vary some of the parameter values from their values in Table 2.2. The bifurcation diagrams were produced using the numerical continuation software AUTO (Doedel et al., 2012) and edited in MATLAB. The abbreviations of the codimension-one bifurcations are given in Table 3.1. First we consider the effect of variation of  $\bar{v}_1$  with other parameters fixed as in Table 2.2. Figs. 3.1a–3.1c show the bifurcation diagrams of the full, reduced, and nondimensionalised models. It is seen that they are qualitatively similar, this shows that the dynamics of the full model is preserved by the reduced model which further



Table 3.1: Abbreviations and notations of codimension-one bifurcations.

Bifurcation	Abbreviation
Saddle-node	SN
Hopf bifurcation	HB
Saddle-node bifurcation of limit cycle	SNC
Saddle-node bifurcation on an invariant circle	SNIC
Homoclinic bifurcation	HC

justifies our reduction method in Sec. 2.2.1.

In Fig. 3.1c, we observe (2.2.6)–(2.2.7) has a unique equilibrium except between two saddle-node bifurcations,  $SN_1$  and  $SN_2$ . To the right of  $SN_2$  the lower equilibrium branch is the only stable solution of the system. The saddle-node bifurcation  $SN_2$  is in fact a SNIC bifurcation (saddle-node on an invariant circle) as here there exists an orbit homoclinic to the equilibrium. To the left of  $SN_2$  this orbit persists as a stable limit cycle. Thus here (2.2.6)–(2.2.7) model SMC activity with Type I excitability. As we pass through the SNIC bifurcation by decreasing the value of  $\bar{v}_1$  the excitable state changes to periodic oscillations. As shown in Fig. 3.1d the period of the oscillations decreases from infinity as a consequence of the homoclinic connection. Upon further decrease in the value of  $\bar{v}_1$  the stable limit cycle loses stability in a saddle-node bifurcation (SNC). The resulting branch of unstable limit cycles terminates in a subcritical Hopf bifurcation (HB). Between these bifurcations the system is bistable because the upper equilibrium branch is stable to the left of the Hopf bifurcation and coexists with a stable limit cycle.

Next we vary the value of the parameter  $\bar{v}_3$ . In the full model (2.1.1)–(2.1.8) transmural pressure is associated with the parameter  $v_6$ , so in the nondimensionalised model it is associated with  $\bar{v}_3$  through  $v_3^* = v_6 + \frac{v_5}{2}$ . Hence we can examine the influence of transmural pressure by using  $\bar{v}_3$  as a bifurcation parameter. As shown in Fig. 3.2a, as we increase the value of  $\bar{v}_3$  a unique equilibrium loses stability in a supercritical Hopf bifurcation  $HB_1$  then regains stability in a subcritical Hopf bifurcation  $HB_2$ . Therefore

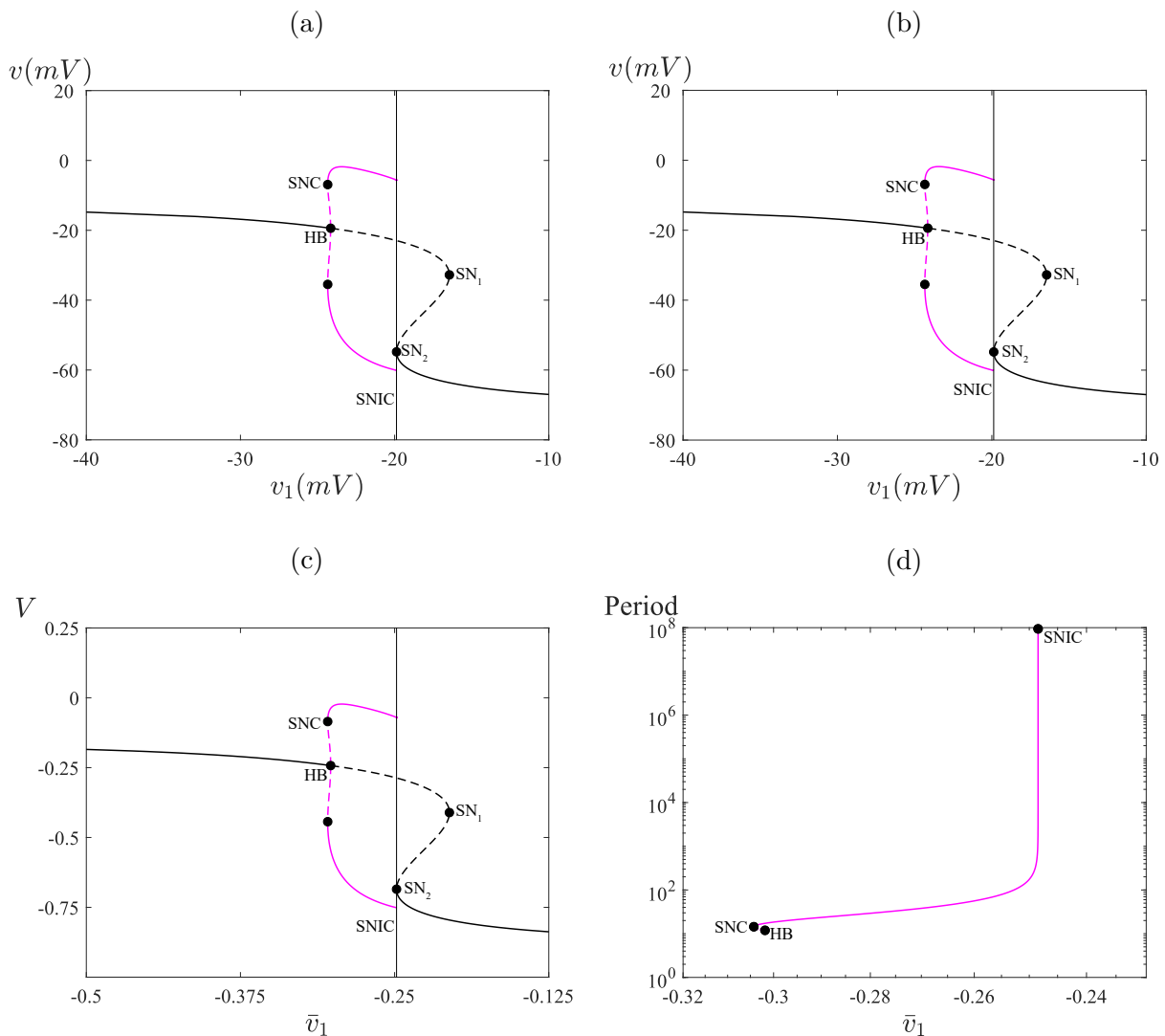


Figure 3.1: Bifurcation diagrams of (a) the full model (2.1.1)–(2.1.8) with  $v_1$  as the bifurcation parameter, (b) the reduced model (2.2.1)–(2.2.2) with  $v_1$  as the bifurcation parameter and (c) the nondimensionalised model (2.2.6)–(2.2.7) with  $\bar{v}_1$  as the bifurcation parameter. The remaining parameter values are given in Tables 2.1 and 2.2. Panel (d) shows the period of the oscillations in Fig. 3.1c for the nondimensionalised model. Black [magenta] curves correspond to equilibria [limit cycles]. Solid [dashed] curves correspond to stable [unstable] solutions. HB: Hopf bifurcation; SN: saddle-node bifurcation (of an equilibrium); SNC: saddle-node bifurcation of a limit cycle; SNIC: saddle-node on an invariant circle bifurcation.

in this case the system exhibits Type II excitability. The stable oscillations are created at  $\text{HB}_1$  with finite period (see Fig. 3.2b). They subsequently lose stability at the saddle-node bifurcation SNC and terminate at  $\text{HB}_2$ .

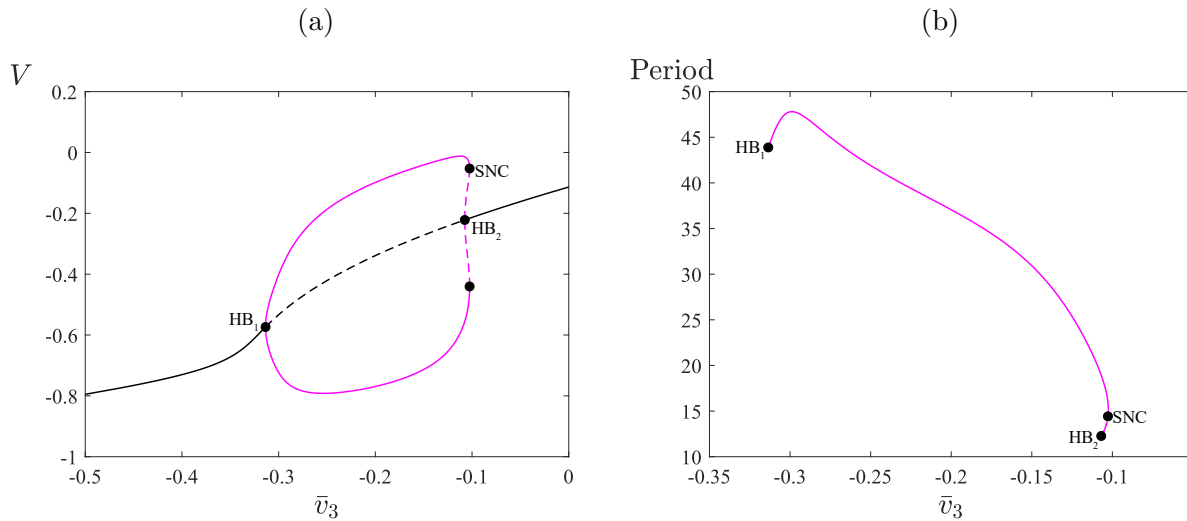


Figure 3.2: (a) A bifurcation diagram of the nondimensionlised model (2.2.6)–(2.2.7) with  $\bar{v}_3$  as the bifurcation parameter and other parameter values as given in Table 2.2. (b) A plot of the periodic oscillations as a function of parameter  $\bar{v}_3$ . The labels and other conventions are as in Fig. 3.1.

The influence of the other parameters associated with ion currents is highly important while investigating physiological activities in excitable cells thus we also consider the effect of  $\psi$ , the rate constant for the kinetics

of the potassium channel and  $v_L$ , the Nerst (reversal) potential of the leak current. Fig. 3.3a is a bifurcation diagram of the membrane potential  $V$  as  $\psi$  is varied. The model (2.2.6)–(2.2.7) has three equilibria for the values of  $\psi$  considered. For relatively low and intermediate values of  $\psi$ , there exist one stable (lower branch) and two unstable (upper and middle branch) equilibria. By increasing  $\psi$ , a stable period orbit emanates through an homoclinic bifurcation HC and upon further increase of  $\psi$ , the limit cycle terminates in a supercritical Hopf bifurcation HB. Between these bifurcations the system is bistable due to coexistence of stable periodic with a stable equilibrium lower

equilibrium branch. To the right of the HB there are two stable (upper and lower branch) and one unstable (middle branch) equilibria.

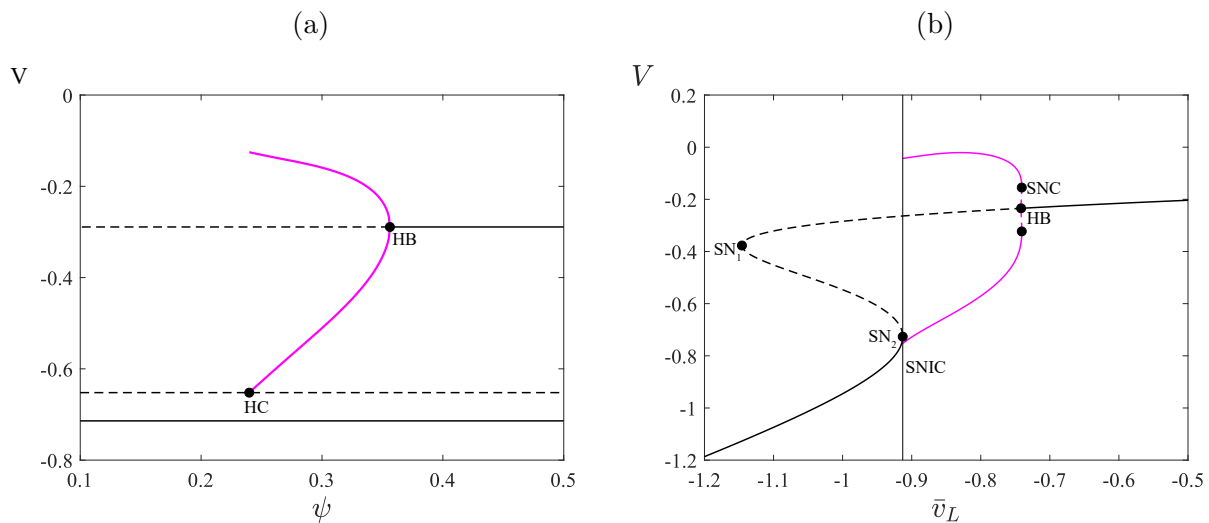


Figure 3.3: A bifurcation diagram of the nondimensionalised model (2.2.6)–(2.2.7) with (a)  $\psi$ ; (b)  $\bar{v}_L$  as the bifurcation parameter, and other parameter values as given in Table 2.2. The labels and other conventions are as in Fig. 3.1.

Lastly, variation of  $\bar{v}_L$  produces the bifurcation diagram Fig. 3.3b. This has the same type of bifurcation structure as Fig. 3.1b (except in reverse). Thus increasing the value of  $\bar{v}_L$  results in the same qualitative changes to the dynamics as decreasing the value of  $\bar{v}_1$ . In particular the excitability is Type I.

### 3.3 Codimension-Two Bifurcation Analysis

As seen in Sect. 3.2, system (2.2.6)–(2.2.7) can exhibit Type I or Type II excitability depending on choice of parameter values. Here we study this in detail and show transitions between the two types of excitability using a codimension-2 bifurcation analysis. Specifically we consider bifurcation sets in the  $(\bar{v}_1, \bar{v}_3)$  and  $(\bar{v}_1, \bar{v}_L)$  planes, respectively.

The abbreviations and notations of the codimension-2 bifurcations are summarised in Table 3.2 and discussed below.

Table 3.2: Abbreviations and notations of codimension-two bifurcations.

Codimension-2 bifurcation	Abbreviation	Label
Cusp bifurcation	$CP_i$	◻
Bogdanov-Takens bifurcation	$BT_i$	◊
Generalized Hopf bifurcation	$GH_i$	△
Resonant homoclinic bifurcation	RHom	◊
Non-central saddle-node homoclinic bifurcation	$NSH_i$	○

### 3.3.1 Bifurcations in $(\bar{v}_1, \bar{v}_3)$ -plane

A two-parameter bifurcation analysis of the model (2.2.6)–(2.2.7) varying the parameters  $\bar{v}_1$  and  $\bar{v}_3$  is illustrated in Fig. 3.4. It is produced from the loci of the codimension-1 bifurcations and contains five different codimension-2 bifurcation points: CP, BT, GH, RHom and NSH denoting the cusp point, Bogdanov-Takens bifurcation, generalised Hopf (Bautin) bifurcation, resonant homoclinic bifurcation, and non-central saddle-node homoclinic bifurcation, respectively.

Two of the one-parameter bifurcation diagrams described in Sect. 3.2 are slices of Fig. 3.4. Specifically Fig. 3.1c has the value of  $\bar{v}_3$  fixed at  $-0.1375$  and Fig. 3.2a has the value of  $\bar{v}_1$  fixed at  $-0.2813$ . Now we explore the consequences to transitions between Type I and II excitability by studying slices at six different values of  $\bar{v}_3$  in Fig. 3.4. Fig. 3.4 is divided into regions with eight qualitatively different types of dynamical behaviour, with enlargements in Fig. 3.5a, 3.6a, 3.8a and 3.8b. We have assigned each region a number and a colour, see Table 3.3.

For sufficiently large values of  $\bar{v}_3$  the only bifurcations are the two saddle-node bifurcations  $SN_1$  and  $SN_2$ , see Fig. 3.5a which shows a magnification of Fig. 3.4. A bifurcation

diagram corresponding to slice  $l_1$  for a fixed value of  $\bar{v}_3 = 0.45$  varying  $\bar{v}_1$  is shown in Fig. 3.5b. Thus for the slice  $l_1$  there are no periodic solutions. In this case, the system dynamics will pass through region ①  $\rightarrow$  ②  $\rightarrow$  ① as labelled in Fig. 3.5a as  $\bar{v}_1$  varies between  $-0.3$  and  $0.05$ .

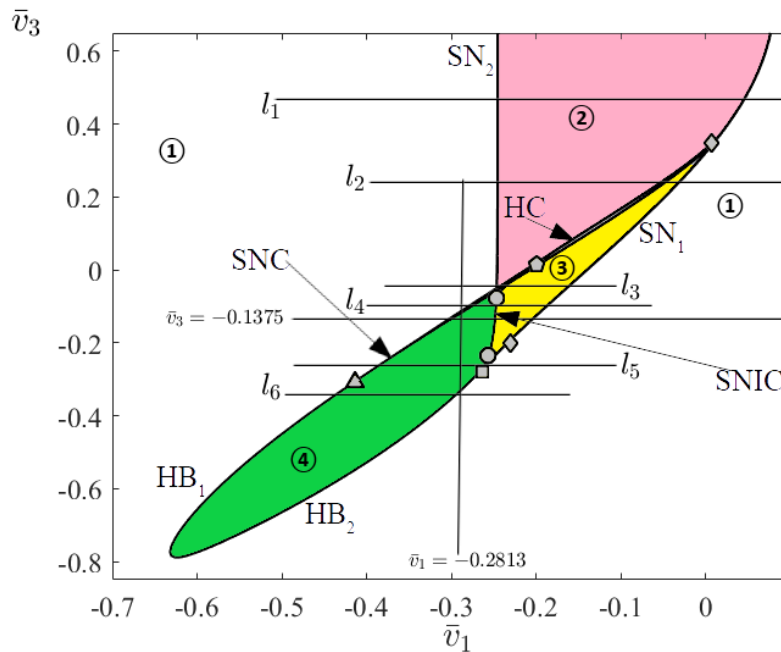










Figure 3.4: A two-parameter bifurcation diagram of the nondimensionalised model (2.2.6)–(2.2.7) in the  $(\bar{v}_1, \bar{v}_3)$ -plane for the parameter values of Table 2.2. The values of  $\bar{v}_3$  in  $l_1, l_2, l_3, l_4, l_5$  and  $l_6$  are  $0.45, 0.25, -0.047, -0.088, -0.26$  and  $-0.32$ , respectively. The black curves are the loci of codimension-one bifurcations labelled as follows: HB: Hopf bifurcation, SN: saddle-node bifurcation (or SNIC), HC: homoclinic bifurcation, and SNC: saddle-node bifurcation of limit cycle. The labels for the codimension-two bifurcations are explained in Table 3.2. The invariant sets that exist in each region are listed in Table 3.3.

Table 3.3: A summary of the eight different combinations of equilibria and limit cycles that arise in Fig. 3.4 and its magnifications, Figs. 3.5a, 3.6a, 3.8a, and 3.8b.

Region	Colour	Existence of equilibria and limit cycles
①		One stable equilibrium, no limit cycles (rest state).
②		Two stable equilibria, one unstable equilibrium, no limit cycles.
③		One stable equilibrium, two unstable equilibria, no limit cycles.
④		One unstable equilibrium, one stable limit cycle.
⑤		Two stable equilibria, one unstable equilibrium, one unstable limit cycle.
⑥		Two stable equilibria, one unstable equilibrium, one stable limit cycle, one unstable limit cycle (tristability).
⑦		One stable equilibrium, one stable limit cycle, one unstable limit cycle.
⑧		One stable equilibrium, two unstable equilibria, one stable limit cycle.

As we decrease the value of  $\bar{v}_3$  a Bogdanov-Takens bifurcation (Takens, 1974; Bogdanov, 1975), denoted  $BT_1$ , occurs on the saddle-node locus  $SN_1$  at  $\bar{v}_3 \approx 0.3792$ . This is a codimension-two point from which loci of homoclinic and subcritical Hopf bifurcations emanate, denoted  $HC$  and  $HB_1$ . As known from the theory of Bogdanov-Takens bifurcations (Kuznetsov, 1995) and as seen in Fig. 3.5a these loci are tangent to  $SN_1$  at the codimension-two point. Thus for a slice below  $BT_1$ , such as  $l_2$  for which  $\bar{v}_3 = 0.25$ , apart from the saddle-node bifurcations already observed there are now also homoclinic and Hopf bifurcations between which there exists an unstable limit cycle, Fig. 3.5c. Observe also that upon crossing  $BT_1$  the interval of values of  $\bar{v}_1$  in which the system is bistable changes from endpoints at  $SN_2$  and  $SN_1$  (for  $l_1$ ) to endpoints at  $SN_2$  and  $HB_1$  (for  $l_2$ ). The system in the case of line  $l_2$  goes through regions  $\textcircled{1} \rightarrow \textcircled{3} \rightarrow \textcircled{5} \rightarrow \textcircled{2} \rightarrow \textcircled{1}$  as  $\bar{v}_1$  decreases.

As the value of  $\bar{v}_3$  is decreased further,  $HB_1$  shifts to the left and a locus of saddle-node bifurcations of the limit cycle,  $SNC$ , emanates from the codimension-two point  $RHom$  on  $HC$  at  $\bar{v}_3 \approx 0.0095$ , see Fig. 3.6a. Thus below this point there exists a stable limit cycle between  $SNC$  and  $HC$ , such as for the slice  $l_3$ , Fig. 3.6b. For this slice, as the value of  $\bar{v}_1$  is decreased stable oscillations are created at  $HC$ . The system passes from region  $\textcircled{1} \rightarrow \textcircled{3} \rightarrow \textcircled{8} \rightarrow \textcircled{6} \rightarrow \textcircled{2} \rightarrow \textcircled{1}$ . Here there is a small region of tristability: stable oscillations coexist with two stable equilibria, see Fig. 3.7.

Upon further decrease of  $\bar{v}_3$  the locus  $HC$  collides tangentially with  $SN_2$  at the codimension-two point  $NSH_1$ . This is known as a non-central saddle-node homoclinic bifurcation, see for instance (Govaerts and Sautois, 2005). The collision produces the locus  $SNIC$ . Thus immediately below  $NSH_1$  the system exhibits Type I excitability. The system transitions from a stable equilibrium to a stable limit cycle at the  $SNIC$  bifurcation, such as for the slice  $l_4$ , Fig. 3.6c (and as described earlier, Fig. 3.1b). Thus the point  $NSH_1$  marks the onset of Type I excitability. This has been observed previously for the reduced Morris-Lecar model with external current (Tsumoto et al., 2006). For slice  $l_4$ ,



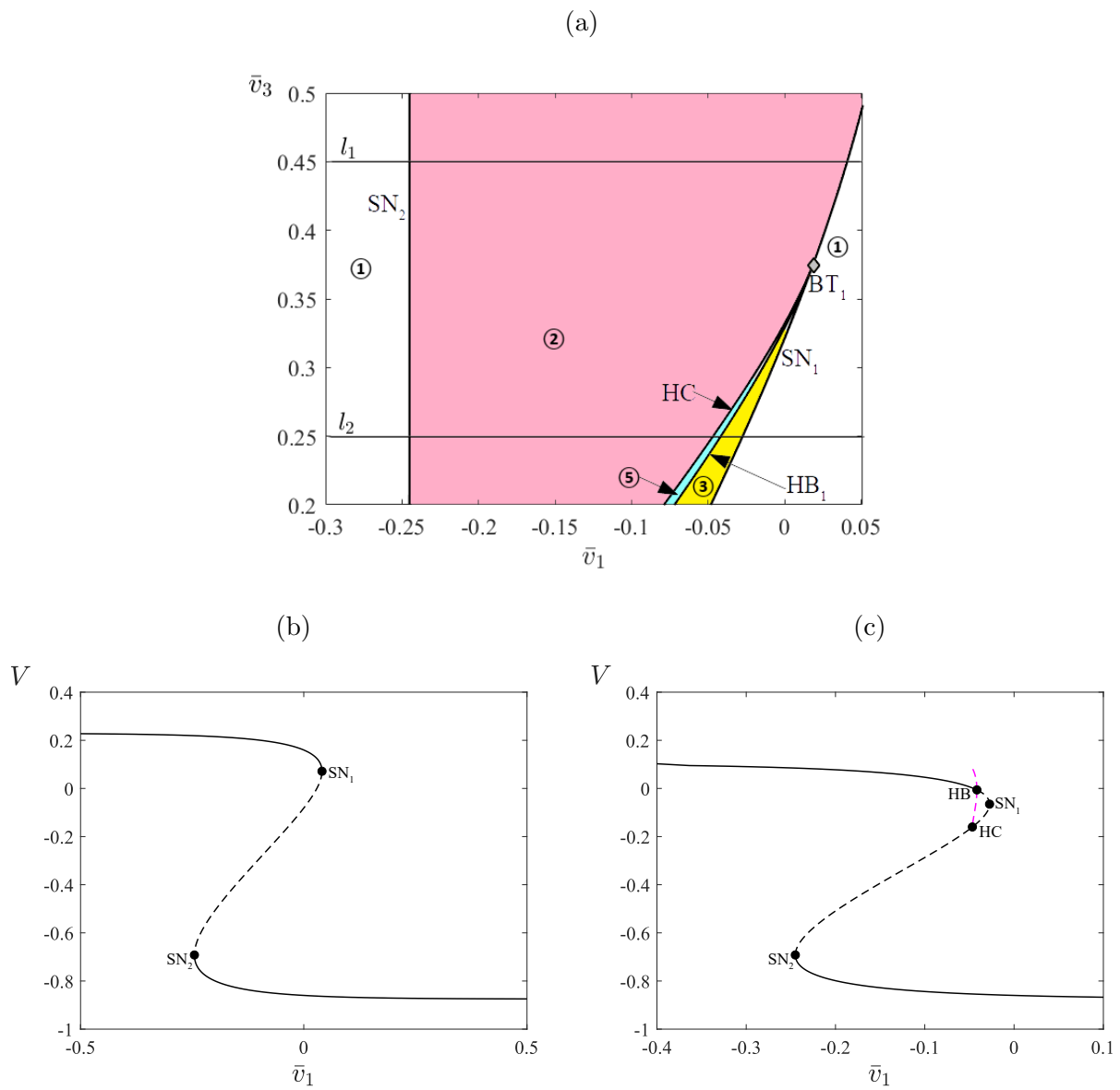


Figure 3.5: (a) An enlargement of Fig. 3.4 showing lines  $l_1$  and  $l_2$ . The filled diamond is a Bogdanov-Takens bifurcation. (b) A one-parameter bifurcation diagram along  $l_1$  with  $\bar{v}_3 = 0.45$ . (c) A one-parameter bifurcation diagram along  $l_2$  with  $\bar{v}_3 = 0.25$ . HB: Hopf bifurcation, SN: saddle-node bifurcation, SNC: saddle-node bifurcation of a limit cycle, HC: homoclinic bifurcation.

as  $\bar{v}_1$  decreases the system goes through region  $\textcircled{1} \rightarrow \textcircled{3} \rightarrow \textcircled{4} \rightarrow \textcircled{7} \rightarrow \textcircled{1}$  as labelled in Fig. 3.6a.

Upon further decrease to the value of  $\bar{v}_3$  a second Bogdanov-Takens bifurcation, denoted  $\text{BT}_2$ , occurs on the  $\text{SN}_1$  locus at  $\bar{v}_3 \approx -0.2429$  (see Fig. 3.8b). This generates loci of homoclinic and supercritical Hopf bifurcations. The homoclinic locus terminates nearby at another  $\text{NSH}_2$  bifurcation where the SNIC locus reverts to a locus of saddle-node bifurcations. The slice  $l_5$ , Fig. 3.8c, is below these two codimension-two points. Here the system exhibits Type II excitability as stable oscillations are created at the Hopf bifurcation. This shows that the transition between Type I and Type II excitability for the parameter regime we have considered is governed by the Bogdanov-Takens bifurcation  $\text{BT}_2$ , and this is in agreement with the result in (Zhao and Gu, 2017) where the authors studied bifurcation mechanisms induced by autapse in the Morris-Lecar model. As  $\bar{v}_1$  decreases, the system passes from region  $\textcircled{1} \rightarrow \textcircled{3} \rightarrow \textcircled{8} \rightarrow \textcircled{6} \rightarrow \textcircled{2} \rightarrow \textcircled{1}$  as labelled in Figs. 3.8a–b.

Finally, as  $\bar{v}_3$  is decreased further the Hopf locus  $\text{HB}_1$  changes from subcritical to supercritical at a generalised Hopf bifurcation at  $\bar{v}_3 \approx -0.2708$  and the saddle-node loci  $\text{SN}_1$  and  $\text{SN}_2$  collide and annihilate in a cusp bifurcation  $\text{CP}$  at  $\bar{v}_3 \approx -0.2727$ . Below these two codimension-two points the only bifurcations that remain are two supercritical Hopf bifurcations. The slice  $l_6$ , Fig. 3.9, shows a typical bifurcation diagram where the system passes through region  $\textcircled{1} \rightarrow \textcircled{4} \rightarrow \textcircled{1}$  as  $\bar{v}_1$  decreases. Here the excitability is Type II and there is no bistability.

From the analysis above, we see that the model (2.2.6)–(2.2.7) can transition between Type I and Type II excitability as  $\bar{v}_3$  varies. Thus, if we require to model SMC activity with Type I behaviour then we set  $\bar{v}_3$  values between  $\text{NSH}_1 \approx -0.0817$  and  $\text{NSH}_2 \approx -0.2586$ ; and if we require to model SMC activity with Type II activity we set  $\bar{v}_3 < \text{NSH}_2$ . For  $\bar{v}_3 < -0.7879$ , the system is neither Type I or Type II in the range of  $\bar{v}_3$  considered in this thesis.

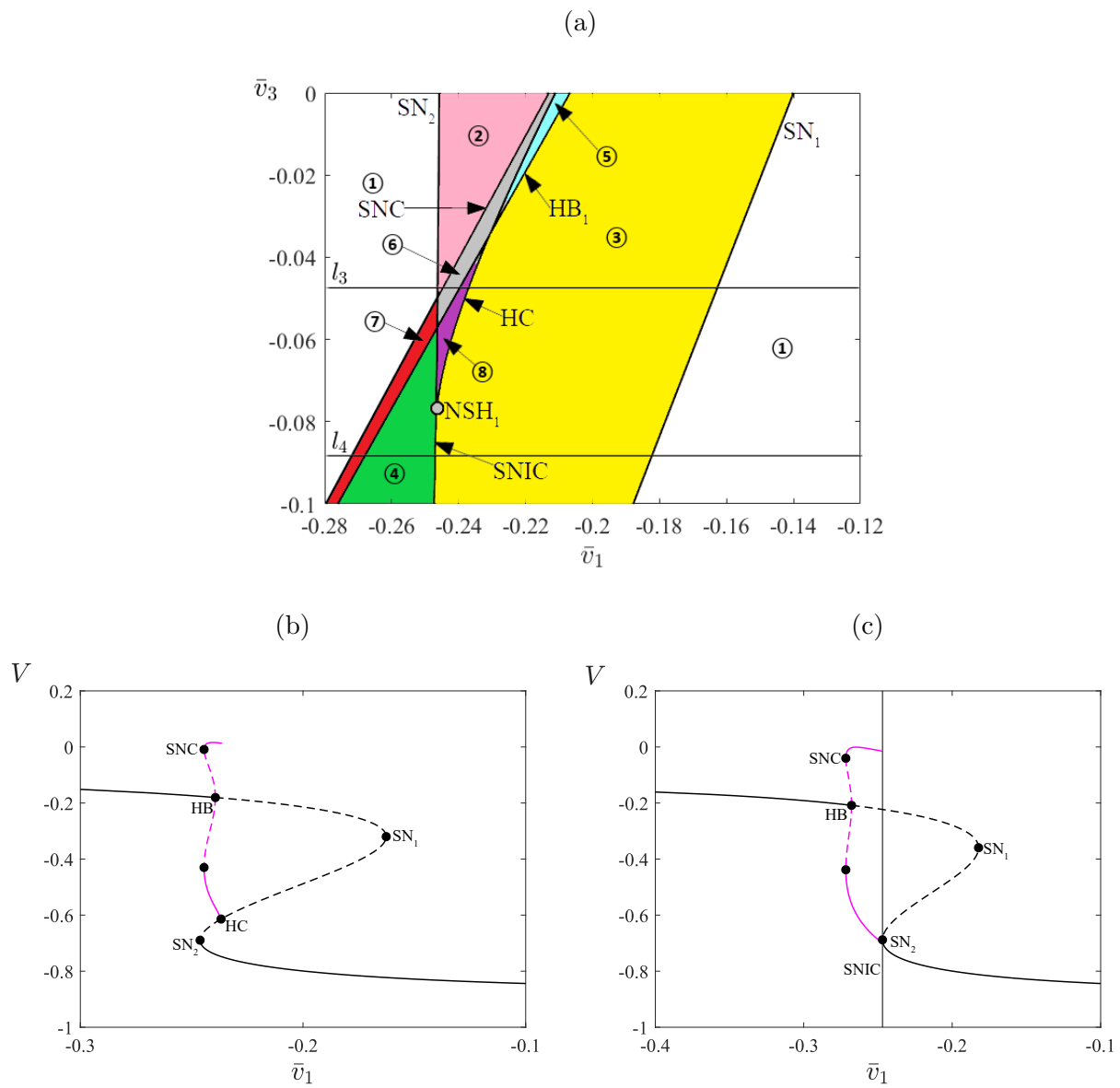


Figure 3.6: (a) An enlargement of Fig. 3.4 showing lines  $l_3$  and  $l_4$ . The filled circle is a non-central saddle-node homoclinic bifurcation. (b) A one-parameter bifurcation diagram along  $l_3$  with  $\bar{v}_3 = -0.047$ . (c) A one-parameter bifurcation diagram along  $l_4$  with  $\bar{v}_3 = -0.088$ . HB: Hopf bifurcation, SN: saddle-node bifurcation, SNC: saddle-node bifurcation of a limit cycle, SNIC: saddle-node on an invariant circle bifurcation, HC: homoclinic bifurcation.

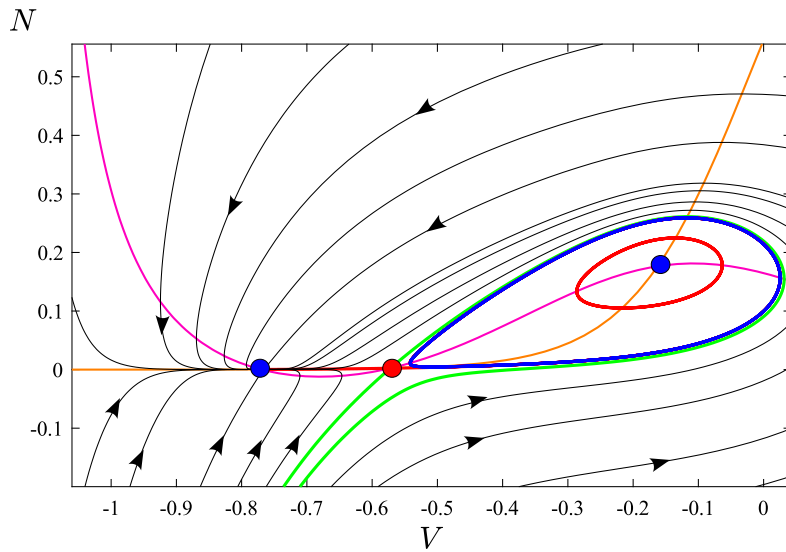


Figure 3.7: A phase portrait of the nondimensionalised model (2.2.6)–(2.2.7) on line  $l_3$  at  $\bar{v}_3 = -0.047$  showing tristability. The blue and red curves are stable and unstable limit cycles. The magenta and orange curves are the nullclines for  $N$  and  $V$ . The black curves are the solution trajectories. The blue and red circles are stable and unstable equilibria.

### 3.3.2 Bifurcations in $(\bar{v}_1, \bar{v}_L)$ -plane

Here we will investigate the range of  $\bar{v}_L$  for which the model (2.2.6)–(2.2.7) can transition between Type I and Type II excitability. Fig. 3.10a is the two-parameter bifurcation diagram in the  $(\bar{v}_1, \bar{v}_L)$  plane with enlargements in Figs. 3.10b and 3.10c. The black curves are the loci of codimension-one bifurcations labelled as in Fig. 3.4. It compose of eight different regions with dynamical behaviour qualitatively similar to regions ①–⑧ in Fig. 3.4. When other parameters are fixed with decreasing  $\bar{v}_L$ , it is seen in Fig. 3.10a that for sufficiently large values  $\bar{v}_L$  there exists two supercritical Hopf bifurcations  $HB_1$  and  $HB_2$ , between which there exists a stable limit cycle. This behaviour is characteristic of Type II excitability. As we decrease the value of  $\bar{v}_L$  a generalised Hopf bifurcation, denoted GH, occurs on the Hopf bifurcation  $HB_1$  at  $\bar{v}_L \approx -0.6955$ . At the GH point, the locus of saddle-node of limit cycle SNC emanates. Also  $HB_2$  changes from supercritical to subcritical. Below this point, apart from the two Hopf

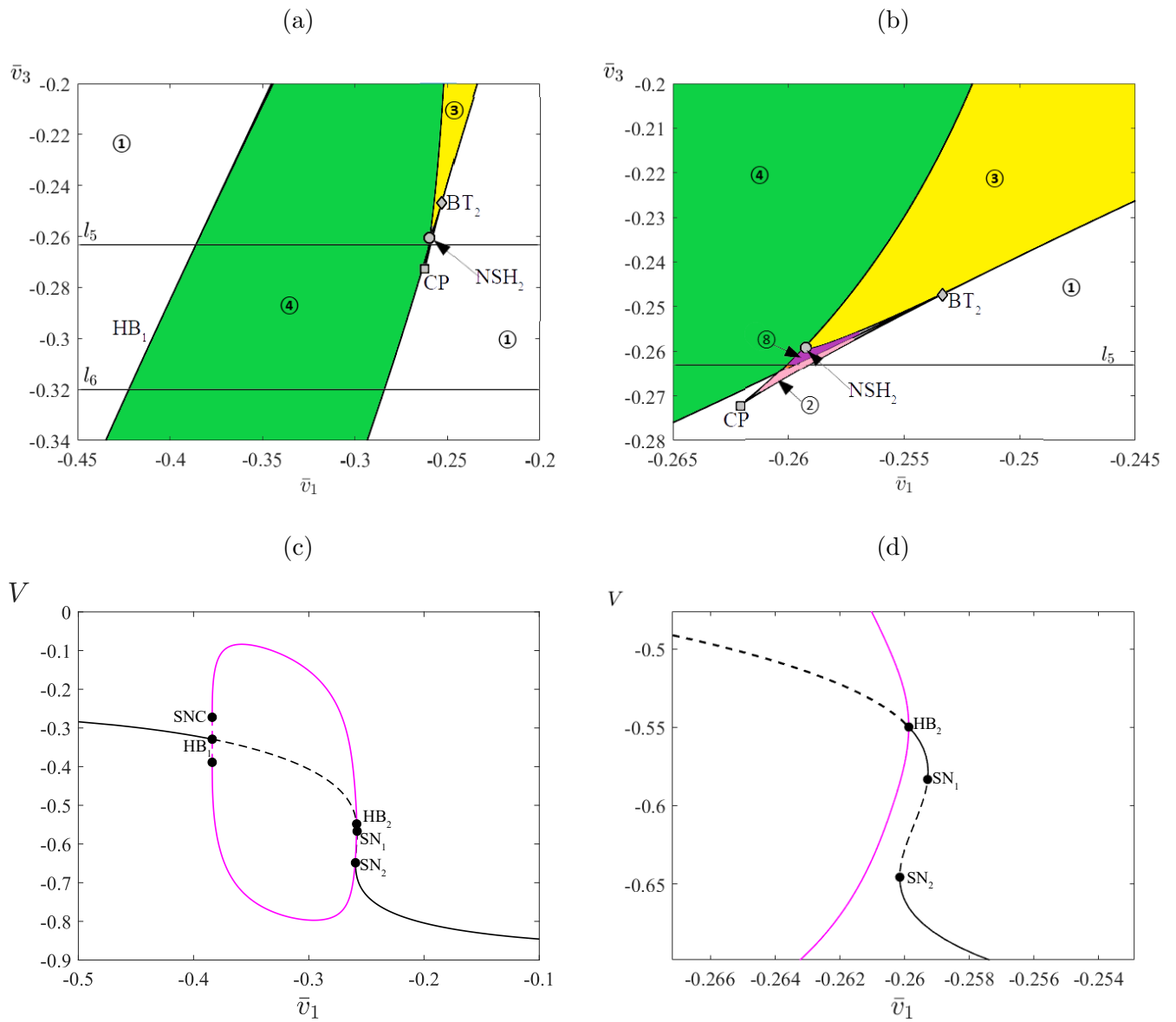


Figure 3.8: (a) An enlargement of Fig. 3.4 showing lines  $l_5$  and  $l_6$  (b) An enlargement of panel (a). (c) A one-parameter bifurcation diagram along  $l_5$  with  $\bar{v}_3 = -0.26$ . (d) An enlargement of panel (c). HB: Hopf bifurcation, SN: saddle-node bifurcation, SNC: saddle-node bifurcation of a limit cycle.

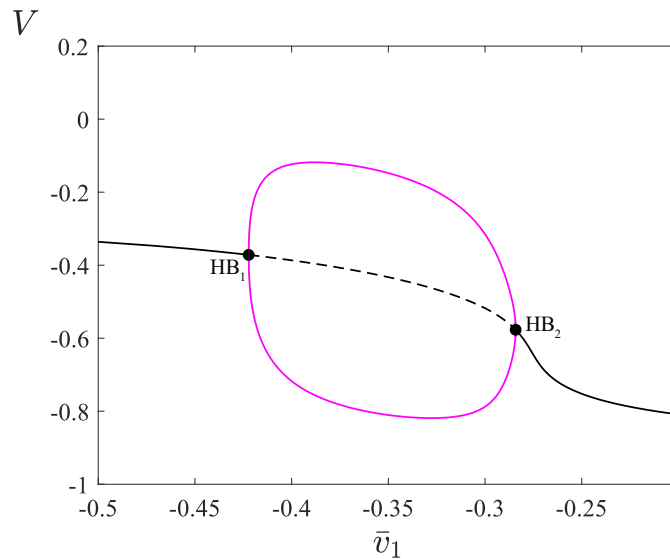


Figure 3.9: A one-parameter bifurcation diagram along  $l_6$  with  $\bar{v}_3 = -0.32$  (shown in Figs. 3.4 and 3.8a). HB: Hopf bifurcation.

bifurcations already observed there are now two saddle-node bifurcations  $SN_1$  and  $SN_2$  which collide and annihilate in a cusp bifurcation CP at  $v_L \approx -0.7620$ .

With decreasing  $\bar{v}_L$ , a Bogdanov-Takens bifurcation, denoted as  $BT_1$  appears on the saddle-node locus  $SN_1$  at  $\bar{v}_L \approx -0.7918$ . The loci of homoclinic and supercritical Hopf bifurcations emanate at  $BT_1$ . The locus of the homoclinic bifurcation HC collides with  $SN_2$  at a non-central saddle-node homoclinic bifurcation  $NSH_1$  to the locus of saddle-node on an invariant circle (SNIC). Thus below  $BT_1$  the system exhibits Type I excitability and this shows that model (2.2.6)–(2.2.7) transitions from Type II to Type I via the Bogdanov-Takens bifurcation  $BT_1$ . Upon further decrease in  $\bar{v}_L$  the SNIC locus terminates at the  $NSH_2$  bifurcation where the homoclinic locus emanates from the  $SN_2$  locus. The locus SNC that emanates from GH terminates on the locus HC at the resonant homoclinic bifurcation RHom.

Finally, as  $\bar{v}_L$  is decreased further the loci of homoclinic and Hopf bifurcations terminate at another the Bogdanov-Takens bifurcation,  $BT_2$ . Below  $BT_2$ , the only bifurcations that remains are the two saddle-node bifurcations  $SN_1$  and  $SN_2$ . Our results show

that to model Type II excitability SMC with (2.2.6)–(2.2.7) it requires  $\bar{v}_L$  values above  $NSH_1$ , whilst Type I excitability requires  $NSH_2 < \bar{v}_L < NSH_1$ .

### 3.4 Effect of Ion Conductances on Pacemaker Dynamics

In Chapter 2 we investigated the significance of maximal conductance of ion channels on the pacemaker dynamics of SMC model (2.1.1)–(2.1.8). By blocking the maximal conductances in turns, it was found that in the absence of leak current conductance  $g_L$  pacemaker activity persists, but does not persist if the conductances  $g_{Ca}$  and  $g_K$  for the  $Ca^{2+}$  and  $K^+$  currents are blocked (Fig. 2.5 shows an example). In this section we analyse the effect of each maximal conductance on pacemaker dynamics of model (2.2.6)–(2.2.7) independently through a bifurcation analysis. Also, we will analyse the model behaviour in response to modulation of transmural pressure in the absence of leak current ( $g_L = 0$ ).

Figure 3.11 shows the bifurcation diagram of the membrane potential  $V$  as  $g_L$ ,  $g_K$ , and  $g_{Ca}$  are varied. As seen in Fig. 3.11a, decreasing  $g_L$  results in the generation of stable periodic oscillations through a saddle-node on an invariant circle bifurcation, SNIC, and the limit cycle changes stability through a saddle-node of cycle, SNC. The unstable limit cycle terminates at the Hopf bifurcation HB. This behaviour corresponds to Type I excitability. Similar behaviour is observed qualitatively when  $g_{Ca}$  is considered as a bifurcation parameter except in reverse (see Fig. 3.11c). The bifurcation diagram of the membrane potential  $V$  with  $g_K$  as a bifurcation parameter is shown in Fig. 3.11b. The onset of periodic oscillations is via a subcritical Hopf bifurcation  $HB_1$  where the unstable periodic oscillations that emanate from  $HB_1$  changes stability at SNC. The stable period oscillations terminates at a supercritical Hopf bifurcation  $HB_2$ . Since the

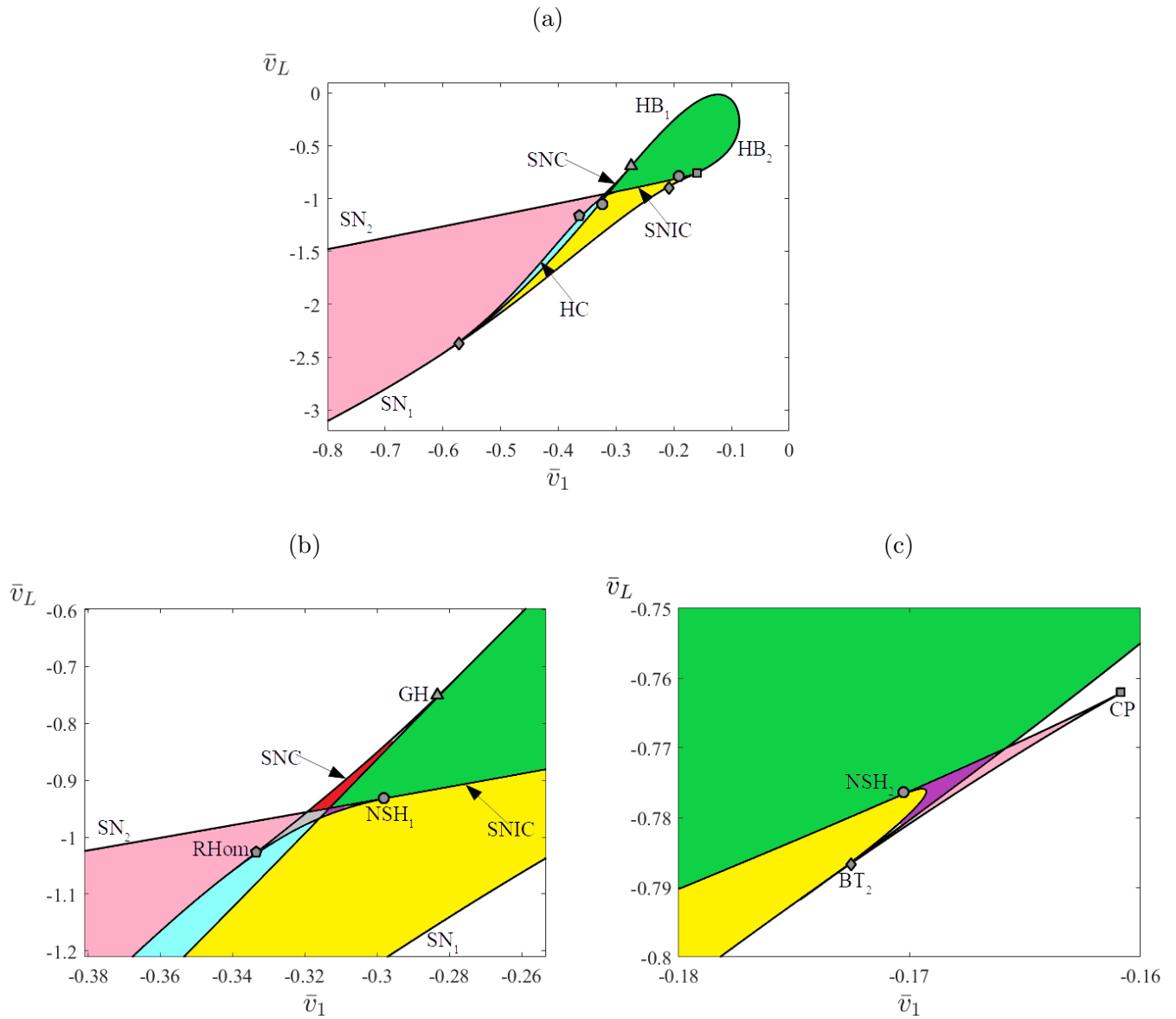


Figure 3.10: A two-parameter bifurcation diagram of the nondimensionalised model (2.2.6)–(2.2.7) in the  $(\bar{v}_1, \bar{v}_L)$ -plane. Other parameter values as in Table 2.2; (b) and (c) are enlargements of Fig. 3.10a. The labels and conventions are as in Fig. 3.4, Table 3.2 and Table 3.3.



oscillations begins at a Hopf bifurcation then the system exhibits Type II excitability in this case. In Fig. 3.11(a)–(c), the system is bistable between the saddle-node of cycles bifurcation SNC and the subcritical Hopf bifurcation HB; a stable limit cycle coexists with a stable equilibrium solution.

Now we want to investigate how the system transitions between the two types of excitability via two-parameter bifurcation analysis. Fig. 3.12 is a two-parameter bifurcation diagram of (2.2.6)–(2.2.7) in the  $(\bar{g}_{Ca}, \bar{g}_L)$ -plane with other parameter values fixed as in Table 2.2. The curves in Fig. 3.12 are loci of the saddle-node bifurcations  $SN_1$  and  $SN_2$ , Hopf bifurcations  $HB_1$  and  $HB_2$ , saddle-node of limit cycles bifurcation SNC, and the homoclinic bifurcation HC. Fig. 3.12 is divided into 6 parameter regions depicted by different colours. . It includes the same types of codimension-two bifurcations as those present in Fig. 3.4. Moreover the labels and conventions used here are the same as those used in Fig. 3.4 (see Table 3.2, Table 3.3). Fig. 3.12 shows that the model exhibits Type I excitability in the range  $0.2369 \leq \bar{g}_L \leq 0.40$ . For this parameter regime the Hopf bifurcation  $HB_2$  is subcritical. A Bogdanov-Takens bifurcation, denoted BT, occurs on the saddle-node locus  $SN_1$  at  $g_L \approx 0.2369$ . At the BT point, loci of homoclinic and Hopf bifurcations emanate, denoted HC and  $HB_1$ . The  $HB_1$  bifurcation in this case is supercritical and intersects with the locus of  $HB_2$  at a generalised Hopf bifurcation GH at  $\bar{g}_L \approx -0.0303$ . This is a codimension-2 point where supercritical changes to subcritical. The homoclinic locus collides tangentially with the  $SN_2$  locus at a non-central saddle-node homoclinic bifurcation NSH at  $\bar{g}_L \approx 0.2236$ . Finally, the saddle-node loci  $SN_1$  and  $SN_2$  collide and annihilate in a cusp bifurcation CP at  $\bar{g}_L \approx 0.0524$ . Below the CP point, the system has only the two Hopf bifurcations  $HB_1$  and  $HB_2$ . Hence for this parameter regime the model is Type II.

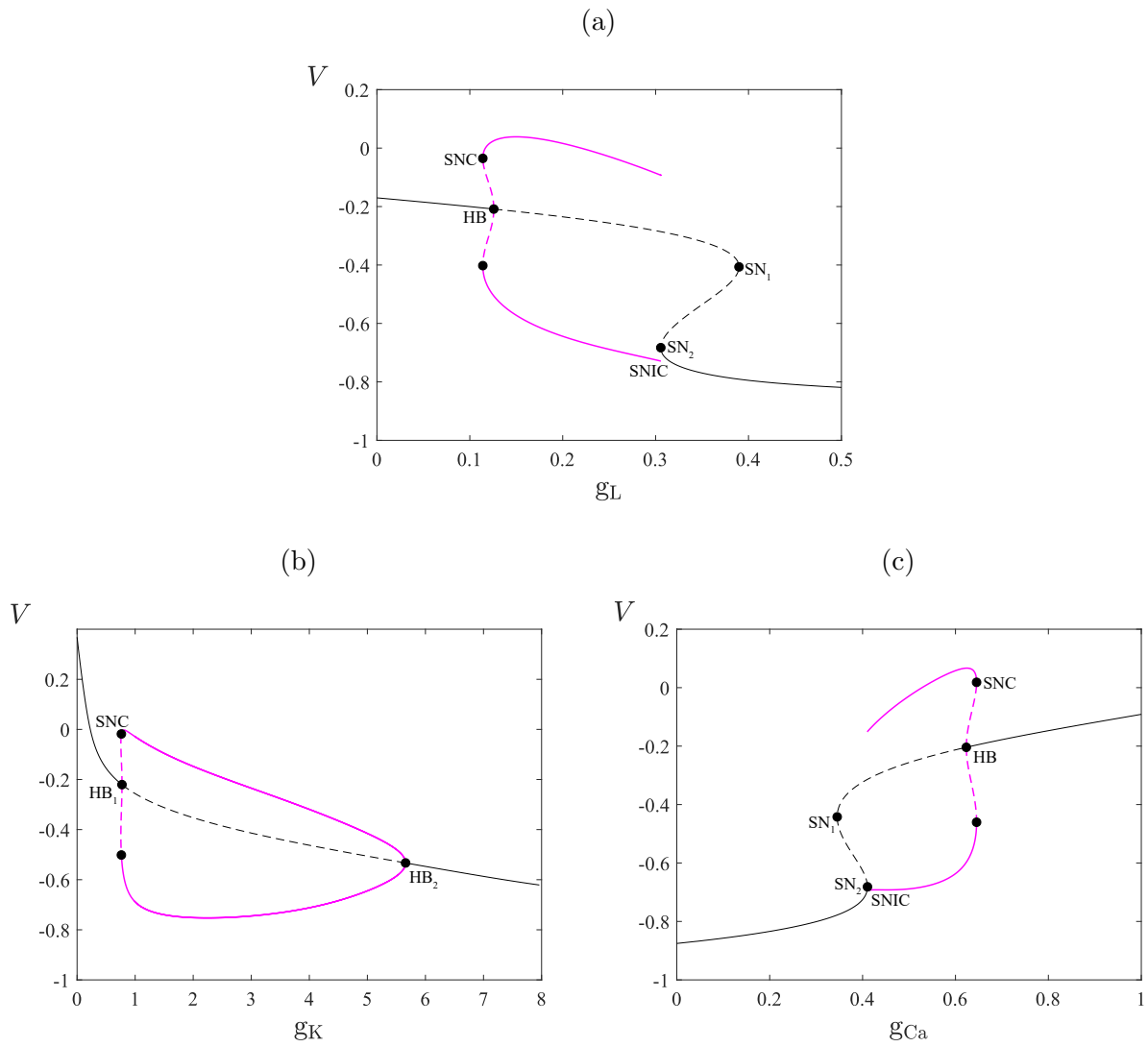


Figure 3.11: Further bifurcation diagrams of (2.2.6)–(2.2.7). The values of the remaining parameters as in Table 2.2.

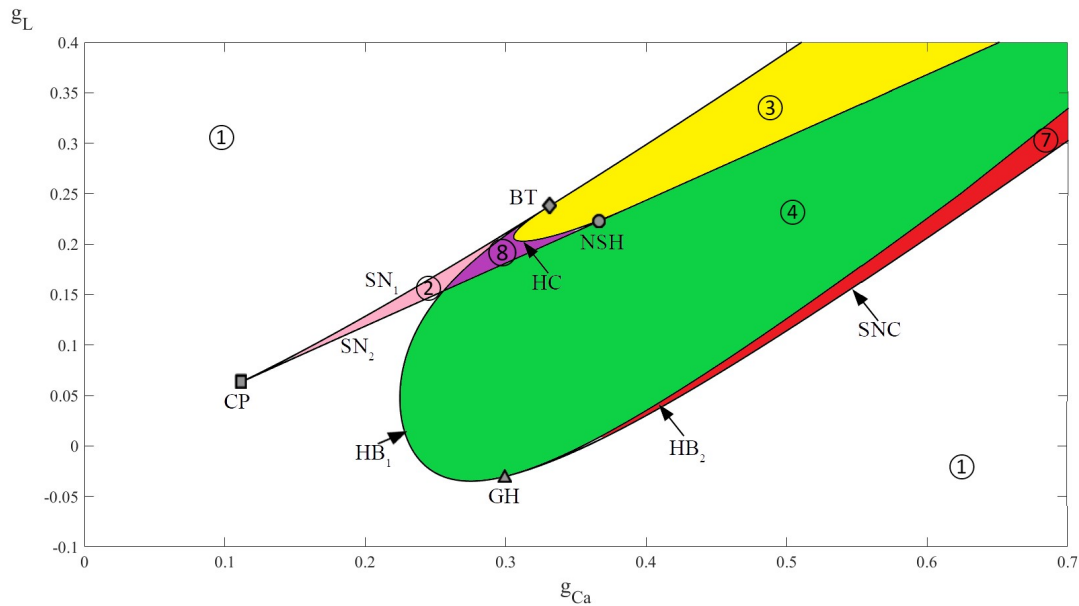


Figure 3.12: A two-parameter bifurcation diagram of the nondimensionalised model (2.2.6)–(2.2.7) in the  $(\bar{g}_{Ca}, \bar{g}_L)$ -plane. Other parameter values as in Table 2.2; The labels and conventions are as in Fig. 3.4, Table 3.2 and Table 3.3.

### 3.4.1 Pacemaker Dynamics in the Absence of Leak Conductance

Figure 3.13a is a one-parameter bifurcation diagram of (2.2.6)–(2.2.7) as  $\bar{v}_1$  is varied with  $g_L = 0$  and other parameters are fixed as in Table 2.2. At very low values of  $\bar{v}_1$ , the system has a unique stable equilibrium. Upon increasing  $\bar{v}_1$ , the system loses stability through a subcritical Hopf bifurcation  $HB_1 \approx -0.2617$ . The resulting unstable limit cycle changes stability in a saddle-node of cycles SNC at  $\bar{v}_1 \approx -0.2625$ . As  $\bar{v}_1$  further increases, the stable limit cycle branch ends in Hopf bifurcation  $HB_2$  at  $\bar{v}_1 \approx 0.0167$ . Since the onset of oscillations is through a Hopf bifurcation the excitability in this case is Type II (Rinzel and Ermentrout, 1999). This result is different compared to the case where  $\bar{g}_L$  is present in the model where we observed Type I excitability as  $\bar{v}_1$  is varied.

Now we consider  $\bar{v}_3$  as the bifurcation parameter keeping other parameters fixed as in

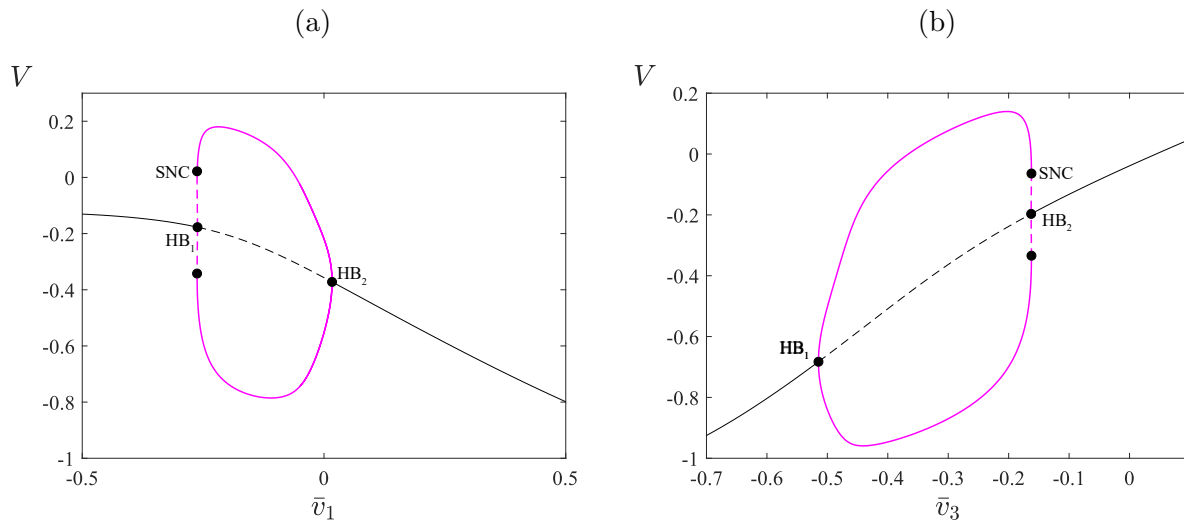


Figure 3.13: Bifurcation diagrams of (2.2.6)–(2.2.7) with other parameter values as given in Table 2.2. Solid (dashed) black curves represent stable (unstable) steady states. Solid (dashed) magenta curves denote the stable (unstable) limit cycles. HB: Hopf bifurcation, SNC: saddle-node of limit cycles.

Table 2.2. Variation of  $\bar{v}_3$  produces the bifurcation diagram in Fig. 3.13b. This has the same bifurcation structure as Fig. 3.13a except in reverse. Hence, increasing  $\bar{v}_3$  results in the same bifurcation points and qualitative changes to the dynamics as decreasing the value of  $\bar{v}_1$ .

Figure 3.14 shows a two-parameter bifurcation analysis of (2.2.6)–(2.2.7) in  $(\bar{v}_1, \bar{v}_3)$ -plane with enlargement in Fig. 3.14b. The curves are loci of the Hopf bifurcations,  $HB_1$  and  $HB_2$ , and saddle-node of limit cycles bifurcation SNC with variation of  $(\bar{v}_1$  and  $\bar{v}_3)$  simultaneously. There exist three regions with three qualitatively different types of dynamical behaviour, and the only codimension-two bifurcation observed is the generalised Hopf bifurcation GH.

For sufficiently large values of  $\bar{v}_3$  the system remains in a steady state as  $\bar{v}_1$  varies. For values of  $\bar{v}_3$  between  $[-1.015, 0.621]$  exist two Hopf bifurcations. Decreasing  $\bar{v}_3$  a generalised Hopf bifurcation, denoted  $GH_1$ , occurs on Hopf locus  $HB_1$  at  $\bar{v}_3 \approx 0.4909$ . At  $GH_1$ , the Hopf bifurcation  $HB_1$  changes from supercritical to subcritical. The SNC

locus emanating from  $\text{GH}_1$  ends in another generalised Hopf bifurcation denoted by  $\text{GH}_4$ , thus between  $\text{GH}_1$  and  $\text{GH}_4$  the Hopf bifurcation  $\text{HB}_1$  is subcritical. From Fig. 3.14 we conclude that when  $\bar{g}_L = 0$  (i.e. the leak channel is blocked) the system only exhibits Type II excitability. In contrast when  $\bar{g}_L$  takes the value in Table 2.1 the system exhibits both Type I and II excitability for what is otherwise for the same parameter set.

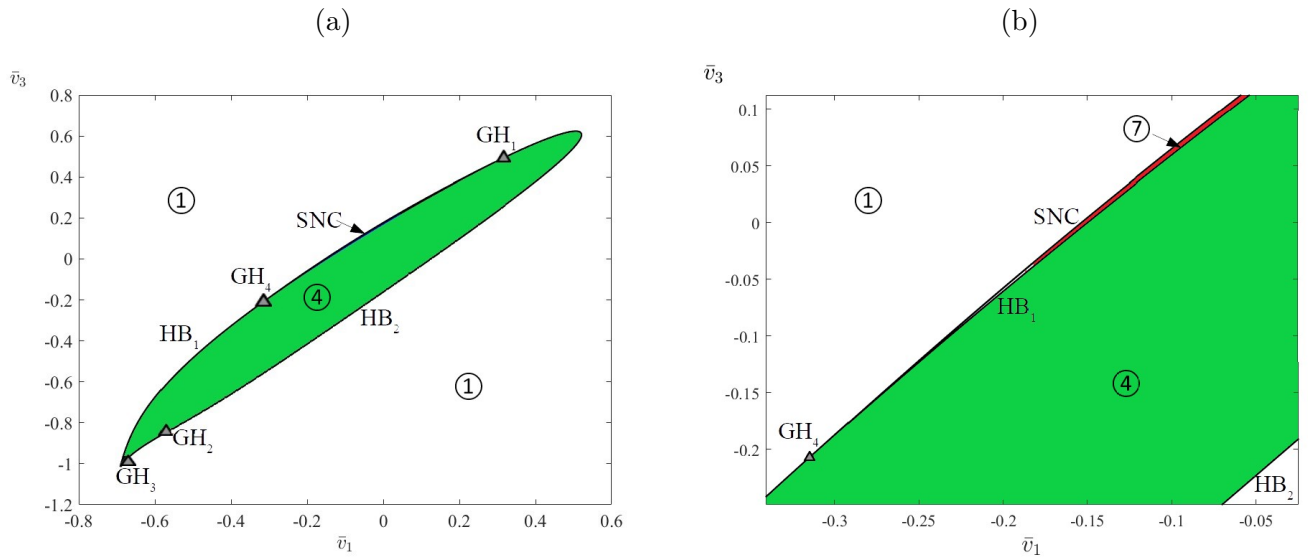


Figure 3.14: A two-parameter bifurcation diagram of the nondimensionalised model (2.2.6)–(2.2.7) in the  $(\bar{v}_1, \bar{v}_3)$ -plane. Other parameter values as in Table 2.2; (b) is enlargement of (a). The labels and conventions are as in Fig. 3.4, Table 3.2 and Table 3.3.

### 3.5 Discussion

The analysis of pacemaker dynamics in an isolated SMC model, namely (2.2.6)–(2.2.7) in the absence of diffusion, shows that our results are in agreement with results of non-pacemaker models in literature. This motivates us to further our investigation to gain more insights into physical significance of model parameters on dynamical behaviours of the model.

---

In the model,  $\bar{v}_1$  and  $\bar{v}_3$  are transmural pressure-dependent parameters, and are treated as the main bifurcation parameters, while  $\bar{v}_L$  and  $\psi$  are secondary bifurcation parameters. Under the parameter regimes considered, the system undergoes periodic oscillations through a SNIC bifurcation as  $\bar{v}_1$  is varied, meaning the model exhibits Type I excitability. Variation of  $\bar{v}_3$  results in periodic oscillations through a Hopf bifurcation, thus here the model exhibits Type II excitability. We investigated the transitions between types of excitability using a two-parameter bifurcation analysis and observed transitions in the  $(\bar{v}_1, \bar{v}_3)$  and  $(\bar{v}_1, \bar{v}_L)$  planes. These provide information on parameter values for which (2.2.6)–(2.2.7) can model SMC activity of either Type I or Type II excitability.

Finally in Sec. 3.4 we studied the effects of maximal conductances of ion channels on the pacemaker dynamics. It was shown that in the absence of leak conductance, the model exhibits only Type II behaviour in the parameter range considered.

## 4. Analysis of Coupled Model

Our goal is to gain insights into the collective behaviour of arterial SMCs due to electrical coupling between adjacent cells under the influence of changes in transmural pressure and concentration gradients of ions. In this chapter, we will analyse the nondimensionalised reaction-diffusion model (2.2.6)–(2.2.7) introduced in Chapter 2 to investigate the propagation of action potentials along a population of SMCs lining the vessel wall. We will review the linear stability analysis to show that the spatiotemporal pattern formation observed in the model is not due to diffusion-driven instability. Also, we will briefly describe the numerical method used to approximate the solutions of the model.

We conduct numerical simulations of diffusively coupled SMCs to study the spatiotemporal dynamics of the reaction-diffusion model. In particular, we examine the spatiotemporal patterns that arise over a range of parameters considered in previous chapters. Variation of model parameters results in wide range of spatiotemporal patterns including non-stationary irregular spatiotemporal patterns, travelling pulses, and fronts with irregular spatiotemporal oscillations. We will also study the effects of the initial conditions on spatiotemporal dynamics of the model.

### 4.1 Linear Stability Analysis

Alan Turing (1952) hypothesised that spatially inhomogeneous patterns may arise in a reaction-diffusion system if a spatially homogeneous steady state is stable in the absence of diffusion and destabilised as result of diffusion. Such instability is referred to as diffusion-driven instability or Turing instability. It has been established in recent years that spatiotemporal patterns in a reaction-diffusion system can arise from small perturbations to a spatially homogeneous steady state. In this section, we want show

if the possible spatiotemporal pattern in (2.2.6)–(2.2.7) is due to Turing-instability or whether it arises through some other mechanism.

Recall that our a reaction-diffusion system (2.2.6)–(2.2.7) is given by:

$$\begin{aligned} V_\tau &= \bar{D}V_{XX} + f(V, N), \\ N_\tau &= g(V, N), \end{aligned} \tag{4.1.1}$$

where  $f(V, N) = -\bar{g}_L(V - \bar{v}_L) - \bar{g}_K N(V - \bar{v}_K) - \bar{g}_{Ca} M_\infty(V)(V - 1)$  and  $g(V, N) = \lambda(V)(N_\infty(V) - N)$  are the reaction kinetics terms of  $V$  and  $N$ , and  $\bar{D}$  is a constant diffusion coefficient. We assume that the spatial domain is a finite interval,  $\Omega = [-L, L]$  for some  $L > 0$  and that  $V$  and  $N$  satisfy zero flux boundary conditions,

$$\frac{\partial V}{\partial X} = \frac{\partial N}{\partial X} = 0, \quad \forall X \in \partial\Omega. \tag{4.1.2}$$

Define  $(V^*, N^*)$  as a spatially stable homogeneous steady state of (4.1.1), if

$$\begin{aligned} V(X, \tau) &= V^*, \\ N(X, \tau) &= N^*, \end{aligned} \tag{4.1.3}$$

is a solution to (4.1.1) where  $V^*$  and  $N^*$  are constants. The steady state  $(V^*, N^*)$  can be found by solving the nonlinear system

$$f(V^*, N^*) = 0, \quad g(V^*, N^*) = 0.$$

Now we want to examine the linear stability of  $(V^*, N^*)$ . Let  $(V_0(X, \tau), N_0(X, \tau))$  be a perturbation from the steady state, i.e. let

$$\begin{pmatrix} V_0 \\ N_0 \end{pmatrix} = \begin{pmatrix} V - V^* \\ N - N^* \end{pmatrix}. \tag{4.1.4}$$



Substituting (4.1.4) into (4.1.1) and expanding  $f$  and  $g$  in Taylor series in  $V, N$  about  $(V^*, N^*)$  we get,

$$\begin{pmatrix} V_0 \\ N_0 \end{pmatrix}_\tau = \begin{pmatrix} D & 0 \\ 0 & 0 \end{pmatrix} \begin{pmatrix} V_0 \\ N_0 \end{pmatrix}_{XX} + \begin{pmatrix} f(V^*, N^*) & 0 \\ 0 & g(V^*, N^*) \end{pmatrix} + \begin{pmatrix} f_V & f_N \\ g_V & g_N \end{pmatrix} \begin{pmatrix} V_0 \\ N_0 \end{pmatrix} + \text{h.o.t.}, \quad (4.1.5)$$

We know  $f(V^*, N^*) = 0$  and  $g(V^*, N^*) = 0$ . Ignoring the higher order terms (h.o.t), we obtain the linearised system

$$\begin{pmatrix} V_0 \\ N_0 \end{pmatrix}_\tau = \begin{pmatrix} D & 0 \\ 0 & 0 \end{pmatrix} \begin{pmatrix} V_0 \\ N_0 \end{pmatrix}_{XX} + \begin{pmatrix} f_V & f_N \\ g_V & g_N \end{pmatrix} \begin{pmatrix} V_0 \\ N_0 \end{pmatrix}, \quad (4.1.6)$$

where  $\begin{pmatrix} f_V & f_N \\ g_V & g_N \end{pmatrix}$  is the Jacobian matrix evaluated at  $(V^*, N^*)$ .

We assume a solution of the form  $(V_0, N_0)(X, \tau) = \boldsymbol{\beta} e^{(\lambda\tau + ikX)}$ , where  $\boldsymbol{\beta}$  is a constant vector,  $k$  is the wave number. Substituting this into (4.1.6),

$$\begin{pmatrix} \lambda & 0 \\ 0 & \lambda \end{pmatrix} \boldsymbol{\beta} = \begin{pmatrix} -k^2 D & 0 \\ 0 & 0 \end{pmatrix} \boldsymbol{\beta} + \begin{pmatrix} f_V & f_N \\ g_V & g_N \end{pmatrix} \boldsymbol{\beta}, \quad (4.1.7)$$

after rearranging we have

$$\begin{pmatrix} -k^2 D + f_V - \lambda & f_N \\ g_V & g_N - \lambda \end{pmatrix} \boldsymbol{\beta} = 0. \quad (4.1.8)$$

Equation (4.1.8) is homogeneous in  $\boldsymbol{\beta}$ , thus it has nontrivial solution only if

$$\begin{vmatrix} -k^2 D + f_V - \lambda & -f_N \\ -g_V & g_N - \lambda \end{vmatrix} = 0. \quad (4.1.9)$$

The characteristic equation is

$$\lambda^2 - \lambda \left( -k^2 D + f_V + g_N \right) + \left( -k^2 D g_N + f_V g_N - g_V f_N \right) = 0, \quad (4.1.10)$$

with characteristic roots

$$\lambda = \frac{\tau}{2} \pm \frac{\sqrt{\tau^2 - 4\delta}}{2}, \quad (4.1.11)$$

where  $\tau = -k^2 D + f_V + g_N$  and  $\delta = -k^2 D g_N + f_V g_N - g_V f_N$ . The eigenvalues of the matrix are the temporal growth rates  $\lambda$ , by (4.1.10) they can be considered to be functions of  $k$ . In the absence of diffusion, we know that the spatially homogeneous steady state  $(V^*, N^*)$  is stable and therefore the following two conditions hold:

$$(1) f_V + g_N < 0, \quad (2) f_V g_N - f_N g_V > 0. \quad (4.1.12)$$

The steady state of the system with diffusion is unstable if  $\Re(\lambda(k)) > 0$  for some  $k \neq 0$ , this can happen if either  $-k^2 D + f_V + g_N > 0$  or  $-k^2 D g_N + f_V g_N - g_V f_N < 0$  for some  $k \neq 0$ . Since the diffusion coefficient  $D$  is non-negative the first condition in (4.1.12) ensures  $-k^2 D + f_V + g_N < 0$ , so we require  $-k^2 D g_N + f_V g_N - g_V f_N < 0$ . For this to happen  $D g_N$  must be positive as a necessary condition since the second condition in (4.1.12) is positive. In summary, the necessary conditions for diffusion-driven (Turing) instability to occur in (2.2.6)–(2.2.7) are:

- I.  $f_V + g_N < 0$
- II.  $f_V g_N - f_N g_V > 0$
- III.  $D g_N > 0$

Since  $(V^*, N^*)$  depends greatly on the reaction kinetics and model parameters,  $\delta$  can be positive or negative. We will consider the parameter regimes where we have observed a stable homogeneous steady state in the dynamics of our reaction kinetics. In the

case of the parameter  $\bar{v}_1$ , we will consider three parameter regimes: before the Hopf bifurcation  $\text{HB}_1$ , between the two saddle-node bifurcations  $\text{SN}_1$  and  $\text{SN}_2$  and to the right of  $\text{SN}_2$  on the bottom branch, see Fig. 3.1c. For all values of  $\bar{v}_1$  considered in this thesis,  $f_N < 0$ ,  $g_V > 0$ , and  $g_N < 0$ . For parameter regime  $\text{SN}_1 < \bar{v}_1 < \text{SN}_2$ , condition III is violated due to  $g_N = -\psi \cosh\left(\frac{V-\bar{v}_3}{2\bar{v}_4}\right) < 0$ , as  $\psi$  and the function  $\cosh\left(\frac{V-\bar{v}_3}{2\bar{v}_4}\right)$  are always positive, thus the conditions for diffusion-driven instability is not satisfied. Similarly, condition III is violated due to  $g_N < 0$  for  $\bar{v}_1$  below  $\text{HB}_1$  and  $\bar{v}_1$  above  $\text{SN}_2$  thus the diffusion-driven instability is not satisfied. Therefore, the spatiotemporal patterns that may arise in the reaction-diffusion system in (2.2.6)–(2.2.7) are not due to Turing instability.

## 4.2 Numerical Method

Different numerical techniques have been developed to approximate solutions for non-linear PDEs, for example, finite difference methods, finite element methods, finite volume methods, method of lines, and spectral methods (Cutlip and Shacham, 1998; Trefethen and Embree, 2005; Schiesser and Griffiths, 2009; Olsen-Kettle, 2011; John, 2013). We use the method of lines (MOL) technique to find approximate solutions to the reaction-diffusion system (2.2.6)–(2.2.7). This technique converts the PDE to a system of ODEs by the discretisation of the spatial variable while the time variable remains continuous. A numerical method for initial value ODEs is applied to approximate solutions to the PDE (Schiesser and Griffiths, 2009; Hiptmair et al., 2010). Using the centred difference and second order central finite difference approximation to approximate the first and second partial derivatives of the membrane potential  $V$  with respect to  $X$ , the approximation to the rate of change for some position  $X_i$  is given by

$$\frac{\partial V(X_i)}{\partial X} \approx \frac{V_{i+1} - V_{i-1}}{2\Delta X}, \quad (4.2.1)$$

and

$$\frac{\partial^2 V(X_i)}{\partial X^2} \approx \frac{V_{i+1} - 2V_i + V_{i-1}}{\Delta X^2}, \quad (4.2.2)$$

where  $\Delta X = \frac{2L}{M}$ , is the spatial step size and  $M$ , is number of grid points in  $X$ . Applying (4.2.1)–(4.2.2) to (2.2.6)–(2.2.7) leads to

$$\frac{dV_i}{d\tau} = D \frac{V_{i+1} - 2V_i + V_{i-1}}{\Delta X^2} - \bar{g}_L(V_i - \bar{v}_L) - \bar{g}_K N_i(V_i - \bar{v}_K) - \bar{g}_{Ca} M_\infty(V_i)(V_i - 1), \quad (4.2.3)$$

$$\frac{dN_i}{d\tau} = \psi \lambda(V_i)(N_\infty(V_i) - N_i), \quad 2 \leq i \leq M - 1. \quad (4.2.4)$$

Equations (4.2.3)–(4.2.4) are system of  $2M$  ODEs, before integrating the ODEs in  $\tau$ , we must consider the boundary and initial conditions imposed on the problem.

### 4.2.1 Boundary Conditions

For all simulations in this research we use zero flux boundary condition, i.e. the flux across the boundaries is zero. When  $i = M$ , (4.2.3) is defined as

$$\frac{dV_M}{dT} = D \frac{V_{M+1} - 2V_M + V_{M-1}}{\Delta X^2} - \bar{g}_L(V_M - \bar{v}_L) - \bar{g}_k N_M(V_M - \bar{v}_k) - \bar{g}_{Ca} M_\infty(V_M)(V_M - 1), \quad (4.2.5)$$

where  $V_{M+1}$  is a point outside the grid in  $X$ ; such a point is known as a fictitious point. For equation (4.2.5) to be integrated, we need to assign a value to  $V_{M+1}$ . Since the point at  $i = M$  is a boundary point, we can obtain the value of  $V_{M+1}$  by approximating the boundary conditions,  $\frac{\partial V}{\partial X} = \frac{\partial N}{\partial X} = 0$ , using the central difference approximation,

$$\frac{\partial V}{\partial X} \approx \frac{V_{M+1} - V_{M-1}}{2\Delta X} = 0. \quad (4.2.6)$$

This implies  $V_{M+1} = V_{M-1}$ , and substituting  $V_{M+1}$  into (4.2.5) we have:

$$\frac{dV_M}{d\tau} = D \frac{2(V_{M-1} - V_M)}{\Delta X^2} - \bar{g}_L(V_M - \bar{v}_L) - \bar{g}_k N_M(V_M - \bar{v}_k) - \bar{g}_{Ca} M_\infty(V_M)(V_M - 1). \quad (4.2.7)$$

Similarly for  $i = 1$ ,  $V_2 = V_0$  such that

$$\frac{dV_1}{d\tau} = D \frac{2(V_2 - V_1)}{\Delta X^2} - \bar{g}_L(V_1 - \bar{v}_L) - \bar{g}_k N_1(V_1 - \bar{v}_k) - \bar{g}_{Ca} M_\infty(V_1)(V_1 - 1). \quad (4.2.8)$$

Therefore, we integrate the ODE system for  $i = 2, \dots, M - 1$  using (4.2.3)–(4.2.4), and (4.2.7) and (4.2.8) for  $i = 1$  and  $i = M$ , respectively.

## 4.2.2 Initial Conditions

Since (4.2.2)–(4.2.3) is a system of  $M$  ODEs,  $M$  initial values are required for each of the two variables. They are given as

$$V(0, X_i) = V_0(X_i) \text{ and } N(0, X_i) = N_0(X_i), \quad 1 \leq i \leq M. \quad (4.2.9)$$

It has been widely observed that spontaneous spatially inhomogeneous patterns can be initiated through perturbation of homogeneous steady states (Murray, 2003; Zhang and Zang, 2014). For all numerical simulations we perturb the initial value of the variable  $V$  such that the initial conditions become

$$V_0(X_i) = V^* + G(X_i) \text{ and } N_0(X_i) = N^* \quad (4.2.10)$$

where  $V^*$  and  $N^*$  are homogeneous steady states of (2.2.6)–(2.2.7) and  $G(X_i)$ , a smooth function.

The numerical simulations are carried out in MATLAB using ODE45 to approximate

the solutions  $V_1(\tau), \dots, V_M(\tau)$  and  $N_1(\tau), \dots, N_M(\tau)$ . We approximate the solution behaviour on a suitably large domain  $\Omega = [-L, L]$ ; the spatial mesh size is  $\Delta X = \frac{2L}{M}$ . The diffusion coefficient  $D = 0.0001$  is chosen to be small relative to domain length so as to prevent the interference of the boundaries. Changing  $D$  is equivalent to rescaling space, and has no qualitative effect on the dynamics on an infinite domain therefore its value is kept constant in our simulations. The values of other parameters are fixed as in Table 2.2, unless otherwise stated.

### 4.3 Numerical Simulations

To observe spatiotemporal patterns in our simulation we perturbed the homogeneous steady state using the Gaussian function  $G(X_i) = A_0 \exp(-\frac{1}{2}(\frac{X_i - \mu}{\sigma})^2)$ , where  $A_0$  is the height of the curve,  $\mu$  is the centre, and  $\sigma$  determines the spread of the curve. In our simulations of (2.2.6)–(2.2.7) with  $A_0 = 0.3$ ,  $\mu = 0$ ,  $\sigma = 0.1$ , the Gaussian generally initiates a pulse at the centre of the domain, which splits into two pulses that travels across the domain in opposite directions as time progresses.

Variation of model parameters results in wide range of spatiotemporal patterns. Such patterns have been observed in chemical systems (Merkin and Sadiq, 1996; Merkin et al., 1996; Or-Guil et al., 2001), ecology (Kay and Sherratt, 1999; Pal et al., 2019), and neurons (Keplinger and Wackerbauer, 2014; Lafranceschina and Wackerbauer, 2014).

Figure 4.1a shows the behaviour of the system over a total simulation time of  $\tau = 500$  with parameter values fixed as in Table 2.2. For these parameters, in the absence of diffusion the system has a unique unstable equilibrium point surrounded by a stable periodic orbit (see Fig. 3.1c). In Fig. 4.1a, the solution is homogeneous in space and periodic in time except for the dynamics created by the Gaussian stimulus that initially splits into counter-propagating pulses at the centre of the domain. As time progresses, the pulse solutions destabilise, generating secondary pulses that travel inwards. The

resulting interactions induce a complicated patterned structure in a roughly triangular region bounded by the first two propagating pulses. The snapshot of the pulse solution for times  $\tau = 2, 20, 250$  is shown in Figs. 4.1b, 4.1c, and 4.1d, respectively.

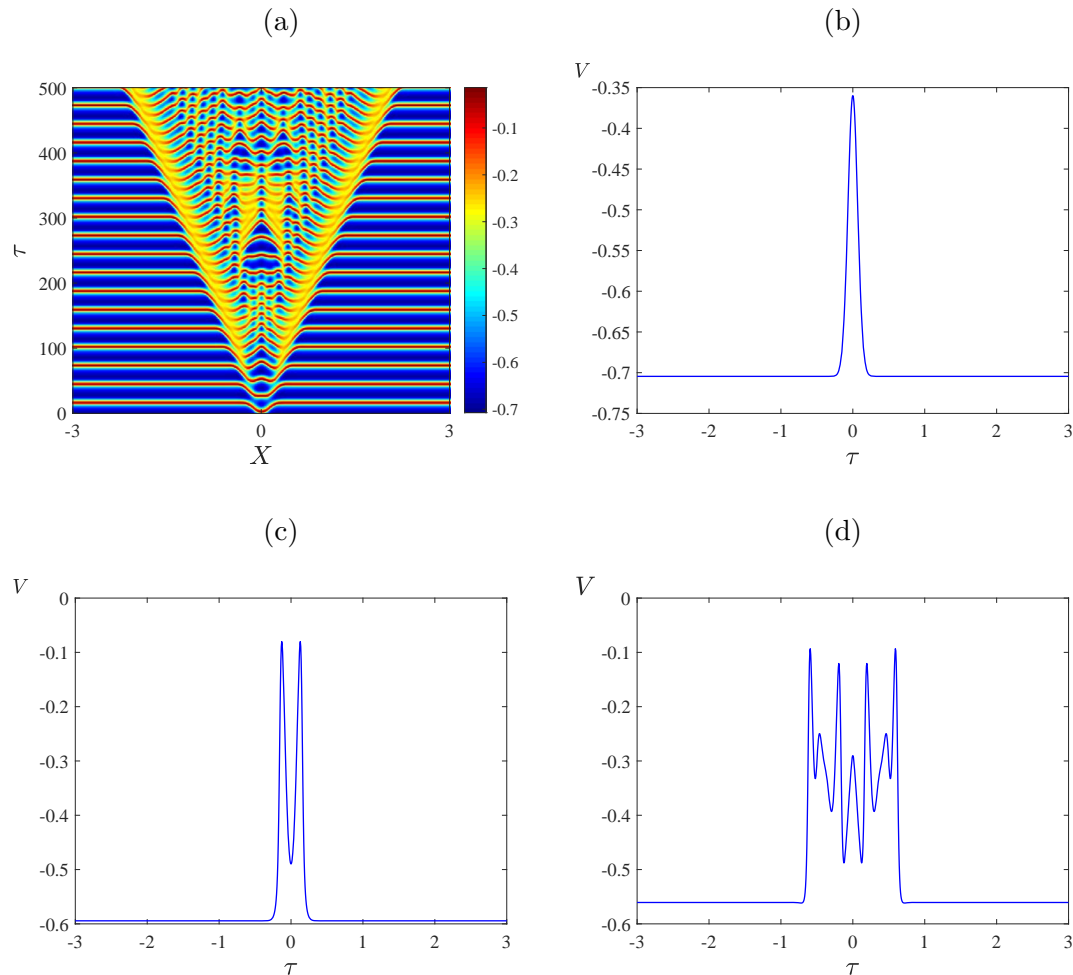


Figure 4.1: (a) Space-time plot of the membrane potential  $V$ ; (b)–(d) Spatial distribution of  $V$  at times  $\tau = 2, 20, 250$ . The parameter values are as in Table 2.2.

We found in Chapters 1 and 2 that the behaviour of the solutions is dependent on the parameters, for example a change in  $\bar{v}_1, \bar{v}_3$  and  $\psi$  can lead to different solutions. Thus in the next sections we will investigate the effect of varying the parameters on the spatiotemporal dynamics of (2.2.6)–(2.2.7). In Sect. 4.1 we showed that the patterns are not due to Turing instability, which required a stable steady state in the absence of diffusion. In our subsequent experiments, we will investigate spatiotemporal dynamics

for a wider range of parameter values, in particular where the steady state in absence of diffusion may be stable or unstable.

### 4.3.1 Spatiotemporal Patterns with varying $\bar{v}_1$

The system (2.2.6)–(2.2.7) in the absence of diffusion ( $D = 0$ ) undergoes a Hopf bifurcation, saddle-node bifurcation, and saddle-node on an invariant circle bifurcation as the parameter  $\bar{v}_1$  is varied, see Sec. 3.2. Transitions between these bifurcations demarcate changes in the behaviour of solutions and this can affect the spatiotemporal behaviour of coupled cells. To show the behaviour of the solutions we vary  $\bar{v}_1 \in [-0.5, -0.125]$ , keeping other parameters fixed. The spatiotemporal solutions of the membrane potential  $V$  for values  $\bar{v}_1$  close to bifurcation points are shown in Fig. 4.2.

For low values of  $\bar{v}_1$ , the solution quickly stabilises to the homogeneous steady state. A typical example is shown in Fig. 4.2b for which  $\bar{v}_1 = -0.325$  corresponding to the left the Hopf bifurcation HB. Increasing  $\bar{v}_1$  to the right of the Hopf bifurcation, an interesting spatiotemporal pattern is observed at  $\bar{v}_1 = -0.265$ . The solution starts as a pulse at the centre of the domain due to the initial perturbation. Then, as time progresses, the pulse splits into two propagating pulses that transition to time-periodic oscillations with inhomogeneous patterns at the back as they move across the domain, as in Fig. 4.2c. Increasing  $\bar{v}_1$ , similar solution behaviour is observed for the values of  $\bar{v}_1$  between the Hopf bifurcation HB and the saddle-node bifurcation  $\text{SN}_2$ . Figure 4.2d shows the spatiotemporal result at  $\bar{v}_1 = -0.25$ . The low frequency oscillations observed are due to a saddle-node on an invariant circle bifurcation, i.e. this value of  $\bar{v}_1$  is close to the  $\text{SN}_2$  bifurcation point.

Beyond  $\text{SN}_2$  the solution transitions from time-periodic oscillations to two pulses travelling in opposite directions. Again the initial Gaussian perturbation splits into two



pulses that destabilise resulting in irregular triangular patterns at the back of the primary pulses. Fig. 4.2e shows an example. Similar behaviour is observed for the value of close to the right of the  $SN_2$ . The initial perturbation induced traveling pulses that travelled in opposite directions and annihilated one another upon collision that results to the triangular patterns at the back of the pulses, as in Fig. 4.2f.

For relatively large values of  $\bar{v}_1$ , the system returns to the homogeneous steady state rapidly after perturbation. Similar behaviour is observed for some values of  $\bar{v}_1$  between the two saddle node  $SN_1$  and  $SN_2$  bifurcations. The solution behaviour to the left of  $SN_1$  (see Fig. 3.1c), specifically at  $\bar{v}_1 = -0.230$ , is shown in Fig. 4.2g.

The spatial distribution of the membrane potential  $V$  for these parameter values at different simulation times,  $\tau = 3, 15, 50, 125, 250, 500$  is shown in Fig. 4.3. This shows again how solution starts as a Gaussian pulse that splits into two pulses which destabilise to create secondary waves that travel in opposite direction to the initial pulses. As time progresses, the secondary waves collide with one another which results in instability across the domain, see Fig. 4.3.

### 4.3.2 Spatiotemporal Patterns with varying $\bar{v}_3$

Here we study the spatiotemporal behaviour of the model varying  $\bar{v}_3$  with other parameters fixed as in Table 2.2. Recall that in this case the system in the absence of diffusion exhibits supercritical and subcritical Hopf bifurcations, see Fig. 3.2a. Results of simulations for time up to  $\tau = 500$  are shown in Fig. 4.4. For extremely low values of  $\bar{v}_3$ , the system returns quickly to the homogeneous steady state after a initial perturbation at the centre of the domain. Fig. 4.4c shows the behaviour at  $\bar{v}_3 = -0.3019$  close to a supercritical Hopf bifurcation point. The system is in a quiescent state across the domain except at the centre where the Gaussian stimulation creates a simple pulse which turns to time periodic oscillations as time progresses. As  $\bar{v}_3$  increases, the solu-

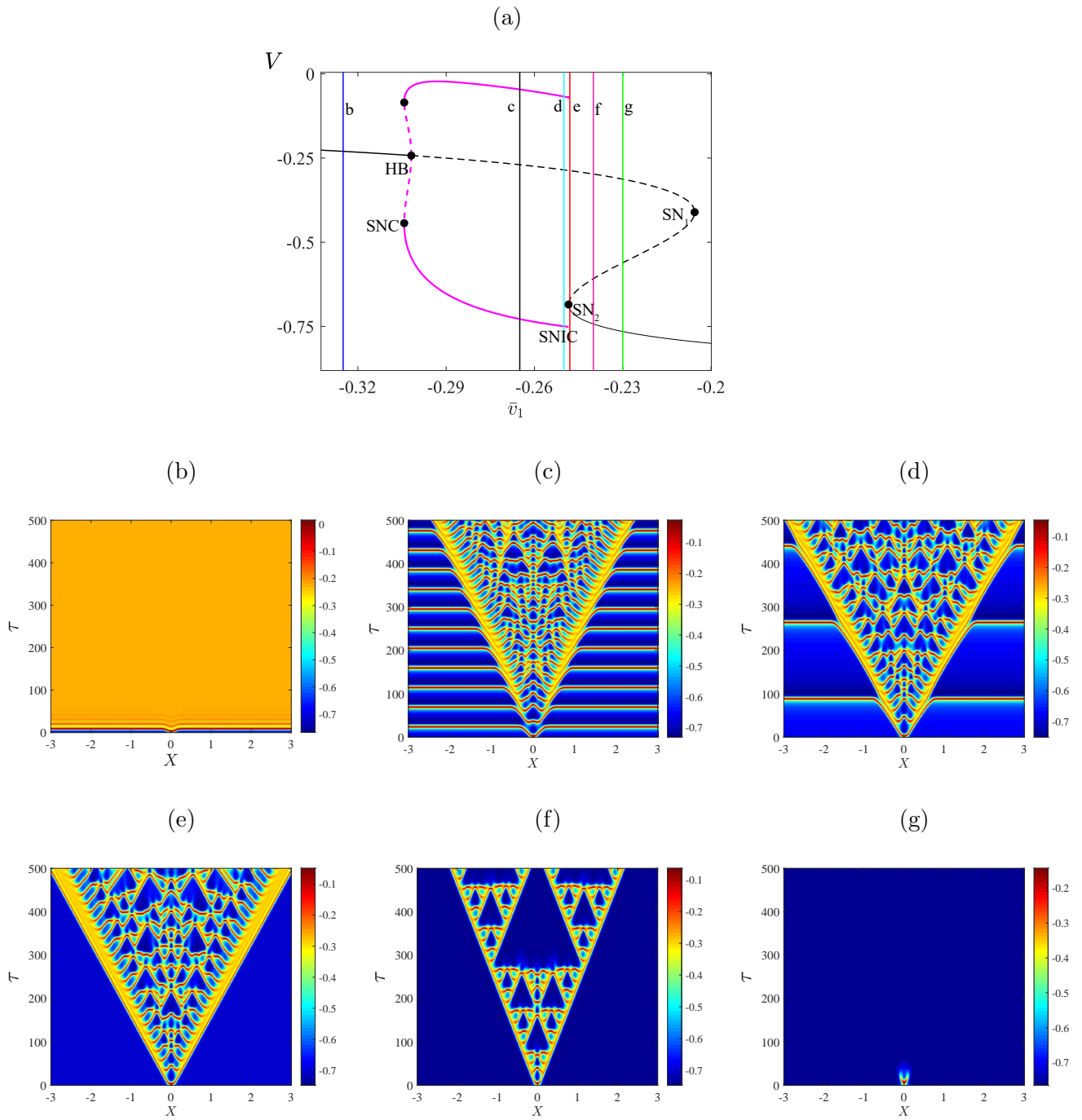


Figure 4.2: Space-time plots of the membrane potential  $V$ . (b)–(g):  $\bar{v}_1 = -0.325, -0.265, -0.25, -0.248, -0.240,$  and  $-0.230,$  respectively. Other parameters are fixed as in Table 2.2.

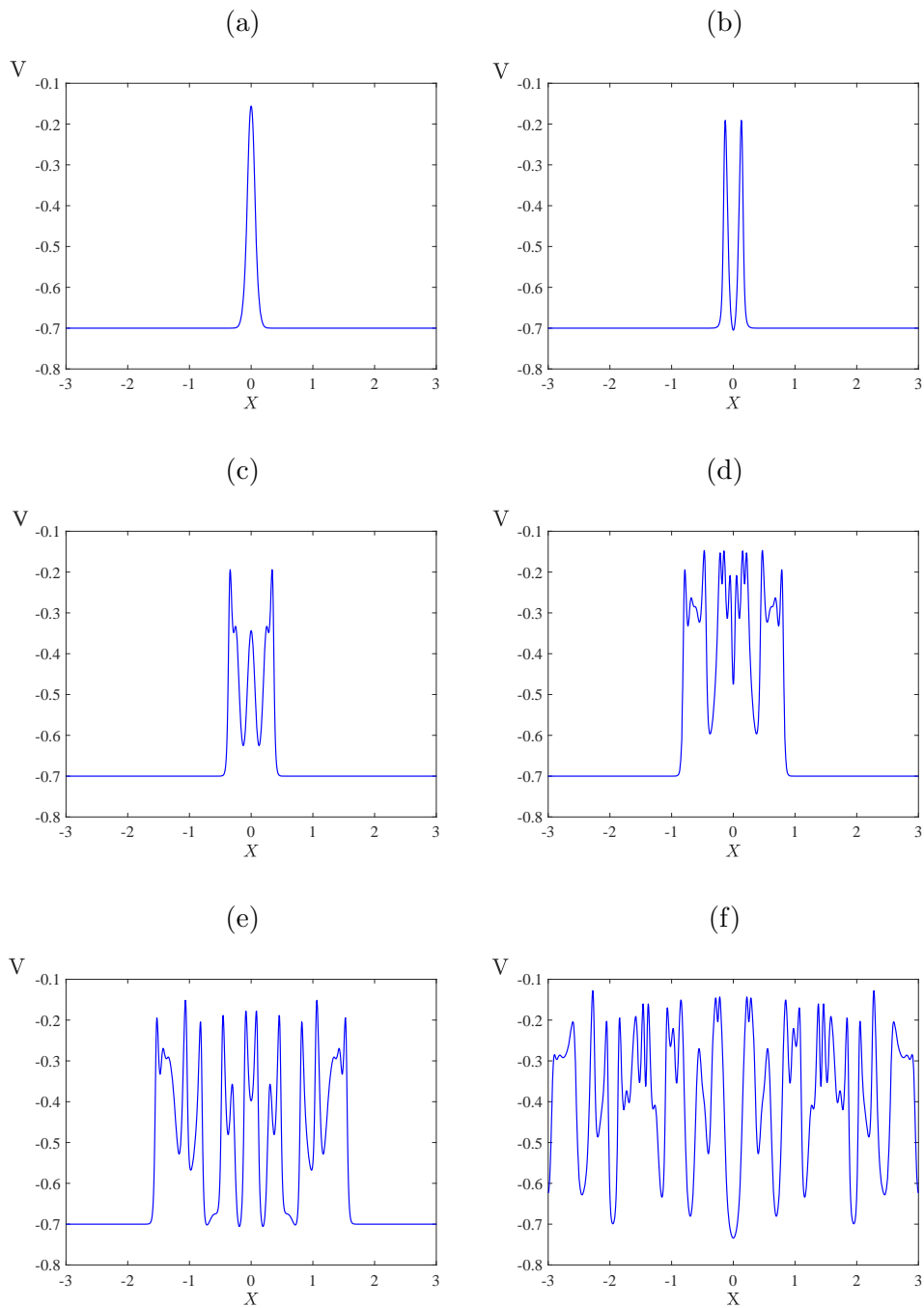


Figure 4.3: Spatial distribution of the membrane potential  $V$  for times  $\tau = 3, 15, 50, 125, 250, 500$  in Fig. 4.2e.

tions start as a simple pulse but as time progresses the action potentials propagate to the previously non-oscillatory region as observed in Fig. 4.4d at time  $\tau = 200$ .

The behaviour of the solutions for intermediate values of  $\bar{v}_3$  is shown in Fig. 4.4e. Apart from the pulse initiated by the Gaussian stimulus at the centre, time-periodic oscillations homogeneous in space are observed across the entire domain, and this corresponds to the stable limit cycle observed in this parameter regime in the bifurcation diagram in Fig. 3.2a for the uncoupled cell. Increasing  $\bar{v}_3$ , Fig. 4.4f depicts the solution behaviour before the subcritical Hopf bifurcation point. The system exhibits stable synchronised temporal oscillations across the entire domain except at the centre where the initial stimulus creates a pulse of propagating action potentials. As time progresses, secondary pulses emanate behind the main pulses and the secondary pulses collide to form irregular oscillations at the centre which eventually spread across the domain. As  $\bar{v}_3$  increases beyond the subcritical Hopf bifurcation point, periodic oscillations are observed for a short time across the entire domain, then stabilise to the homogeneous steady state, see Fig. 4.4g.

### 4.3.3 Spatiotemporal Patterns with varying $\psi$

As we saw in Fig. 3.3a, when the parameter  $\psi$  is increased for the system in the absence of diffusion, stable periodic oscillations are created in a homoclinic bifurcation and then are destroyed in a supercritical Hopf bifurcation. The spatiotemporal behaviour of solutions for various values of  $\psi$  is shown in Fig. 4.5. For extremely low values of  $\psi$ , the initial perturbation created a pulse at the centre of the domain and as time progresses the pulse splits into two travelling pulses propagating in opposite direction at the same speed. A slight increase in  $\psi$  leads to a destabilisation of the pulses that results in an initiation of secondary pulses travelling in the opposite direction to the primary pulses. Increasing  $\psi$  further results in the collision of the secondary pulses

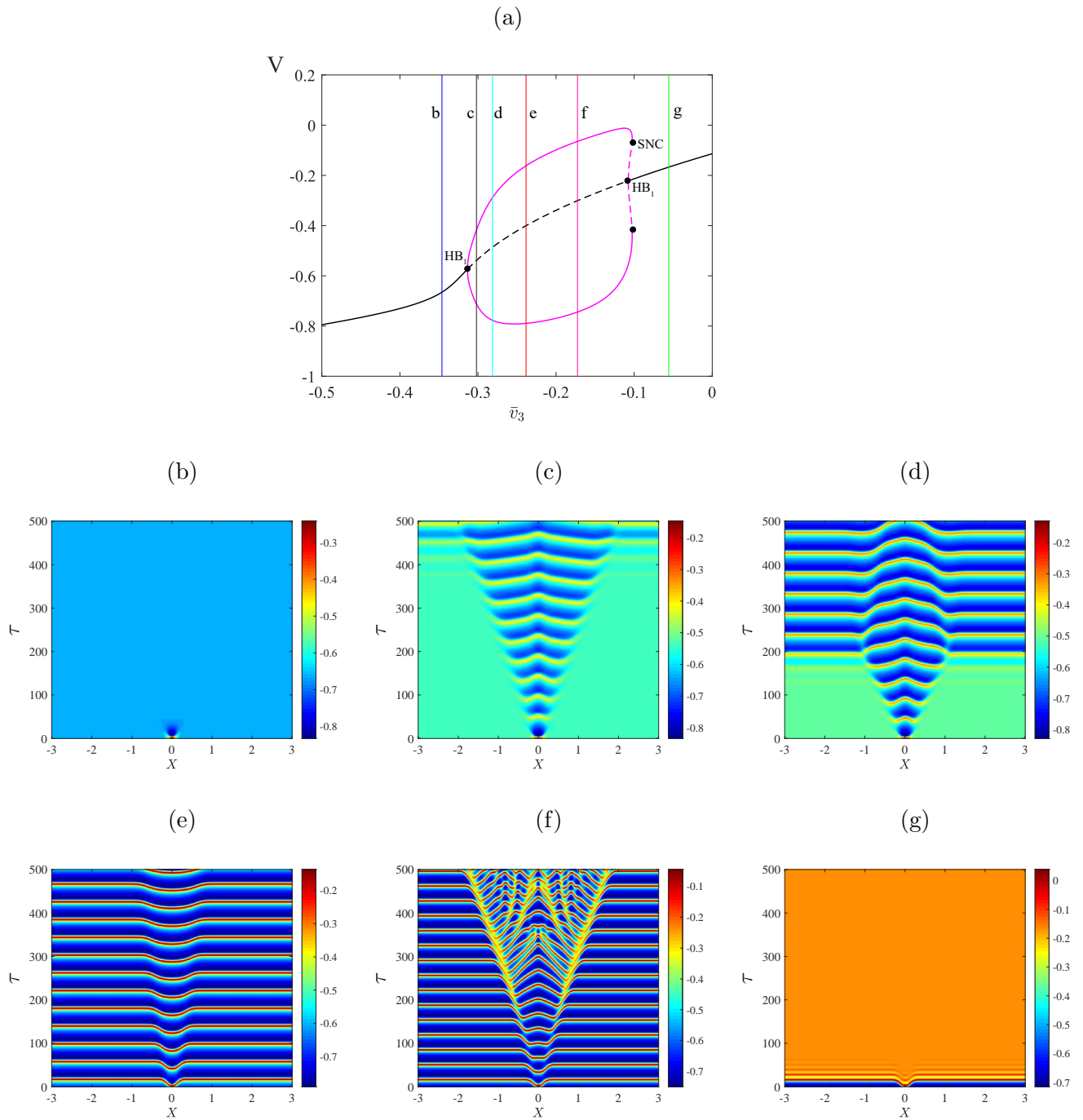


Figure 4.4: Space-time plots of the membrane potential  $V$ . (b)–(g):  $\bar{v}_3 = -0.3462, -0.3019, -0.2813, -0.23842, -0.1725,$  and  $-0.05565$ , respectively. Other parameters are fixed as in Table 2.2.

and eventually irregular oscillations occur across the spatial domain. Interestingly, as  $\psi$  varies past the homoclinic bifurcation, the unstable pulses transition to travelling fronts connecting a stable steady state to an unstable state with irregular oscillations at the back of the fronts. However, as  $\psi$  increases further, the upper unstable branch changes stability at a supercritical Hopf bifurcation so beyond the Hopf bifurcation point the system has two stable steady-state solutions. Finally, for large values of  $\psi$  the solution eventually transitions to travelling fronts propagating in opposite directions. In this case the front connects the two stable steady states shown in Fig. 3.3a. The solution profile at time  $\tau = 300$  shows the transitions from travelling pulses to complex spatiotemporal patterns to travelling fronts as  $\psi$  is varied.

#### 4.3.4 Effect of Changing the Initial Perturbation

In this section, we change the initial perturbation to investigate the effect of initial conditions on the qualitative behaviour of solutions. Fig. 4.7 shows the spatiotemporal patterns observed in the model varying  $\bar{v}_1$  with other parameters fixed and initial stimulus  $G(X_i) = \epsilon X_i$ , where  $\epsilon$  is a small number. For low values of  $\bar{v}_1$ , the system returns quickly to the homogeneous steady state after a short sequence of periodic oscillations. By increasing  $\bar{v}_1$ , we observed a pulse (wave train) of propagating action potentials moving across the domain as time progresses. Specifically, examples of such behaviour are illustrated in Fig. 4.7b and Fig. 4.7c. This behaviour corresponds to the stable periodic orbit observed in the bifurcation diagram of the uncoupled cell (see Fig. 3.1c). As  $\bar{v}_1$  increases further, the solution transitions to single pulse that propagates across the domain, and as time progresses a counter propagating pulse emanates from behind the pulse. Behind the already existing two pulses are secondary pulses travelling in opposite directions to the primary pulses, and collision of the secondary pulses result in irregular oscillations that spread across the domain. Fig. 4.7d and Fig. 4.7e are behaviour of solutions near the saddle-node on an invariant circle (SNIC) bifurcation

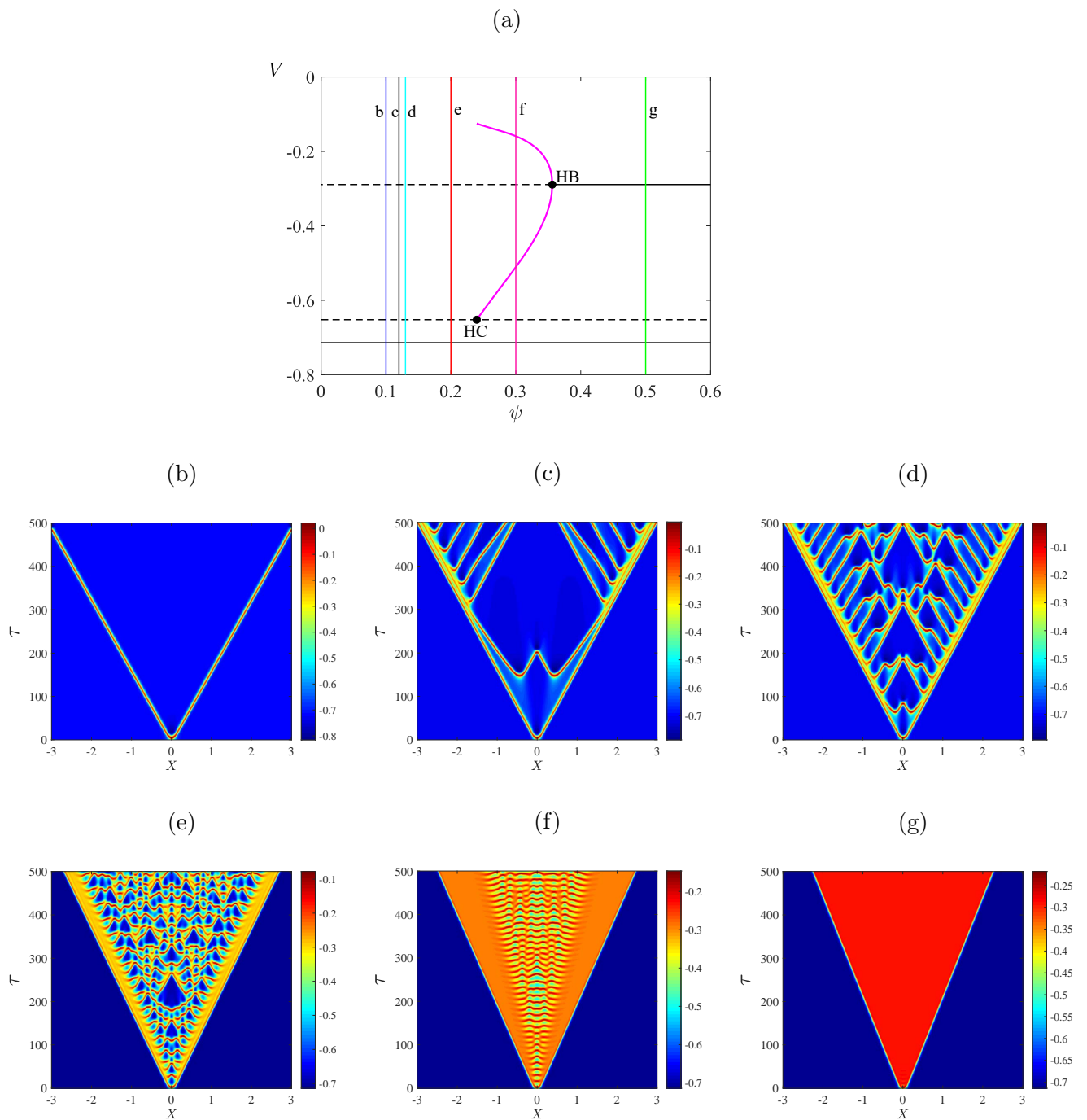


Figure 4.5: Space-time plots of the membrane potential  $V$ . (b)–(g):  $\psi = 0.1, 0.12, 0.13, 0.2, 0.3,$  and  $0.5$ , respectively. Other parameters are fixed as in Table 2.2. The solution transitions from propagating pulses travelling in opposite direction to complex spatiotemporal patterns to fronts travelling in opposite direction.

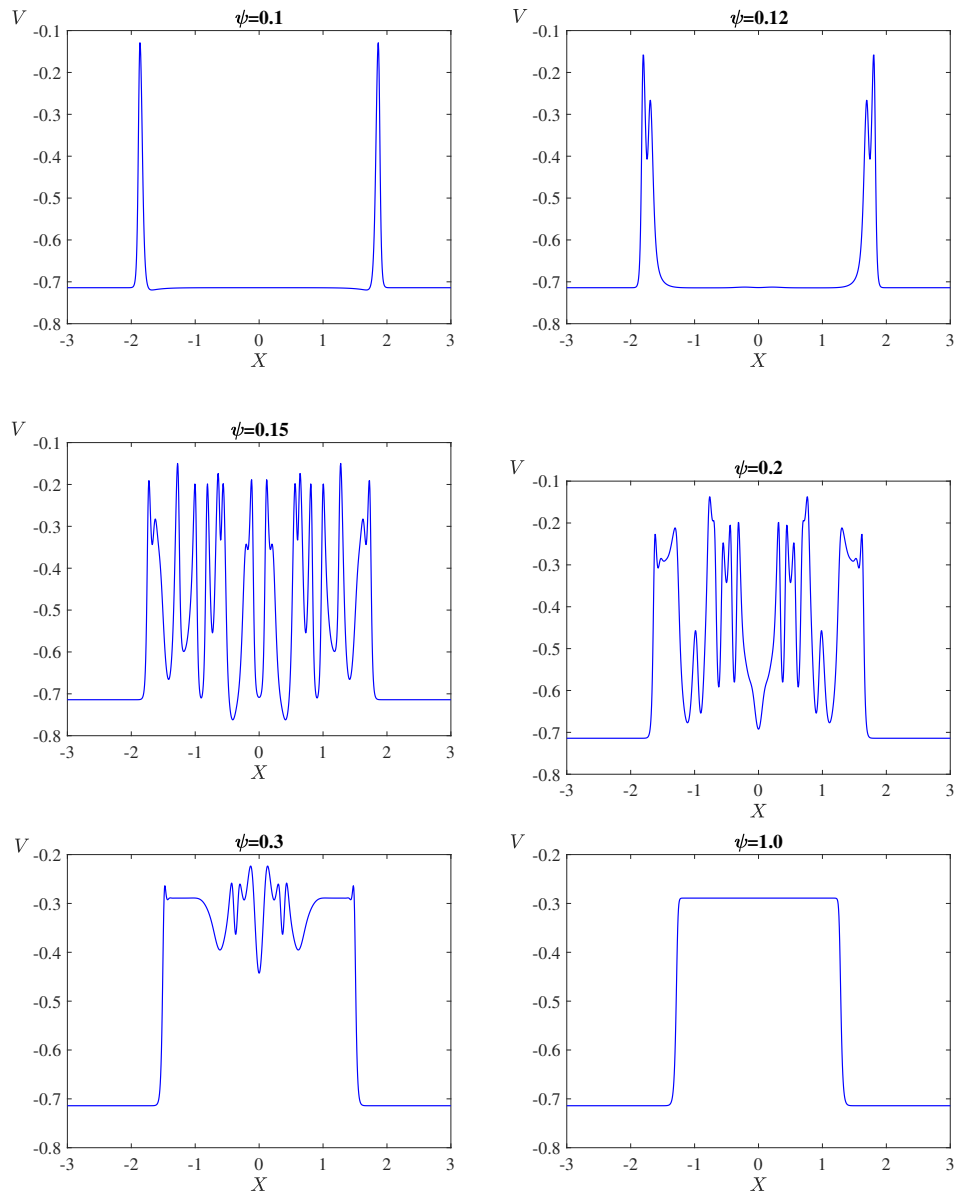


Figure 4.6: Solution profiles at time  $\tau = 300$  showing the transitions from travelling pulses to spatiotemporal chaos and to fronts.



in Fig. 3.1c. For values of  $\bar{v}_1$  to the left of the first saddle-node bifurcation  $SN_1$ , the system goes back quickly to the homogeneous steady state after initial perturbation.

It is seen that the emergent spatiotemporal patterns seem similar to what we observed in Sec. 4.3.1 for the parameter values of  $\bar{v}_1$  considered except for Fig. 4.7c at where the solution looks like travelling pulses for transient time. The spatiotemporal structure for longer simulation time at  $\bar{v}_1 = -0.255$  is shown in Fig. 4.8 and it is observed that the solution behaviour is similar to Fig. 4.2d in long time.

Similarly, the dynamical behaviour of the model varying  $\psi$  with a straight line as the initial perturbation is the same with the Gaussian stimulus in Sec. 4.3.3. In particular, the spatiotemporal pattern for  $\psi = 0.12$  is shown in Fig. 4.9, the result is similar to Fig. 4.5c. The results in this section shows that the profile of the initial perturbation does not seem to change the types of spatiotemporal patterns observed in the model.

### 4.3.5 Simulations with Two-Point Source

In this section we explore the spatiotemporal dynamics of (2.2.6)–(2.2.7) by perturbing the homogeneous steady state at two spatial locations with same initial profile. Here, we consider two Gaussian initial stimuli centred at  $X = \pm 1$ . The results of a simulation for  $\tau = 500$  varying  $\bar{v}_1$  are shown in Fig. 4.10. The perturbation creates a pulse at points of stimulation while other regions remain at the homogeneous steady state across the domain. The spatiotemporal patterns observed do not seem qualitatively different from those produced in the case of single point source perturbation (Fig. 4.2).

For extreme low values of  $\bar{v}_1$ , the system stabilises at the homogeneous steady state after a short time of periodic oscillations. A typical example is shown in Figs. 4.10a. In some parameter regimes, the pulse created at the perturbed points splits into two pulses propagating in opposite directions with irregular spatiotemporal patterns between the pulses. As time progresses, the right propagating pulse and left propagating

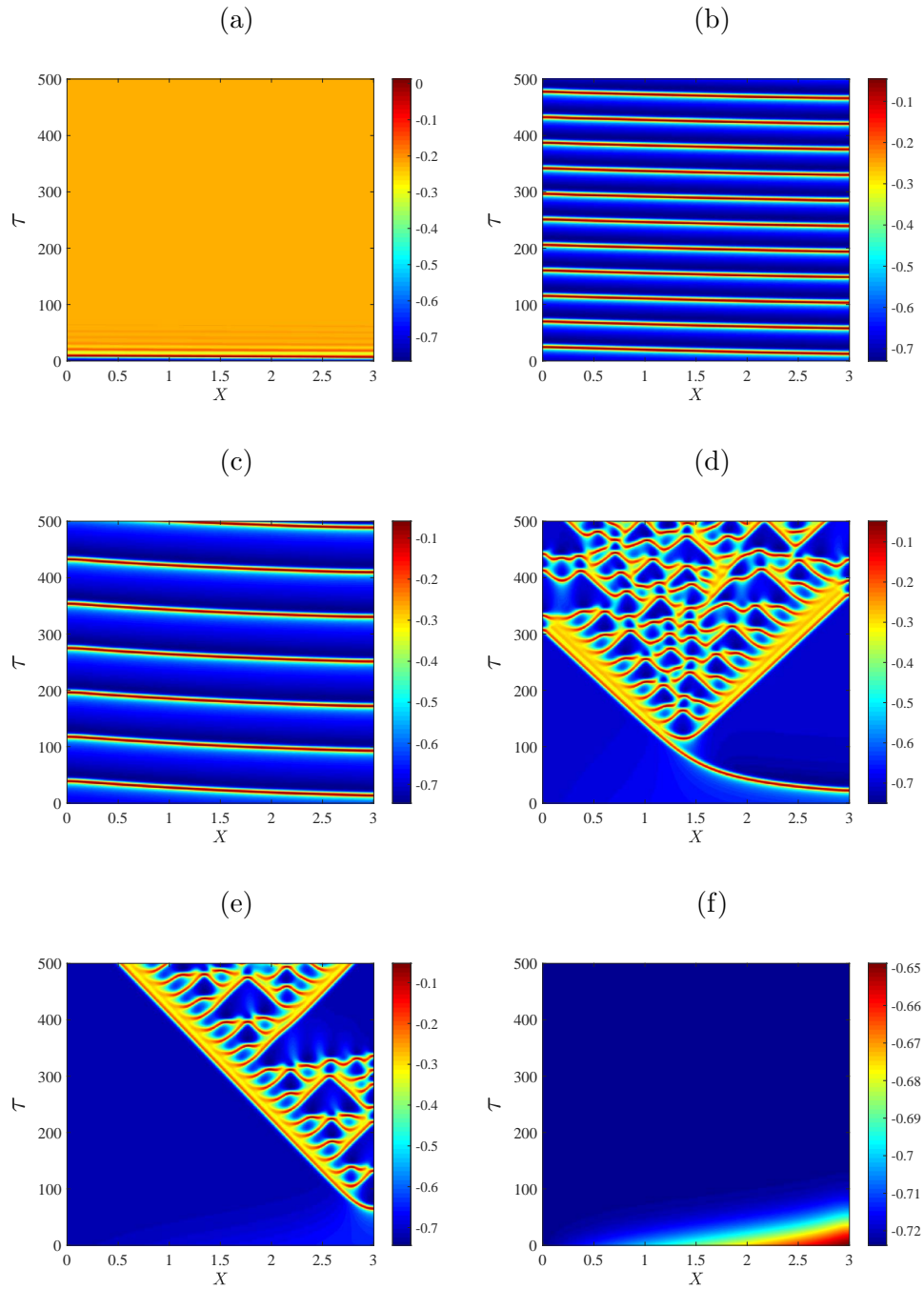


Figure 4.7: Space-time plots of the membrane potential  $V$ . (a)–(f):  $\bar{v}_1 = -0.325, -0.265, -0.25, -0.248, -0.246, \text{ and } -0.245$ , respectively. Other parameters are fixed as in Table 2.2 and  $\epsilon = 0.025$ .

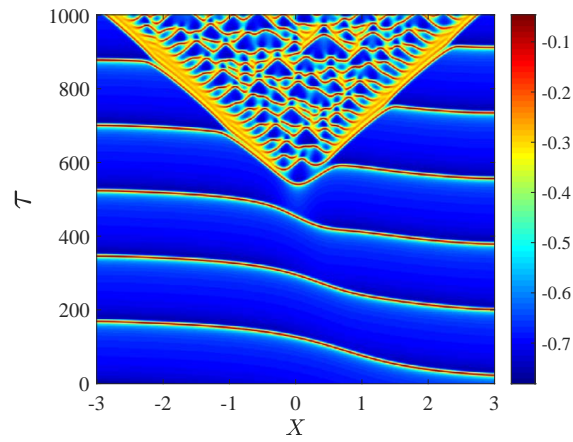


Figure 4.8: Space-time plot of the membrane potential  $V$  at  $\bar{v}_1 = -0.255$  with a straight line as the initial perturbation.

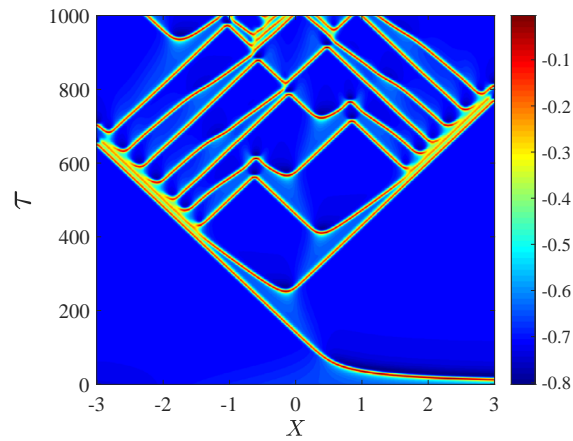


Figure 4.9: Space-time plot of the membrane potential  $V$  for simulation time  $\tau = 1000$  at  $\psi = 0.12$  with a straight line as the initial perturbation.

pulse from the two point sources coincide at the centre of the domain to create more irregular patterns across the domain, see Figs. 4.10 (b)–(e). Finally, for extremely high values of  $\bar{v}_1$  the system goes to back quickly to the homogeneous steady state after perturbation. This behaviour is shown in Fig. 4.10f. Similar analysis is carried out for  $\psi$ , the spatiotemporal patterns observed seem to appear similar to those for a one-point source for the same values of  $\psi$  in Fig. 4.5.

The effect of the distance between the point sources, say  $\rho_{\text{diff}}$ , on the behaviour of solutions is also considered. It is observed that the spatial locations of the point sources do not affect the mechanisms and kind of patterns in the system except that the waves coincide in short time if the point sources are close to each other while it takes longer time for the collision of waves to occur for larger distance. Fig. 4.12 shows the simulations with the same parameter value of  $\psi$  with two point sources at different spatial locations. In Fig. 4.12a the distance between the point sources  $\rho_{\text{diff}} = 2$ , the waves collide at time  $\tau = 176$  while in Fig. 4.12b  $\rho_{\text{diff}} = 4$ , the waves collide at time  $\tau = 368$ .

## 4.4 Discussion

We have studied in detail the spatiotemporal dynamics in a model of SMCs coupled electrically through the gap junctions. We began our analysis by establishing by linear stability analysis that the spatiotemporal patterns observed in the model are not due to Turing instability but as a consequence of the nonlinear dynamics of the system in the absence of diffusion, plus the coupling effect of diffusion. We explained many qualitative features of the spatiotemporal dynamics by referring to the bifurcation analysis of the system in the absence of diffusion that was given in the preceding chapter.

To investigate the evolution of the model dynamics as time increases we perturbed

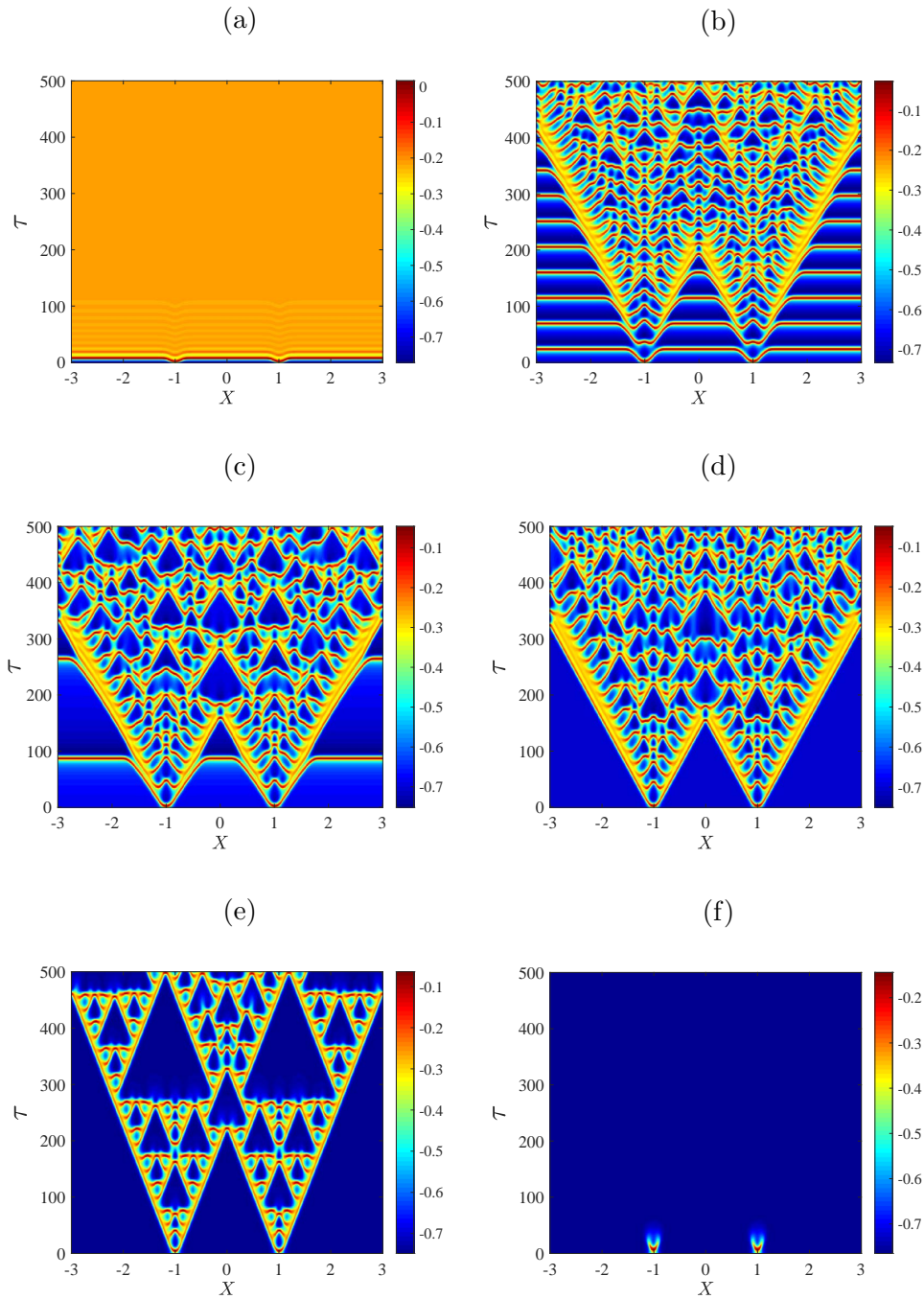


Figure 4.10: Space-time plots of the membrane potential  $V$  with two Gaussian pulses centered at  $X = \pm 1$ , respectively. (a)–(f):  $\bar{v}_1 = -0.325, -0.265, -0.250, -0.248, -0.240$ , and  $-0.230$ , respectively. Other parameters are fixed as in Table 2.2.

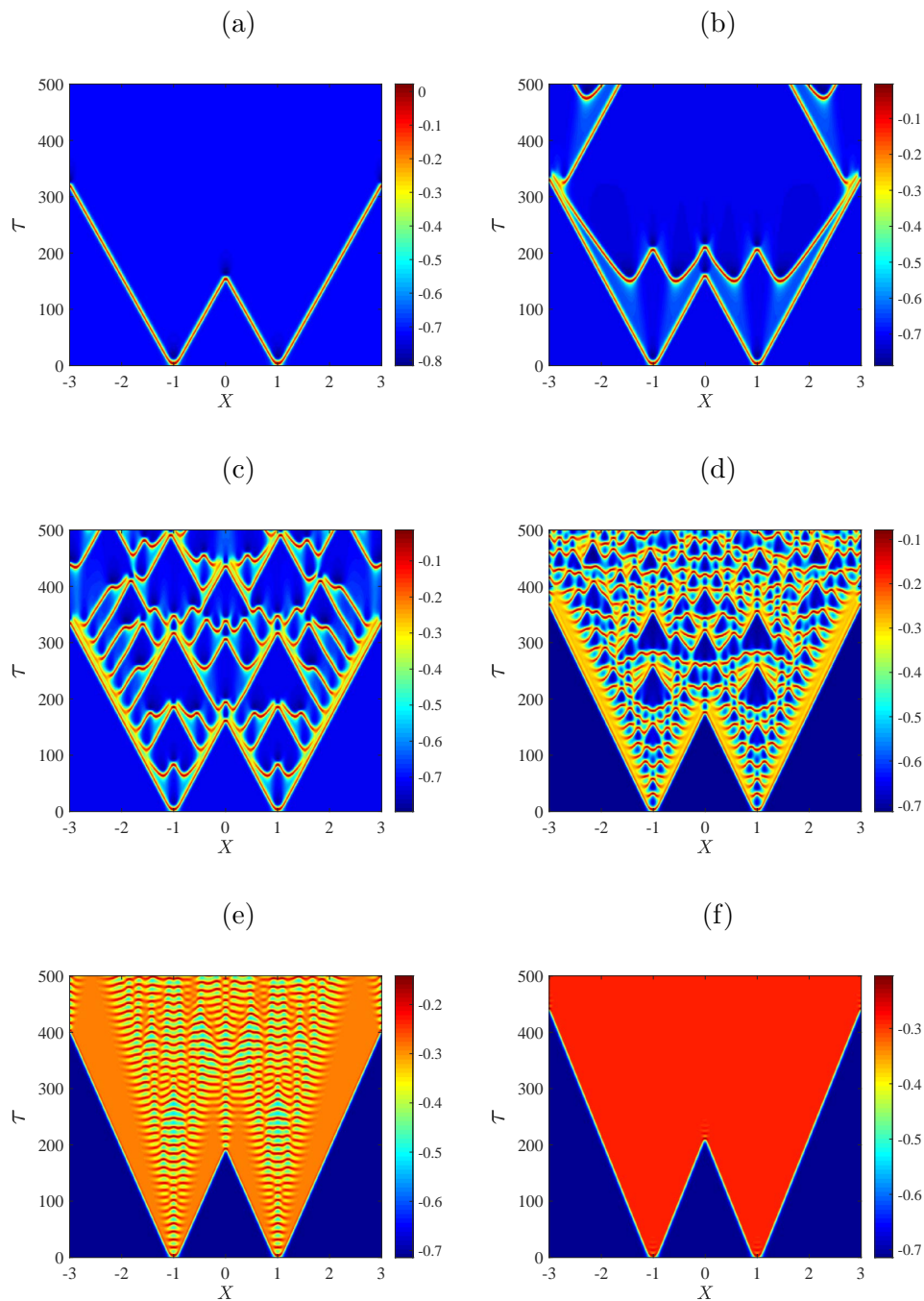


Figure 4.11: Space-time plots of the membrane potential  $V$  for simulation time  $\tau = 500$  with two Gaussian pulses centred at  $X = \pm 1$ , respectively. (a)–(f):  $\psi = 0.1, 0.12, 0.13, 0.2, 0.3,$  and  $0.5$ , respectively. Other parameters are fixed as in Table 2.2. The solution transitions from propagating pulses travelling in opposite direction to complex spatiotemporal patterns to fronts travelling in opposite direction.

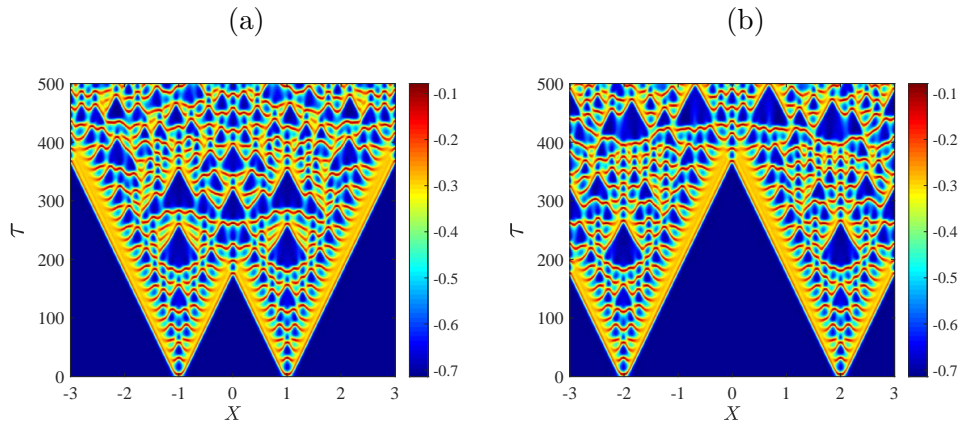


Figure 4.12: Space-time plots of the membrane potential  $V$  for simulation time  $\tau = 500$  at  $\psi = 0.2$  with two Gaussian pulses centered at (a)  $X = \pm 1$  with distance between the point sources  $\rho_{\text{diff}} = 2$ ; (b)  $X = \pm 2$  with distance between the point sources  $\rho_{\text{diff}} = 4$ .

the centre of the domain with a Gaussian pulse. In general, the initial perturbation induced counter propagating pulses that travel across the domain as time progresses. By varying  $\bar{v}_1$  we found some interesting patterns that depend on the parameter values. For values of  $\bar{v}_1$  close to the left of the Hopf bifurcation the system returns to the steady state quickly after short time-periodic oscillations. For values  $\bar{v}_1$  to right of the Hopf bifurcation, irregular triangular patterns are generated. This is due to the destabilisation of the pulse initiated by the Gaussian stimulus. For values of  $\bar{v}_1$  below and above the saddle-node  $\text{SN}_2$ , spatiotemporal chaos is observed behind two travelling pulses moving in opposite directions. The resulting patterns found in our numerical simulations are similar to the one found in (Merkin et al., 1996; Hartle and Wackerbauer, 2017).

We further explored spatiotemporal dynamics by varying  $\psi$ . For low values there exist two stable counter propagating pulses initiated at center of the domain that travel through the entire domain as time progresses. For intermediate values, secondary pulses are produced behind primary pulses which further collide to create irregular triangular patterns. Increasing  $\psi$ , to the right of the Hopf bifurcation the pattern transitions to two travelling fronts moving in opposite directions.

Finally, we investigated the effect of the profile of the initial perturbation on the spatiotemporal dynamics of the model. The patterns observed when the initial perturbation is changed to a straight line are similar to when a Gaussian pulse is considered as the perturbation function. Therefore, we can conclude that the shape of initial perturbation does not appear to have much effect on the type of spatiotemporal patterns exhibited by the model provided an action potential is triggered by the initial perturbation.



# 5. Travelling Wave Analysis of the Reaction-Diffusion System

Travelling waves play a vital role in understanding many biological, physical, and chemical systems, such as the propagation of signals in neurons (Hodgkin and Huxley, 1952), beams and pulses that travel through an optical fiber, solitary water waves in a channel, flame fronts in chemical reactions, and synchronisation of cell cycles and cell migration (Chang and Ferrell Jr., 2013; Yang et al., 2016). Travelling waves of electrical activities in excitable cells are due to interactions between the cells. Emergence of complex dynamics of such waves can sometimes cause tissue or cellular disorders, for example, multiple propagation of fibrillation waves observed during heart contractions (Moe et al., 1964; Pandit and Jalife, 2013).

In the previous chapter, we showed that the reaction-diffusion system (2.2.6)–(2.2.7) exhibits different forms of travelling waves including propagating pulses and fronts depending on model parameters. In this chapter, we will be concerned with the analysis of travelling wave solutions for a range of parameter values where travelling waves have been observed in our numerical simulations, to establish existence of the wave and numerically approximate the wave speed. Also, we will investigate the stability of the travelling wave as a solution of (2.2.6)–(2.2.7).

## 5.1 Existence of Travelling Waves via Wave Speed Analysis

Travelling waves (TWs) are solutions to a partial differential equation on an infinite domain which propagate with a fixed shape, and speed. To describe the TW profile we

consider TWs with speed  $c > 0$ . Introducing the travelling wave variable,  $\zeta = X - c\tau$ , we now treat  $V$  and  $N$  as a function of  $\zeta$  and  $\tau$ . Equations (2.2.6)–(2.2.7) transform to

$$\begin{pmatrix} V \\ N \end{pmatrix}_\tau = D \begin{pmatrix} V \\ 0 \end{pmatrix}_{\zeta\zeta} + c \begin{pmatrix} V \\ N \end{pmatrix}_\zeta + \begin{pmatrix} f(V, N) \\ g(V, N) \end{pmatrix}, \quad (5.1.1)$$

where

$$\begin{aligned} f(V, N) &= -\bar{g}_L(V - \bar{v}_L) - \bar{g}_K N(V - \bar{v}_K) - \bar{g}_{Ca} M_\infty(V)(V - \bar{v}_{Ca}), \\ g(V, N) &= \lambda_N(V)(N_\infty(V) - N). \end{aligned}$$

TWs are solutions to (5.1.1) that propagate without changing their profile at a constant speed  $c$ . That is, TWs are stationary solutions to (5.1.1). These solutions satisfy

$$\begin{pmatrix} V \\ N \end{pmatrix}_\tau = \mathbf{0},$$

and hence, by (5.1.1), they satisfy the ordinary differential equation (ODE)

$$D \begin{pmatrix} V \\ 0 \end{pmatrix}_{\zeta\zeta} + c \begin{pmatrix} V \\ N \end{pmatrix}_\zeta + \begin{pmatrix} f(V, N) \\ g(V, N) \end{pmatrix} = \mathbf{0}. \quad (5.1.2)$$

Equation (5.1.2) defines the spatial profile of the TW solution denoted by

$$P(\zeta) = \begin{pmatrix} V(\zeta) \\ N(\zeta) \end{pmatrix}. \quad (5.1.3)$$

We rewrite (5.1.2) as system of first order ODEs with  $' := \frac{d}{d\zeta}$ ; introducing a new

variable  $W = V'$  to obtain

$$\begin{aligned} V' &= W, \\ W' &= -\frac{1}{D}(cW + f(V, N)), \\ N' &= -\frac{1}{c}g(V, N), \end{aligned} \tag{5.1.4}$$

with boundary conditions:

$$\lim_{\zeta \rightarrow +\infty} (V, W, N)(\zeta) = (V_+, 0, N_+), \quad \lim_{\zeta \rightarrow -\infty} (V, W, N)(\zeta) = (V_-, 0, N_-), \tag{5.1.5}$$

where  $V_{\pm}$  and  $N_{\pm}$  are boundary values (or asymptotic states). We will refer to (5.1.4) as the travelling wave ordinary differential equation (TWODE) system. The dependence of terms on the right hand-sides of the TWODE system on  $c$  is significant in obtaining the existence of TW solutions. Types of TWs commonly observed in excitable systems are fronts, solitary pulses, and periodic wave trains. These are described below and shown in Fig. 5.1.

**Front:** A travelling front tends to a constant as both  $\zeta \rightarrow -\infty$  and  $\zeta \rightarrow \infty$ . It connects two different asymptotic states, thus in the phase space of the TWODE system the corresponding trajectory that connects the two states is a *heteroclinic orbit*.

**Pulse:** A travelling pulse is the same as a travelling front except the two asymptotic states are the same. This TW is represented by a *homoclinic orbit* since the corresponding trajectory connects one equilibrium to itself.

**Periodic wave trains:** Periodic wave trains are TW solutions that are periodic in  $\zeta$ . Such TWs do not satisfy the constant boundary conditions (5.1.5). They are represented by limit cycles in the phase space of the TWODE system.

**Homogeneous waves:** These are simply constant solutions and correspond to equilibria of the TWODE system.

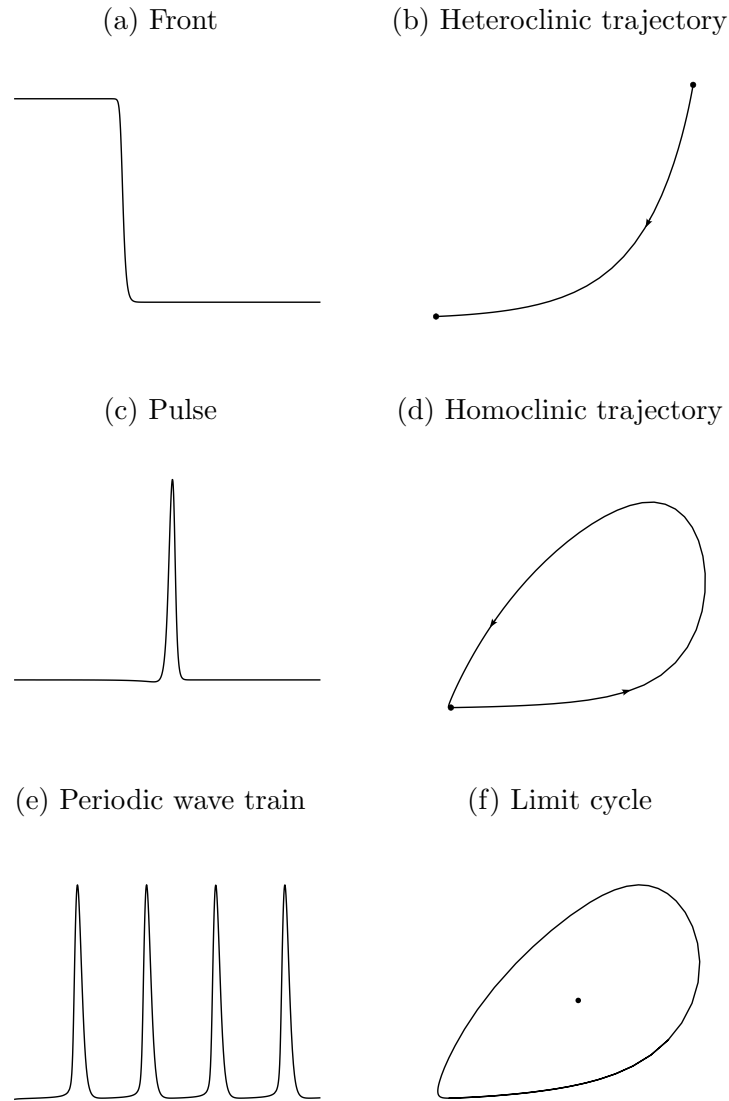


Figure 5.1: A schematic diagram showing three different types of travelling waves and their corresponding trajectories in the phase space of the TWODE system. The black dots correspond to equilibria.

For some values of the parameter  $\psi$ , direct simulations of (2.2.6)–(2.2.7) result in travelling pulses and fronts, respectively. For example, when  $\psi = 0.1$  two stable counter-propagating pulses are created, and they travel across the domain at approximate speed  $c = 0.006182$  (see Fig. 4.5b). Also, when  $\psi = 0.5$  two stable counter-propagating fronts are created, and they travel across the domain at speed  $c = 0.004155$  (see Fig. 4.5g). These speeds have been estimated directly from the numerical simulation results. Now, we want to establish the existence of TW solutions for (2.2.6)–(2.2.7). That is, we want to find the homoclinic and heteroclinic trajectories of (5.1.4) that correspond to such TW solutions. A number of mathematical methods have been established to describe the existence of TW solutions in a reaction-diffusion system, for example, the shooting method (Ermentrout, 2002), singular perturbation theory (Merkin and Sadiq, 1996; Cornwell and Jones, 2018), variational techniques (Chen and Choi, 2015), and the factorisation method (Achouri, 2016).

We use the shooting method to numerically investigate the existence of TWs and to approximate their wave speed. The simulation procedure for the shooting method is the following: Given an  $n$ -dimensional system of ODEs, we can compute an equilibrium, and evaluate its associated eigenvalues. If none of the eigenvalues lie on the imaginary axis, then there are  $m$  eigenvalues with positive real parts and  $n - m$  eigenvalues with negative real parts. Since the equilibrium is hyperbolic, by the stable manifold theorem there exist unstable and stable invariant manifolds,  $\Lambda^\pm$ , which are of  $m$  and  $n - m$  dimensions respectively. Every point on  $\Lambda^+$  tends to the equilibrium as  $\zeta \rightarrow -\infty$ , and every point on  $\Lambda^-$  tends to the equilibrium as  $\zeta \rightarrow \infty$ .

The simulation of the TWODE system (5.1.4) was carried out in MATLAB. We first numerically computed equilibria and their associated Jacobian matrices. The desired homoclinic or heteroclinic trajectory was found by using, as an initial point, a point perturbed from the corresponding equilibrium in a direction given by one of the eigenvectors of its Jacobian matrix. We solved (5.1.4) from this initial point (this is ‘shoot-

ing’) and adjusted the value of  $c$  until the solution was approximately homoclinic (or heteroclinic).

Specifically in case of the pulse, the solution travels away from the bottom steady state to the top steady state and returns to the bottom steady state in the ODE system, see Fig. 4.5b. Thus, we look for a trajectory that approaches the asymptotic state  $(V, W, N) = (-0.7148, 0, 0.001764)$  as  $\zeta \rightarrow \pm\infty$ . The Jacobian matrix evaluated at  $(V, W, N)$  has one positive eigenvalue and two negative eigenvalues for all  $c > 0$ . Thus, there is a one-dimensional stable manifold and a two-dimensional unstable manifold. We shoot from the bottom steady state along the one-dimensional manifold and vary  $c > 0$  until desired homoclinic trajectory is obtained. The wave speed we obtained by shooting is  $c = 0.006116$ . This is very similar to the wave speed of the pulse solution that we estimated from the simulation of (2.2.6)–(2.2.7) at  $\psi = 0.1$ . The plot of the pulse profile for  $V$  is shown in Fig. 5.2a and its corresponding homoclinic trajectory in  $(V, W, N)$  phase space is shown in Fig. 5.2b.

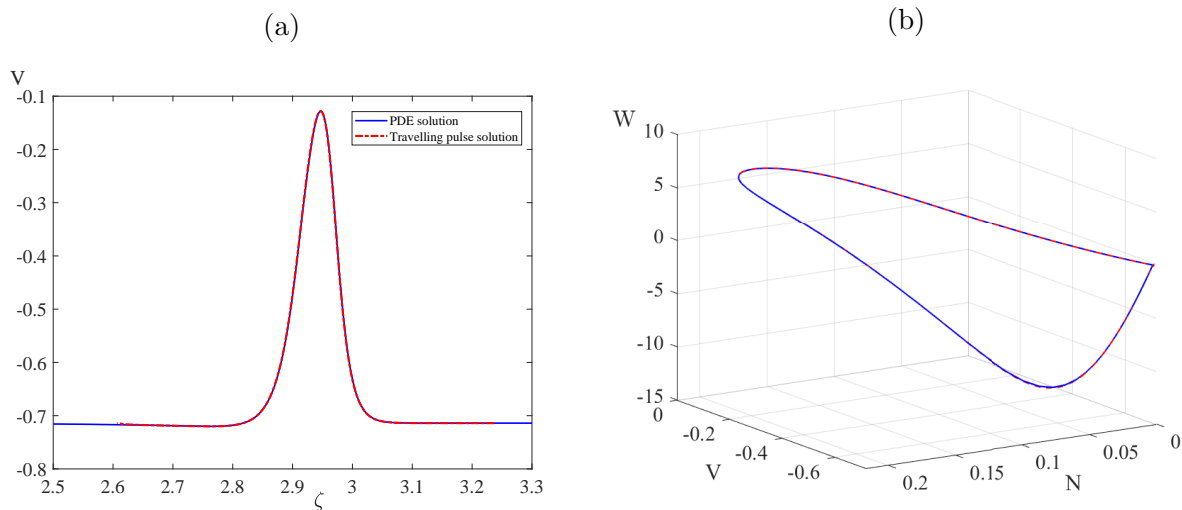


Figure 5.2: (a) The solution profile of (2.2.6)–(2.2.7) and the travelling pulse  $V(\zeta)$  with  $c = 0.006116$  (b) Corresponding homoclinic trajectory representing the pulse in (a) connecting the asymptotic state  $(V, W, N) = (-0.7148, 0, 0.001764)$  to itself in the  $(V, W, N)$  phase space. The parameters are  $\psi = 0.1$ ,  $D = 0.0001$ ,  $c = 0.006116$ .

From Fig. 4.5g, we can see that the travelling front connects the top and bottom steady states of the ODE system. We followed a similar procedure to find the heteroclinic trajectory that connects the asymptotic state  $\mu_2(V, W, N) = (-0.2935, 0, 0.1559)$  to  $\mu_1 = (V, W, N) = (-0.7148, 0, 0.001764)$  as  $\zeta \rightarrow \pm\infty$ .

From Fig. 4.5g, we can see that the travelling front connects the top and bottom steady states of the ODE system. We followed a similar procedure to find the heteroclinic trajectory that connects the asymptotic state  $(V, W, N)_- = (-0.2935, 0, 0.1559)$  to  $(V, W, N)_+ = (-0.7148, 0, 0.001764)$  as  $\zeta \rightarrow \pm\infty$ . The eigenvalues of the Jacobian matrix  $J$  evaluated at  $(V, W, N)_-$  and  $(V, W, N)_+$  has one stable and two unstable eigenvalues. Thus, there is a one-dimensional stable manifold and a two-dimensional unstable manifold. We shoot from the one-dimensional manifold of the top steady state to approximate the heteroclinic by varying  $c$  until the desired trajectory is obtained. The wave speed obtained by shooting was  $c = 0.0043$  which is close to the wave speed estimated from the simulation of (2.2.6)–(2.2.7) at  $\psi = 0.5$ . The plot of the front profile for  $V(\zeta)$  is shown in Fig. 5.3a and its corresponding heteroclinic trajectory in  $(V, W, N)$  phase space is shown in Fig. 5.3b.

## 5.2 Stability Analysis of Travelling Waves

Now that TWs to (2.2.6)–(2.2.7) have been found, we now address their stability. Stable propagating solutions can lose stability as model parameters are varied. A typical example is shown in Fig. 4.5. A stability analysis of TW solutions thus provides a more detailed understanding of the wave dynamics of the reaction-diffusion system.

Note that any translate  $P(\zeta + \alpha)$  of the wave  $P(\zeta)$ , with  $\alpha \in \mathbb{R}$  fixed, is also a TW. Here we are concerned with the stability of a given TW, i.e. we are interested in solutions whose initial conditions are small perturbations of the TW under consideration. If every such solution stays close to the set of all translates of  $P(\zeta)$  for all positive

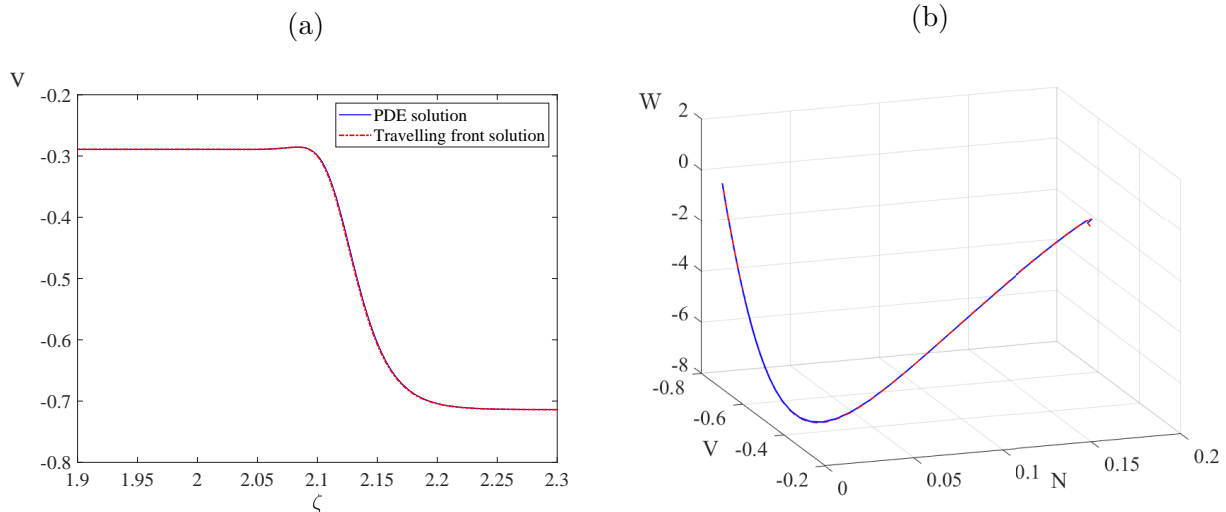


Figure 5.3: (a) The solution profile of (2.2.6)–(2.2.7) and travelling front  $V(\zeta)$  with  $c = 0.006116$  (b) Corresponding heteroclinic trajectory representing the front in (a) connecting the asymptotic state  $(V, W, N) = (-0.2935, 0, 0.1559)$  to  $(V, W, N) = (-0.7148, 0, 0.001764)$  in the  $(V, W, N)$  phase space. The parameters are  $\psi = 0.1$ ,  $D = 0.0001$ ,  $c = 0.006116$ .

times, and converges to a translate of  $P(\zeta)$  as  $\zeta \rightarrow \infty$  then we say that  $P(\zeta)$  is asymptotically stable. If there are initial conditions arbitrarily close to the wave such that the associated solutions leave a small neighbourhood of the wave and its translates, then the wave is unstable (Sandstede, 2002).

Different techniques have been used to investigate the stability the TWs, for example, the shooting method (Ledoux et al., 2010), Hill’s method (Deconinck and Nathan, 2006), pseudospectra method (Trefethen and Embree, 2005). The major approach in investigating the stability of a TW is the use of a linearisation criterion. This can be achieved by linearising the PDE about the TW solution. The spectrum of the resulting linear operator  $\mathcal{L}$  provides information on the stability of the TW. If the spectrum is entirely contained in the left half of the complex plane, then the TW is stable. If part of the spectrum belongs to the right half of the complex plane, it is unstable (Jones, 1984; Eigentler and Sherratt, 2020).

A numerical continuation method for the computation of spectra of the linear opera-



tor  $\mathcal{L}$  was introduced by Sandstede (2002) and its implementation using the software package AUTO was presented by Rademacher et al. (2007). A comprehensive analysis of various aspects and concepts related to stability analysis of TW solutions using this method is given by Kapitula and Promislow (2013). In the next section we provide the setup required for the computation of the spectrum of the linear operator in a general  $m$ -dimensional setting.

### 5.2.1 Spectral Analysis

Let  $D$  be a diagonal  $m \times m$  matrix of diffusion coefficients with positive entries and  $G(U) : \mathbb{R}^m \rightarrow \mathbb{R}^m$  be a smooth function. We consider the reaction-diffusion system in one spatial dimension given by

$$U_\tau = DU_{xx} + G(U), \quad x \in \mathbb{R}, \quad \tau \geq 0, \quad U \in \mathbb{R}^m. \quad (5.2.1)$$

We consider solutions to (5.2.1) of the form  $U(x - c\tau, \tau)$  such that in a moving coordinate frame in the variable  $\zeta = x - c\tau$  with speed  $c > 0$  we get

$$U_\tau = DU_{\zeta\zeta} + cU_\zeta + G(U). \quad (5.2.2)$$

A travelling wave  $U(\zeta, \tau) = P(\zeta)$  is a stationary solution to (5.2.2), thus

$$DP_{\zeta\zeta}(\zeta) + cP_\zeta(\zeta) + G(P(\zeta)) = 0. \quad (5.2.3)$$

Rewriting the second order ODE system (5.2.3) as a first order system gives

$$\begin{aligned} P_\zeta(\zeta) &= Q(\zeta), \\ Q_\zeta(\zeta) &= -\frac{1}{D} (cQ(\zeta) + G(P(\zeta))). \end{aligned} \quad (5.2.4)$$

Let  $\varepsilon\bar{P}(\zeta, t)$  for  $\varepsilon \ll 1$  be a small perturbation from the TW solution, i.e. write

$$P(\zeta, \tau) = P(\zeta) + \varepsilon\bar{P}(\zeta, \tau). \quad (5.2.5)$$

Substituting (5.2.5) into (5.2.2) and expanding  $G$  in a Taylor series about  $P(\zeta)$  gives

$$P(\zeta, \tau) = \mathcal{L}\bar{P} + \mathcal{O}(\varepsilon), \quad (5.2.6)$$

where  $\mathcal{L}$  is the linear operator

$$\mathcal{L} = D\partial_{\zeta\zeta} + c\partial_{\zeta} + \partial_U G(P(\zeta)). \quad (5.2.7)$$

The solution  $P(\zeta)$  is said to be spectrally stable if the spectrum of the linear operator, denoted by  $\Sigma(\mathcal{L})$  and defined below (see Definition 5.2.3), lies entirely in the left half of the complex plane. If any elements of  $\Sigma(\mathcal{L})$  have positive real part, then the corresponding travelling wave is spectrally unstable. By assuming the separation of variables

$$\bar{P}(\zeta, \tau) = e^{\lambda\tau}\Phi(\zeta), \quad (5.2.8)$$

we obtain the following eigenvalue problem:

$$\lambda\Phi = D\Phi_{\zeta\zeta} + c\Phi_{\zeta} + \partial_U G(P(\zeta))\Phi. \quad (5.2.9)$$

The eigenvalue problem (5.2.9) can be written as a first order ODE system

$$\mathcal{T}(\lambda)\Phi := \left( \frac{d}{d\zeta} - A(\zeta; \lambda) \right) \Phi = 0, \quad (5.2.10)$$

where  $\mathcal{T}$  is a first order linear operator. The matrix function  $A(\zeta; \lambda) \in \mathbb{C}^{2m \times 2m}$  can be

written as

$$A(\zeta; \lambda) = \tilde{A}(\zeta) + \lambda B(\zeta), \quad (5.2.11)$$

where

$$\tilde{A}(\zeta) = \begin{pmatrix} 0 & I \\ -\frac{1}{D}\partial_U G(P(\zeta)) & -\frac{c}{D} \end{pmatrix}, \quad B(\zeta) = \begin{pmatrix} 0 & 0 \\ -\frac{1}{D} & 0 \end{pmatrix}.$$

$A(\zeta; \lambda)$  is given by the asymptotic matrices  $A_{\pm}(\lambda)$  as  $\zeta \rightarrow \pm\infty$ .  $A_{\pm}(\lambda)$  is said to be hyperbolic if the real part of all eigenvalues of  $A_{\pm}(\lambda)$  is non-zero (i.e.  $\Sigma(A_{\pm}(\lambda)) \cap i\mathbb{R} \neq \emptyset$ ). The stable (unstable) subspaces associated with all eigenvalues with negative (positive) real part of the asymptotic matrices  $A_{\pm}(\lambda)$  are denoted as  $\mathbb{E}_{\pm}^s(\lambda)$  ( $\mathbb{E}_{\pm}^u(\lambda)$ ).

**5.2.1 Definition.** (Kapitula and Promislow, 2013) The Morse index of  $A_{\pm}(\lambda)$ , denoted by  $i(A_{\pm}(\lambda))$ , is the dimension of the unstable subspace associated to  $A_{\pm}(\lambda)$ :

$$i(A_{\pm}(\lambda)) := i_{\pm}(\lambda) = \dim(\mathbb{E}_{\pm}^u(\lambda)). \quad (5.2.12)$$

**5.2.2 Definition.** Let  $\text{Ker}(\mathcal{L})$  and  $\text{R}(\mathcal{L})$  denote the kernel and range of  $\mathcal{L}$ . We say that  $\mathcal{L}$  is a Fredholm operator if

- (a)  $\text{Ker}(\mathcal{L})$  is finite-dimensional,
- (b)  $\text{R}(\mathcal{L})$  is closed with finite codimension.

The Fredholm index of a Fredholm operator is defined as

$$\text{ind}(\mathcal{L}) = \dim[\text{Ker}(\mathcal{L})] - \text{codim}[\text{R}(\mathcal{L})].$$

We now define the spectrum of an operator.

**5.2.3 Definition.** (Sandstede, 2002) We say that  $\lambda \in \mathbb{C}$  is in the *spectrum*  $\Sigma$  of  $\mathcal{T}$  if  $\mathcal{T}(\lambda)$  is not invertible. We say that  $\lambda \in \Sigma$  is in the *point spectrum*  $\Sigma_{\text{pt}}$  of  $\mathcal{T}$  if  $\mathcal{T}(\lambda)$  is a *Fredholm operator* with index zero. We say that  $\lambda \in \Sigma$  is in the *essential spectrum*

$\Sigma_{\text{ess}}$  if it is not in the *point spectrum*, i.e.  $\Sigma \setminus \Sigma_{\text{pt}} := \Sigma_{\text{ess}}$ . The resolvent set of  $\mathcal{T}$  is defined as  $\rho = \mathbb{C} \setminus \Sigma$ .

Kapitula and Promislow (2013) showed that the essential spectrum can be characterised by the following set

$$\Sigma_{\text{ess}}(\mathcal{L}) = \{\lambda \in \mathbb{C} : i_-(\lambda) \neq i_+(\lambda)\} \cup \{\lambda \in \mathbb{C} : A_{\pm}(\lambda) \text{ is not hyperbolic}\}. \quad (5.2.13)$$

Next we come to spatial eigenvalues  $\mu$  which are given by solutions to the characteristic polynomial of  $A_{\pm}(\lambda)$ :

$$d_{\pm}(\lambda, \mu) := \det(A_{\pm}(\lambda) - \mu I) = 0. \quad (5.2.14)$$

Equation (5.2.14) is known as the dispersion relation for  $\mathcal{L}$  (or  $\mathcal{T}$ ). It can be obtained by substituting the ansatz  $\Phi(\zeta, \tau) = e^{\mu\zeta}\bar{\Phi}(\tau)$  into the eigenvalue problem (5.2.9). The borders of  $\Sigma_{\text{ess}}$  (also known as the Fredholm borders), denoted by  $\Sigma_{\text{F}}(\mathcal{L})$ , are then given by the following curves in the complex  $\lambda$ -plane (Kapitula and Promislow, 2013):

$$\Sigma_{\text{F}} := \{\lambda \in \mathbb{C} : d_{\pm}(\lambda, ik) = 0, k \in \mathbb{R}\}. \quad (5.2.15)$$

These curves correspond to the loss of hyperbolicity of  $A_{\pm}(\lambda)$ ; therefore, the essential spectrum depends solely on the behaviour of solutions at the asymptotic states as  $\zeta \rightarrow \pm\infty$ .

## 5.2.2 Spectra of Different Wave Types

Here we briefly discuss the consequences of the results from Sec. 5.2 for the different wave types observed in our system. For more details on this topic see (Sandstede, 2002; Rademacher et al., 2007; Kapitula and Promislow, 2013).

**Homogeneous waves:** Suppose  $P(\zeta)$  is a homogeneous stationary solution, so that  $P(\zeta) = P_0 \in \mathbb{R}^m$  does not depend on  $\zeta$ . In this case the coefficients of linearisation about  $P_0$  are constant and the linearised solution  $u$  satisfies an equation of the form

$$\frac{du}{d\zeta} = A_0(\lambda)u, \quad (5.2.16)$$

where  $A_0(\lambda)$  is a linearised matrix evaluated at  $P_0$ .

Equation (5.2.16) has a bounded solution on  $\mathbb{R}$  if, and only if, the matrix  $A_0(\lambda)$  is non-hyperbolic. A complex number  $\lambda$  is in the essential spectrum of  $\mathcal{T}$  if and only if

$$d_0(\lambda, k) := \det[A_0(\lambda) - (ik)I] = 0, \quad (5.2.17)$$

has a solution  $k \in \mathbb{R}$ . The essential spectrum consists of curves  $\lambda(k)$  in the complex plane, while the point spectrum of the homogeneous rest state is the empty set.

**Fronts:** Suppose that the TW solution  $P(\zeta)$  is a front such that the limits

$$\lim_{\zeta \rightarrow \pm\infty} P(\zeta) = P_{\pm} \in \mathbb{R}^m \quad (5.2.18)$$

exist and  $P_{\pm}$  are homogeneous stationary solutions (asymptotic steady states). The matrix  $A$  has limiting values

$$\lim_{\zeta \rightarrow \pm\infty} A(\zeta; \lambda) = A_{\pm}(\lambda). \quad (5.2.19)$$

Here  $\lambda$  is in the essential spectrum of  $\mathcal{T}$  if either  $\lambda$  is in essential spectrum of  $P_+$  or  $P_-$  or else if the Morse indices of  $A_{\pm}$  differ, i.e.  $i_+(\lambda) \neq i_-(\lambda)$ . Also  $\lambda$  is in the point spectrum of  $\mathcal{T}$  if and only if the asymptotic matrices  $A_{\pm}(\lambda)$  are both hyperbolic with identical Morse indices  $i_+(\lambda) = i_-(\lambda)$ .

**Pulses:** Suppose that the TW solution  $P(\zeta)$  is a pulse such that

$$\lim_{|\zeta| \rightarrow \infty} P(\zeta) = P_0 \in \mathbb{R}^m. \quad (5.2.20)$$

The matrix  $A$  has one limiting value

$$\lim_{|\zeta| \rightarrow \infty} A(\zeta; \lambda) = A_0(\lambda). \quad (5.2.21)$$

Here  $\lambda$  is in the essential spectrum if the asymptotic matrix  $A_0(\lambda)$  is not hyperbolic, i.e. if  $\lambda$  is in the essential spectrum of the asymptotic steady state  $P_0$ . Also  $\lambda$  is in the point spectrum if and only if  $A_0(\lambda)$  is hyperbolic. The major difference between this case and that of the front above is that the Morse indices at  $\zeta = -\infty$  and  $\zeta = +\infty$  are always the same.

### 5.2.3 Model Analysis

Having established the existence of travelling pulses and fronts in Sec. 5.1, we now investigate their stability. As mentioned above, the stability of the TW is determined by the spectrum  $\Sigma$  of the linear operator  $\mathcal{L}$  in (5.2.7), which for system (2.2.6)–(2.2.7) is

$$\mathcal{L} := \begin{pmatrix} D\partial_{\zeta\zeta} + c\partial_{\zeta} + f_V & f_N \\ g_V & c\partial_{\zeta} + g_N \end{pmatrix}. \quad (5.2.22)$$

Note that in (5.2.22)  $D$  is a scalar whereas in the previous section it was a  $m \times m$  matrix. For the separation of variables in (5.2.8) we write

$$e^{\lambda\tau}\Phi(\zeta, \tau) = e^{\lambda\tau}(\bar{p}(\zeta), \bar{q}(\zeta))^T. \quad (5.2.23)$$

Substituting (5.2.23) into (5.2.22) gives the eigenvalue problem  $(\mathcal{L} - \lambda I)\bar{\Phi} = 0$  which, in full, is given by

$$\lambda \begin{pmatrix} \bar{p} \\ \bar{q} \end{pmatrix} = \begin{pmatrix} D\partial_{\zeta\zeta} + c\partial_{\zeta} + f_V & f_N \\ g_V & c\partial_{\zeta} + g_N \end{pmatrix} \begin{pmatrix} \bar{p} \\ \bar{q} \end{pmatrix}. \quad (5.2.24)$$

We can rewrite (5.2.24) as the following system of first order ODEs

$$\begin{aligned} \bar{p}' &= \bar{r}, \\ \bar{r}' &= -\frac{c}{D}\bar{r} + \frac{1}{D}(\lambda - f_V)\bar{p} - \frac{1}{D}f_N\bar{q}, \\ \bar{q}' &= -\frac{1}{c}g_V\bar{p} + \frac{1}{c}(\lambda - g_N)\bar{q}, \end{aligned} \quad (5.2.25)$$

where  $' = \frac{d}{d\zeta}$ . The operator  $\mathcal{L} - \lambda I$  is equivalent to the operator  $\mathcal{T}(\lambda)$  given by

$$\mathcal{T}(\lambda) \begin{pmatrix} \bar{p} \\ \bar{r} \\ \bar{q} \end{pmatrix} := \left( \frac{d}{d\zeta} - A(\zeta; \lambda) \right) \begin{pmatrix} \bar{p} \\ \bar{r} \\ \bar{q} \end{pmatrix}, \quad (5.2.26)$$

where

$$A(\zeta; \lambda) = \begin{pmatrix} 0 & 1 & 0 \\ \frac{1}{D}(\lambda - f_V) & -\frac{c}{D} & -\frac{1}{D}f_N \\ -\frac{1}{c}g_V & 0 & \frac{1}{c}(\lambda - g_N) \end{pmatrix}. \quad (5.2.27)$$

Note that the dependence of  $A(\zeta; \lambda)$  on  $\zeta$  is through the underlying wave  $P(\zeta)$ ; thus, the matrix  $A(\zeta; \lambda)$  tends to asymptotic matrices  $A_{\pm}(\lambda)$  as  $\zeta \rightarrow \pm\infty$ . These limiting matrices are given by

$$A_{\pm}(\lambda) = \begin{pmatrix} 0 & 1 & 0 \\ \frac{1}{D}(\lambda - f_V(P_{\pm})) & -\frac{c}{D} & -\frac{1}{D}f_N(P_{\pm}) \\ -\frac{1}{c}g_V(P_{\pm}) & 0 & \frac{1}{c}(\lambda - g_N(P_{\pm})) \end{pmatrix}, \quad (5.2.28)$$

where

$$f_V(P_{\pm}) = \left[ -\bar{g}_L - \bar{g}_K N(P_{\pm}) - \frac{\bar{g}_{Ca}}{2\bar{v}_2} \left( 1 - \tanh^2 \left( \frac{V(P_{\pm}) - \bar{v}_1}{\bar{v}_2} \right) \right) (V(P_{\pm}) - \bar{v}_{Ca}) \right. \\ \left. - \frac{\bar{g}_{Ca}}{2} \left( 1 + \tanh \left( \frac{V(P_{\pm}) - \bar{v}_1}{\bar{v}_2} \right) \right) \right],$$

$$f_N(P_{\pm}) = -\bar{g}_K (V(P_{\pm}) - \bar{v}_K),$$

$$g_V(P_{\pm}) = \frac{\psi}{2\bar{v}_4} \left[ \left\{ \frac{1}{2} \left( 1 + \tanh \left( \frac{V(P_{\pm}) - \bar{v}_3}{\bar{v}_4} \right) \right) - N(P_{\pm}) \right\} \sinh \left( \frac{V(P_{\pm}) - \bar{v}_3}{2\bar{v}_4} \right) \right] \\ + \frac{\psi}{2\bar{v}_4} \left[ \cosh \left( \frac{V(P_{\pm}) - \bar{v}_3}{2\bar{v}_4} \right) \left( 1 - \tanh^2 \left( \frac{V(P_{\pm}) - \bar{v}_3}{\bar{v}_4} \right) \right) \right],$$

$$g_N(P_{\pm}) = -\psi \cosh \left( \frac{V(P_{\pm}) - \bar{v}_3}{2\bar{v}_4} \right).$$

For our system, from (5.2.14) and (5.2.28) we obtain the following cubic polynomial for the dispersion relation term

$$d_{\pm}(\lambda, \mu) = -\mu \left[ \left( -\frac{c}{D} - \mu \right) \left( \frac{\lambda - g_N}{c} - \mu \right) \right] - \left[ \left( \frac{\lambda - f_V}{D} \right) \left( \frac{\lambda - g_N}{c} - \mu \right) - \frac{f_N g_V}{cD} \right] \\ = -cD\mu^3 + [D(\lambda - g_N) - c^2]\mu^2 + [c(\lambda - g_N) + c(\lambda - f_V)]\mu \\ - [(\lambda - f_V)(\lambda - g_N) - f_N g_V] = 0. \quad (5.2.29)$$

Substituting  $\mu = ik$  for some  $k \in \mathbb{R}$  into (5.2.29) we obtain

$$d_{\pm}(\lambda, ik) = (-D(ik)^2 + ick + f_V - \lambda)(ick + g_N - \lambda) - f_N g_V = 0. \quad (5.2.30)$$

Solving  $d_{\pm}(\lambda, ik) = 0$  for  $\lambda$  gives

$$\lambda^2 - (-Dk^2 + 2cik + f_V + g_N)\lambda + ((k^2 D + ick + f_V)(ick + g_N) - f_N g_V) = 0. \quad (5.2.31)$$



For a particular wave number  $k$ , the solutions to (5.2.31) are

$$\lambda = \frac{\tau \pm \sqrt{\tau^2 - 4\delta}}{2}, \quad (5.2.32)$$

where

$$\tau = -k^2 D + ick + f_V + g_N, \quad (5.2.33)$$

$$\delta = (-k^2 D + ick + f_V)(ick + g_N) - f_N g_V. \quad (5.2.34)$$

We begin our analysis with spectral stability of homogeneous steady states. Following Sandstede (2002), it is sufficient to study the essential spectrum to determine the stability of the homogeneous steady state, as the point spectrum is always empty. The steady states of the reaction terms of (2.2.6)–(2.2.7) are spatially homogeneous steady state solutions in the reaction-diffusion system and the steady states to the TWODE system (5.1.4).

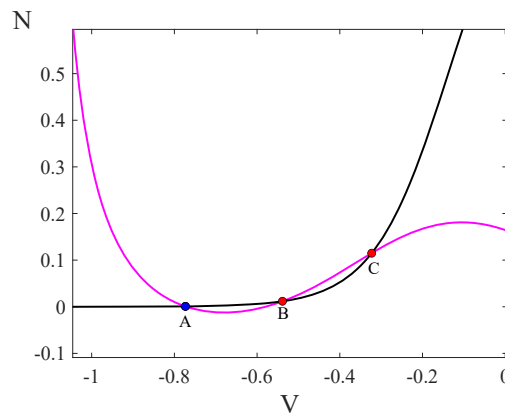


Figure 5.4:  $V$  and  $N$  nullclines for the nondimensionalised model (2.2.6)–(2.2.7) at  $\bar{v}_1 = -0.225$ . Magenta and black curves represent the  $V$ -nullcline, and  $N$ -nullcline, respectively. The blue and red filled circles are the steady states, A (stable), B and C (unstable). Other parameter values as in Table 2.2.

To calculate the essential spectrum of homogeneous steady state we will focus on values of  $\bar{v}_1$  between  $SN_1$  and  $SN_2$  where the system has three steady states. Fig. 5.4 shows

the nullclines of the state variables  $V$  and  $N$  at  $\bar{v}_1 = -0.225$ , the three intersections correspond to the steady states, A is stable node, B is a saddle point, and C is an unstable focus. The TWODE system (5.1.4) and the eigenvalues of its linearised system depend on the wave speed  $c$ . Thus for the range of values of  $c$  considered in this thesis, the steady states A, B and C are saddle points in the TWODE system.

To compute the essential spectra of the operator associated with homogeneous steady states A, B and C we use the characteristic polynomial (5.2.31) following (5.2.17). Our results are shown in Fig. 5.5. For steady state A, the curve of  $\lambda(k)$  lies entirely in the left-half plane of the complex plane (Fig. 5.5a), whereas, for steady states B and C the curves cross the imaginary axis (Fig. 5.5b and Fig. 5.5c). This indicates that A is spectrally stable, but B and C are spectrally unstable.

We found that the stability of the essential spectrum depends on the location of the steady state. For example, decreasing  $\bar{v}_1$  moves the  $V$ -nullcline up which results in the collision and annihilation of steady states A and B, and there is only one unstable steady state, C remaining. As  $\bar{v}_1$  decreases further, the system undergoes a subcritical Hopf bifurcation and the steady state C becomes stable after the bifurcation point. A typical example is shown Fig. 5.6a where the curve of  $\lambda(k)$  for  $C$  is contained in the left half plane, for the value of  $\bar{v}_1 = -0.45$ .

Next we compute the essential spectra of the travelling pulse and fronts. In our numerical simulations we observed travelling pulse at  $(\bar{v}_1, \psi) = (-0.2466, 0.1)$  with an estimated wave speed  $c = 0.006116$ , see Fig. 5.7a. It satisfies the following boundary conditions:

$$\lim_{|\zeta| \rightarrow \infty} (V, W, N)(\zeta) = (-0.7148, 0, 0.001764) = P_0, \quad (5.2.35)$$

which is an asymptotic state of (5.1.4). The essential spectrum is characterised by the stability properties of the asymptotic state  $P_0$  with the associated asymptotic matrix

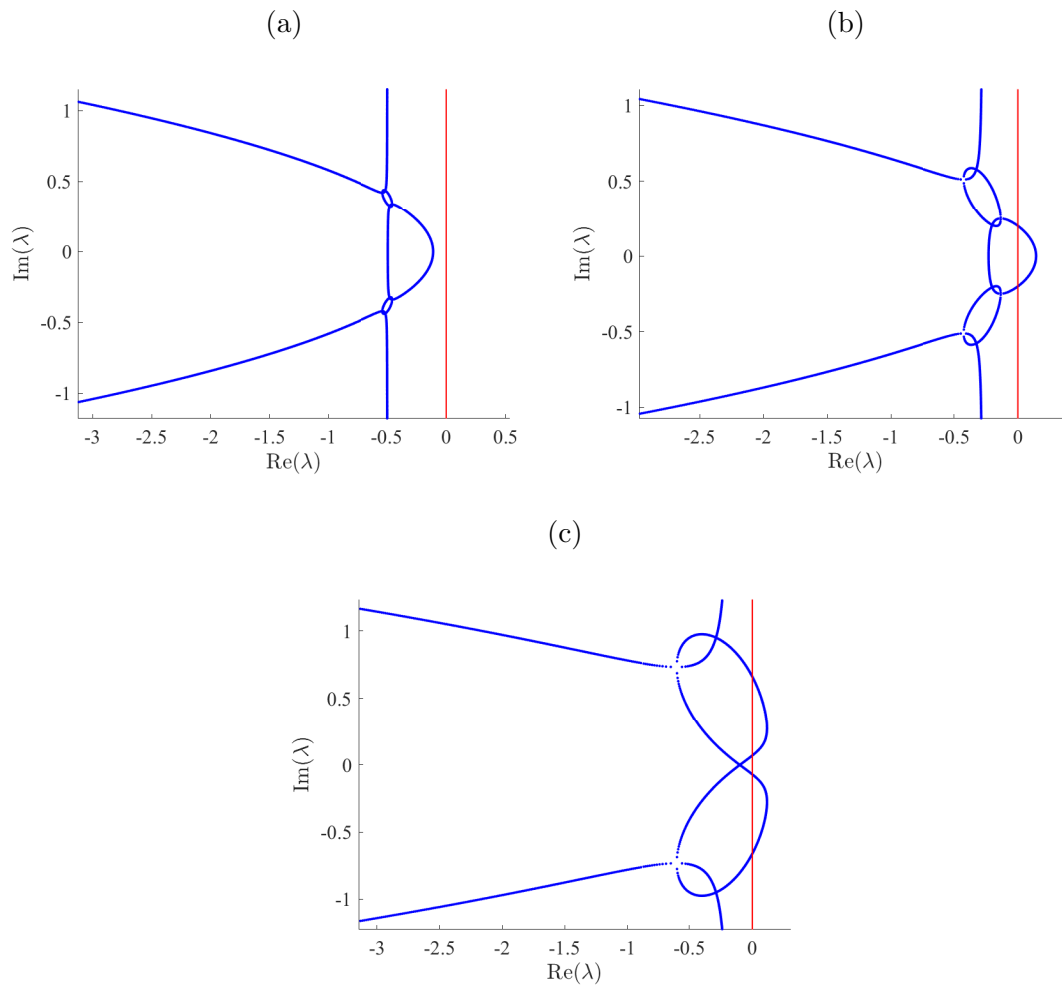


Figure 5.5: Essential spectra of steady states A, B, and C for  $\bar{v}_1 = -0.225$  with  $c = 0.006116$ .

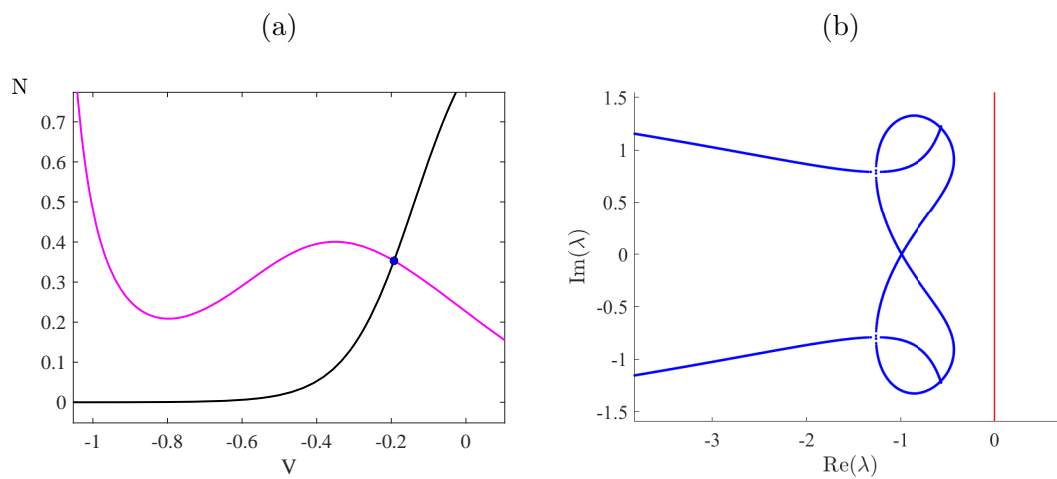


Figure 5.6: (a)–(b) Essential spectrum of steady state C for  $\bar{v}_1 = -0.45$  with  $c = 0.006116$ .

$A_0(\lambda)$  given by

$$A_0(\lambda) = \begin{pmatrix} 0 & 1 & 0 \\ \frac{1}{D}(\lambda + 0.0262) & -\frac{c}{D} & \frac{1}{D}(0.4109) \\ -\frac{1}{c}(0.0048) & 0 & \frac{1}{c}(\lambda + 0.2555) \end{pmatrix}, \quad (5.2.36)$$

$A_0(\lambda)$  is non-hyperbolic if at least one of its eigenvalues has zero real part. We then compute the essential spectrum using the dispersion relation (5.2.14). The curve of  $\lambda(k)$  in Fig. 5.7b lies entirely in the left half-plane in the complex plane, thus the spectral stability of the pulse is determined by the stability of its point spectrum.

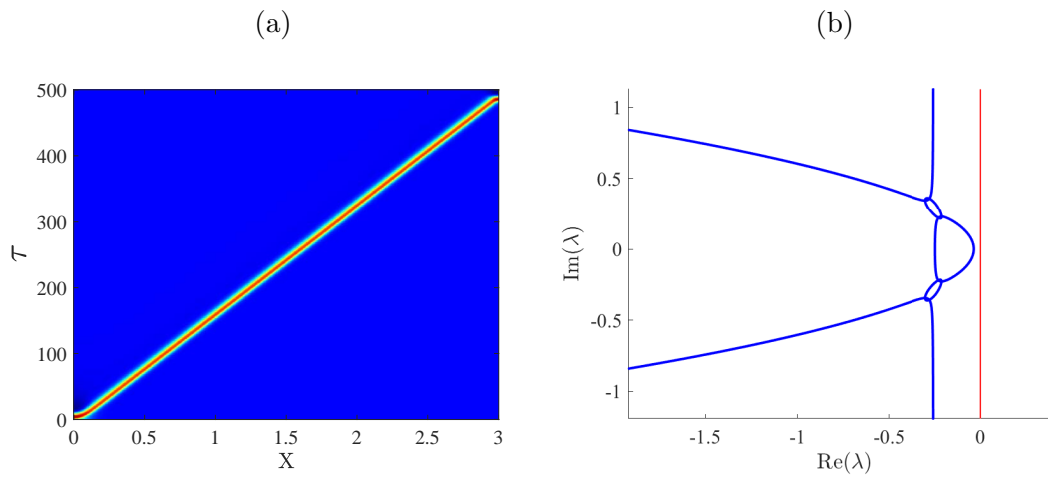


Figure 5.7: (a) A travelling pulse solution (b) The essential spectrum of the pulse with wave speed  $c = 0.006116$  and  $D = 0.0001$ .

A travelling front with an estimated wave speed  $c = 0.004368$  is observed at  $(\bar{v}_1, \psi) = (-0.2466, 5.0)$ , it satisfies the following boundary conditions:

$$\lim_{\zeta \rightarrow -\infty} (V, W, N)(\zeta) = (-0.2935, 0, 0.1559) = P_- \quad (5.2.37)$$

$$\lim_{\zeta \rightarrow +\infty} (V, W, N)(\zeta) = (-0.7148, 0, 0.001764) = P_+, \quad (5.2.38)$$

which are asymptotic states of (5.1.4). The stability of the front is determined by the

properties of the asymptotic states  $P_-$  and  $P_+$  with an associated asymptotic matrices

$$A_-(\lambda) = \begin{pmatrix} 0 & 1 & 0 \\ \frac{1}{D}(\lambda + 0.0262) & -\frac{c}{D} & \frac{1}{D}(0.4109) \\ -\frac{1}{c}(0.0484) & 0 & \frac{1}{c}(\lambda + 2.5553) \end{pmatrix}, \quad (5.2.39)$$

and

$$A_+(\lambda) = \begin{pmatrix} 0 & 1 & 0 \\ \frac{1}{D}(\lambda + 0.0262) & -\frac{c}{D} & \frac{1}{D}(0.4109) \\ -\frac{1}{c}(0.0484) & 0 & \frac{1}{c}(\lambda + 2.5553) \end{pmatrix}. \quad (5.2.40)$$

Similarly,  $A_{\pm}(\lambda)$  is non-hyperbolic if at least one of its eigenvalues has zero real part.

The curve of essential spectrum for the asymptotic state  $P_-$  is shown in Fig. 5.8b and Fig. 5.8c shows the essential spectrum of asymptotic state  $P_+$ . In both cases, the curves lie entirely in the left-half of the complex plane, meaning the spectral stability of the front is determined by the stability of its point spectrum.

Since the essential spectrum is determined by the asymptotic steady states  $P_{\pm}$ , essential spectrum instabilities of the front occur if one of the asymptotic steady states becomes unstable. The mechanisms of essential instability of fronts in reaction-diffusion systems are Turing, Hopf or Turing-Hopf bifurcations (Sandstede and Scheel, 2001). These bifurcations cause spatially periodic patterns behind or ahead the front depending on the direction of propagation. Such fronts are called modulated fronts. Our numerical simulations exhibit modulated travelling front for some parameter values of  $\psi$ . A typical example is shown in Fig. 5.9a for  $\psi = 0.3$ . The essential spectrum at  $P_+$  is the same as in Fig. 5.8c while the essential spectrum of  $P_-$  is shown in Fig. 5.9b, the curve lies on the right-half plane in the complex plane meaning the essential instability of the front occurs due to loss of stability of the asymptotic state  $P_-$  behind the front. The

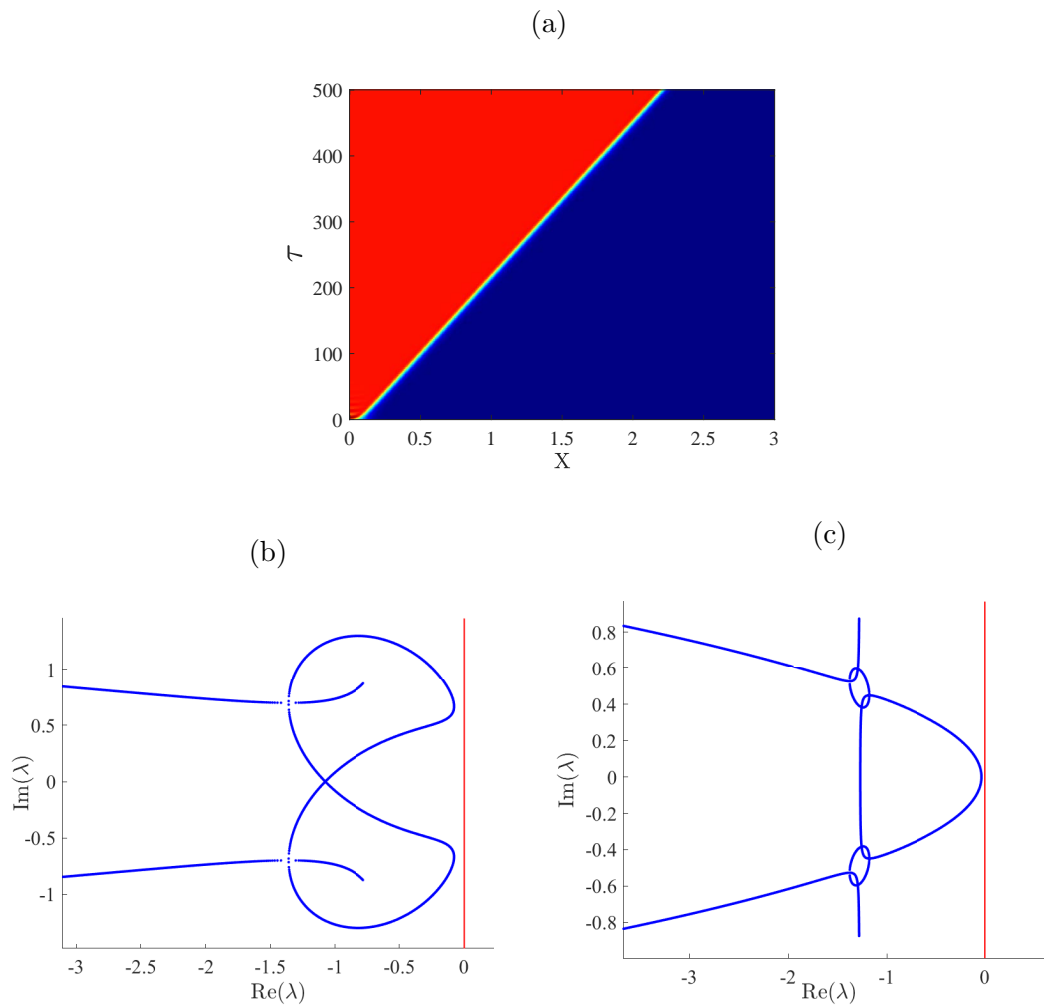


Figure 5.8: (a) A travelling front that connects homogeneous steady states  $V = -0.2891$  to  $V = -0.7141$ . (b)–(c) Essential spectra of the front for asymptotic state  $P_-$  and  $P_+$  with wave speed  $c = 0.0043$ .

onset of essential instability is due to a Hopf bifurcation in the dynamics of (2.2.6)–(2.2.7). As explained in Sandstede and Scheel (2001) at the onset of instability, patterns are created close to the steady state and this behaviour is observed in Fig. 5.9a.

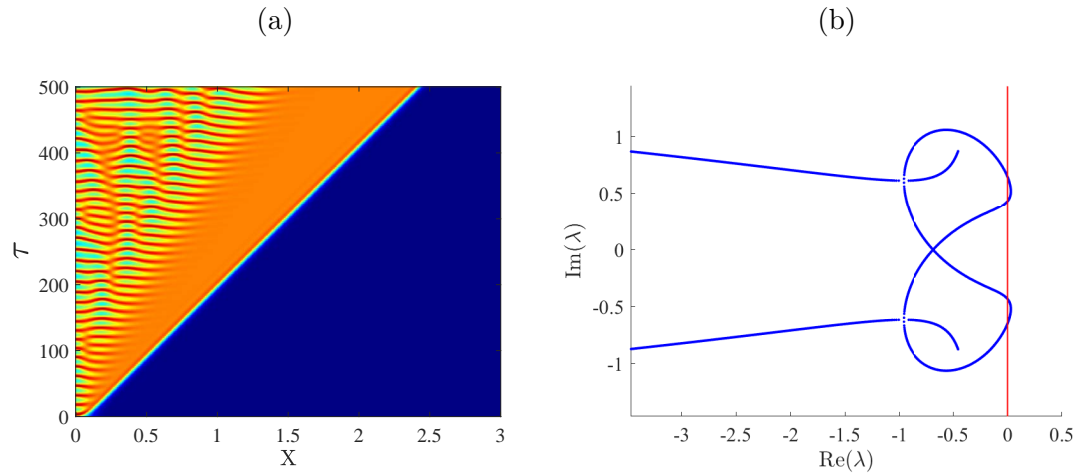


Figure 5.9: (a) A space-time plot of modulated front to (2.2.6)–(2.2.7) at  $(\bar{v}_1, \psi) = (-0.2466, 0.3)$  (b) The essential spectrum of the front for asymptotic state  $P_-$ .

### 5.3 Discussion

In this chapter we studied the TW solutions to the reaction-diffusion system (2.2.6)–(2.2.7). To describe the profile of the TW solutions, the system (2.2.6)–(2.2.7) is transformed via the TW ansatz to the system of ordinary differential equations called TWODE, (5.1.4). We established the existence of right moving travelling pulses and fronts numerically with the shooting method, and it was shown that the estimated wave speed in the TWODE system is very close to the wave speed observed in the numerical simulations.

We investigated the stability properties of homogeneous steady states, pulses, and fronts. The stability of these TWs was determined by the location of the spectrum of the linear operator  $\mathcal{L}$  in the complex plane. The spectrum of  $\mathcal{L}$ , denoted by  $\Sigma$ ,

---

can be partitioned into the essential spectrum  $\Sigma_{\text{ess}}$  and the point spectrum  $\Sigma_{\text{pt}}$ . For the homogeneous steady state the point spectrum is empty thus knowledge of the essential spectrum is sufficient to determine stability. Our results show that, as one would expect, the stability of the homogeneous steady-states is different for different parameter values.

Also, we found that the essential spectrum of the travelling pulse is contained in the left-half of the complex plane provided the asymptotic state is stable. Similarly, this occurs for the travelling front provided the asymptotic states that connect the front are both stable. For some parameter values of  $\psi$ , the travelling front is unstable due to instability of the asymptotic state behind the front. The onset of the essential instability occurred due to a Hopf bifurcation, and this results in spatiotemporal patterns close to the unstable steady state.

The condition that the essential spectrum is contained in the left-hand plane is not sufficient for the stability of travelling pulse and front since their point spectrum is not empty. Although we did not analyse the point spectrum in this thesis, it is important and remains for future studies.



## 6. Conclusion

This thesis aimed to study the collective dynamics of electrically coupled pacemaker SMCs. Our work is motivated by a model that describes stationary vasomotion of the vessel in arterial SMCs developed by [Gonzalez-Fernandez and Ermentrout \(1994\)](#). We proposed a reaction-diffusion system to model the electrical coupling of membrane potential between neighbouring cells. We presented a detailed analysis of spatiotemporal dynamics of the model in one-dimensional domain.

The local dynamics of the reaction-diffusion system (2.1.1)–(2.1.8) under variation of model parameters are analysed to study the electrical activity of an isolated SMC. We first studied the role of ion channels on the pacemaker dynamics of the SMC model. We found that the pacemaker activity persisted if the leak current conductance is blocked i.e.  $g_L = 0$ , but absent if the conductances for the  $\text{Ca}^{2+}$  and  $\text{K}^+$  currents are blocked i.e.  $g_{\text{Ca}} = 0$  and  $g_{\text{K}} = 0$  in turn. The implication of this is that the  $\text{Ca}^{2+}$  and  $\text{K}^+$  currents are required for the pacemaker activity. Existing studies have investigated the effect of mechanical stimulation on the pacemaker electrical activity of SMCs. We reproduced some of these behaviours in our pacemaker model by modulating parameters associated with the ion currents and gating variables, specifically the pressure-dependent parameters,  $v_1$  and  $v_6$ , respectively. The numerical results showed that the cell is either excitable, nonexcitable, or oscillatory depending on the model parameters.

The full reaction-diffusion system was reduced to two equations, we further simplified the model through dimensional analysis. The dynamics of the nondimensionalised version of the reduced model (2.2.1)–(2.2.2) in the absence of diffusion term with pressure dependent parameters,  $\bar{v}_1$  and  $\bar{v}_3$  (correspond to  $v_1$  and  $v_6$  in the full model), revealed that the behaviour of solutions observed is qualitatively similar to the full model. Thus the full model can be approximated by the reduced model, to further

---

our understanding of the model behaviours we performed phase plane analysis of the nondimensionalised model (2.2.6)–(2.2.7). It provided information on how the solutions of the system change due to variation of parameters.

We then performed numerical bifurcation analysis to gain more insights into physical significance of model parameters on dynamical behaviours of the model. With the aid of bifurcation diagrams, we showed that the reduced model preserved the dynamical properties of the full model qualitatively. We considered the transmural pressure-dependent parameters,  $\bar{v}_1$  and  $\bar{v}_3$ , as the main bifurcation parameters, and the rate constant for the kinetics of the open  $K^+$  channel and the Nerst reversal potential of the leak channel,  $\psi$  and  $v_L$ , as secondary bifurcation parameters. The model exhibited the two types of excitability for excitable cells depending on how parameters are varied. Variation of  $\bar{v}_1$  results in Type I excitability and Type II excitability is observed as  $\bar{v}_3$  is varied. We computed two-parameter bifurcation diagrams in different parameter planes to show transitions between the two types of excitability as parameters are varied. These analysis provided information on parameter values for which we can model SMC activity of either Type I or Type II excitability.

The numerical simulations of the nondimensionalised reaction-diffusion system showed a wide variety of spatiotemporal behaviours such as travelling pulses, travelling fronts and spatiotemporal chaos. We explored the mechanisms for the generation of patterns in the system, we have found that the spatiotemporal patterns observed occurred as a consequence of nonlinear dynamics of the reaction terms and effects of diffusion not due diffusion-driven instability as often the case in reaction-diffusion systems. Transitions between patterns are driven by the model parameters. For instance, the system transitions from stable travelling pulses to travelling fronts as the rate constant for the kinetics of the open  $K^+$  channel  $\psi$  is varied. We also showed that the shape of the initial perturbation does not affect the type of spatiotemporal patterns exhibited by the model. The precise mechanisms is not yet well understood therefore a more

---

comparison of the results to that of other gap junction coupling models could provide an insight as it has been previously established by Sherman and Rinzel (1991) and Medvedev and Kopell (2001) that desynchronised oscillations occur in gap junctions coupled pancreatic  $\beta$ -cells and neurons when the coupling strength is weak.

In addition, we examined the travelling wave solutions to the reaction-diffusion system. We established the existence of travelling pulses and fronts observed in our numerical simulations and showed how they relate to homoclinic and heteroclinic solutions in travelling wave coordinates. Lastly, we presented a detailed analysis of spectral stability of the travelling waves specifically we focused on the homogeneous waves, travelling pulses and travelling fronts. We computed the essential spectra of the travelling waves and as expected this depends on the parameter values.

In this thesis we have revealed that biologically important parameters  $\bar{v}_1$ ,  $\bar{v}_3$  and  $\psi$  affect the type of excitability and nature of the oscillations more generally in our pacemaker model. The results of the model agree with experimental observations on pacemaker behaviour of smooth muscle cells (Meyer et al., 1983; Harder, 1984) and neural cells (Connor, 1985; Ramirez et al., 2004). Harder (1984, 1987) observed in isolated small cerebral arteries that changes in transmural pressure cause smooth muscle cells in the arterial wall to become depolarised, followed by spontaneous electrical activity leading to constriction of the vessel's smooth muscles. It was reported that for small and large values of transmural pressure, the SMC is in a relaxation state, that is, there are no oscillations. For intermediate values of the transmural pressure oscillatory activity corresponding to EMC is observed. These behaviours are observed in our analysis of an isolated cell in Chapters 2 and 3 when the parameters,  $\bar{v}_1$  and  $\bar{v}_3$ , that govern transmural pressure in our model are varied, see Figs. 3.1c and 3.2a. Similar behaviours were observed in the experiment of Osol and Halpern (1988). Also, contraction of the vessel's smooth muscle is abolished when ion channel blockers are added (Harder, 1984). We observed similar results in our model analysis when the  $\text{Ca}^{2+}$  and  $\text{K}^+$  channels were

blocked, see Figs. 3.12 and 2.5c.

It is hoped the results may find application in models and experimental studies of physiological and pathophysiological responses in muscle cells. Certainly the observation that the dynamics of SMCs are particularly sensitive to parameter values has been utilised pharmacologically in therapeutics (Droogmans and Casteels, 1989; Pogátsa, 1994)

## 6.1 Future Work

In this thesis we have studied spatiotemporal dynamics in one spatial dimension, however the model can be extended to two-dimension setting. Hence, further studies can be conducted on two-dimensional patterns in our reaction-diffusion system.

Some experimental and computational studies of SMCs have shown that voltage-dependent inward  $\text{Na}^+$  current is important in EMC activity (Berra-Romani et al., 2005; Ulyanova, 2020), thus incorporating the  $\text{Na}^+$  current into our model to study its effect on pacemaker dynamics of SMCs is a future work.

# References

- R. Achouri. Travelling Wave Solutions. Technical report, The University of Manchester, 2016.
- R. R. Aliev, W. Richards, and J. P. Wikswo. A simple nonlinear model of electrical activity in the intestine. *J. Theor. Biol.*, 204:21–28, 2000.
- E. L. Allgower and K. Georg. *Introduction to Numerical Continuation Methods*. SIAM, Philadelphia, 2 edition, 2003.
- M. Banerjee and S. Banerjee. Turing instabilities and spatio-temporal chaos in ratio-dependent Holling Tanner model. *Math. Biosci.*, 236:64–76, 2012.
- R. Berra-Romani, M. P. Blaustein, and D. R. Matteson. TTX-sensitive voltage-gated  $\text{Na}^+$  channels are expressed in mesenteric artery smooth muscle cells. *Am. J. Physiol. Heart Circ. Physiol.*, 289:H137–H145, 2005.
- BLMCalifornia. Cadiz dunes wilderness, 2012. URL [https://en.wikipedia.org/wiki/Dune#/media/File:Cadiz\\_Wilderness\\_and\\_Valley.jpg](https://en.wikipedia.org/wiki/Dune#/media/File:Cadiz_Wilderness_and_Valley.jpg).
- R. I. Bogdanov. Versal deformations of a singular point of a vector field on the plane in the case of zero eigenvalues. *Funct. Anal. Its Appl.*, 9:144–145, 1975.
- R. Casteels, K. Kitamura, H. Kuriyama, and H. Suzuki. Excitation-contraction coupling in the smooth muscle cells of the rabbit main pulmonary artery. *J. Physiol.*, 271:63–79, 1977.
- C. Y. Cha, K. H. Earm, J. B. Youm, Eun Bok Baek, Sung Joon Kim, and Yung E. Earm. Electrophysiological modelling of pulmonary artery smooth muscle cells in the rabbits—special consideration to the generation of hypoxic pulmonary vasoconstriction. *Prog. Biophys. Mol. Biol.*, 96:399–420, 2008.

- 
- C. Chang, M. Duan, G. Sun, and Z. Jin. Cross-diffusion-induced patterns in an SIR epidemic model on complex network. *Chaos*, 30:013147, 2020.
- J. B. Chang and J. F. Ferrell Jr. Mitotic trigger waves and the spatial coordination of the *Xenopus* cell cycle. *Nature*, 500:603–607, 2013.
- M. A. J. Chaplain, G. D. Singh, and J. C. McLachlan. *On Growth and Form: Spatio-temporal Pattern Formation in Biology*. Wiley, 1999.
- T. R. Chay. Chaos in a three-variable model of an excitable cell. *Phys. D Nonlinear Phenom.*, 16:233–242, 1985.
- C. N. Chen and Y. Choi. Traveling pulse solutions to FitzHugh-Nagumo equations. *Cal. Var.*, 54:1–45, 2015.
- J. A. Connor. Neural Pacemakers and Rhythmicity. *Ann. Rev. Physiol.*, 47:17–28, 1985.
- J. A. Connor and C. F. Stevens. Prediction of repetitive firing behaviour from voltage clamp data on an isolated neurone soma. *J. Physiol.*, 213:31–53, 1971.
- P. Cornwell and C. K. R. T. Jones. On the Existence and Stability of Fast Traveling Waves in a Doubly Diffusive FitzHugh-Nagumo System. *SIAM J. Appl. Dyn. Syst.*, 17:754–787, 2018.
- A. Corrias and M. L. Buist. A quantitative model of gastric smooth muscle cellular activation. *Ann. Biomed. Eng.*, 35:1595–1607, 2007.
- A. Corrias and M. L. Buist. Quantitative cellular description of gastric slow wave activity. *Am. J. Physiol. Gastrointest. Liver. Physiol.*, 294:G989–G995, 2008.
- M. B. Cutlip and M. Shacham. The Numerical Method of Lines for Partial Differential Equations. *CACHE News*, 47:18–21, 1998.

- 
- P. De Kepper, V. Castets, E. Dulos, and J. Boissonade. Turing-type chemical patterns in the chlorite-iodide-malonic acid reaction. *Physica D*, 49:161–169, 1991.
- B. Deconinck and K. J. Nathan. Computing spectra of linear operators using the Floquet-Fourier-Hill method. *J. Comput. Phys.*, 219:296–321, 2006.
- E. J. Doedel, H. B. Keller, and J. P. Kernèvez. Numerical analysis and control of bifurcation problems (I): Bifurcation in infinite dimensions. *Internat. J. Bifur. Chaos Appl. Sci. Engrg.*, 1:493–520, 1991a.
- E. J. Doedel, H. B. Keller, and J. P. Kernèvez. Numerical analysis and control of bifurcation problems (II): Bifurcation in infinite dimensions. *Internat. J. Bifur. Chaos Appl. Sci. Engrg.*, 1:745–772, 1991b.
- E. J. Doedel, B. E. Oldeman, X. Wang, and C. Zhang. AUTO-07P : Continuation and Bifurcation Software for Ordinary Differential Equations. Technical report, Concordia University, Montreal, 2012.
- G. Drion, T O’Leary, and E Marder. Ion channel degeneracy enables robust and tunable neuronal Firing rates. *Proc. Natl. Acad. Sci. USA*, 112:E5361–E5370, 2015.
- G. Droogmans and R. Casteels. Electromechanical and pharmacomechanical coupling in vascular smooth muscle. In *Sperelakis N. (eds) Physiology and Pathophysiology of the Heart. Developments in Cardiovascular Medicine*, volume 90. Springer, Boston, MA, 1989.
- L. Duan, Q. Lu, and Q. Wang. Two-parameter bifurcation analysis of firing activities in the Chay neuronal model. *Neurocomputing*, 72:341–351, 2008.
- L. Eigentler and J. A. Sherratt. Spatial self-organisation enables species coexistence in a model for savanna ecosystems. *J. Theor. Biol.*, 487, 2020.

- 
- K. Engelborghs, T. Luzyanina, and D. Roose. Numerical bifurcation analysis of delay differential equations using DDE-Biftool. *ACM Trans. Math. Soft.*, 28:1–21, 2002.
- B. Ermentrout. *Simulating, Analyzing, and Animating Dynamical Systems: A Guide to XPPAUT for Researchers and Students*. SIAM Press, Philadelphia, 2002.
- B. Ermentrout and D. Terman. *Foundations of Mathematical Neuroscience*. Springer, 2008.
- B. Ermentrout, J. W. Wang, J. Flores, and A. Gelperin. Model for transition from waves to synchrony in the olfactory lobe of *Limax*. *J. Comput. Neurosci.*, 17:365–383, 2004.
- R. Fitzhugh. Impulses and Physiological States in Theoretical Model of Nerve Membrane. *Biophys. J.*, 1:445–466, 1961.
- H. Fujii and I. Tsuda. Neocortical gap junction-coupled interneuron systems may induce chaotic behaviour itinerant among quasi-attractors exhibiting transient synchrony. *Neurocomputing*, 58-60:151–157, 2004.
- J. M Gonzalez-Fernandez and B. Ermentrout. On the Origin and Dynamics of the Vasomotion of Small Arteries. *Math. Biosci.*, 119:127–167, 1994.
- J. M. González-Miranda. Pacemaker dynamics in the full Morris-Lecar model. *Commun. Nonlinear Sci. Numer. Simul.*, 19:3229–3241, 2014.
- W. Govaerts and B. Sautois. The Onset and Extinction of Neural Spiking: A Numerical Bifurcation Approach. *J. Comput. Neurosci.*, 18:265–274, 2005.
- W. Govaerts, Y. A. Kuznetsov, V. De Witte, A Dhooge, H G E Meijer, W Mestrom, A M Riet, and B Sautois. *MATCONT and CL MATCONT: Continuation toolboxes in matlab*. Gent University and UtrechtUniversity, 2011.



- 
- C. Hahn and M. A. Schwartz. Mechanotransduction in vascular physiology and atherogenesis. *Nature Rev. Mol. Cell Biol.*, 10:53–62, 2009.
- D. R. Harder. Pressure-dependent membrane depolarization in cat middle cerebral artery. *Circ Res*, 55:197–202, 1984.
- D. R. Harder. Pressure-induced myogenic activation of cat cerebral arteries is dependent on intact endothelium. *Circ Res*, 60:102–107, 1987.
- H. Hartle and R. Wackerbauer. Transient chaos and associated system-intrinsic switching of spacetime patterns in two synaptically coupled layers of Morris-Lecar neurons. *Phys. Rev. E*, 96:032223, 2017.
- R. Hiptmair, C. Schwab, H. Harbrecht, V. Gradinaru, and A. Chernov. *Numerical Methods for Partial Differential Equations Numerical Methods for PDEs*. ETH Zurich, 2010.
- M. W. Hirsch, S. Smale, and R. L. Devaney. *Differential Equations, Dynamical Systems, and an Introduction to Chaos*. Elsevier Science, New York, 3rd edition edition, 2013.
- A. L. Hodgkin. The local electric changes associated with repetitive action in a non-medullated axon. *J. Physiol.*, 107:165–181, 1948.
- A. L. Hodgkin and A. F. Huxley. A quantitative description of membrane current and its application to conduction and excitation in nerve. *J. Physiol.*, 117:500–544, 1952.
- E. M. Izhikevich. *Dynamical systems in neuroscience : the geometry of excitability and bursting*. MIT Press, Cambridge, 2007.
- J. C. B Jacobsen, C. Aalkjær, H. Nilsson, V. V. Matchkov, J. Freiberg, and N. Holstein-Rathlou. A model of smooth muscle cell synchronization in the arterial wall. *Am. J. Physiol. Heart Circ. Physiol.*, 293:H229–H237, 2007.

- 
- Y. F. Jia, Y. L. Cai, H. B. Shi, S. M. Fu, and W. M. Wang. Turing patterns in a reaction-diffusion epidemic model. *Int. J. Biomath.*, 2:3087–3107, 2018.
- B. Johansson and A. P. Somlyo. Electrophysiology and excitation-contraction coupling. In *Handbook of Physiology*, D. H. Bohr, A. P. Somlyo, H. V. Sparks, Jr., S. R. Geiger II, chapter 12, pages 301–323. Waverly Press, Baltimore, 1980.
- V. John. *Numerical Methods for Partial Differential Equations*. Weierstrass Institute for Applied Analysis and Stochastics, 2013.
- C. K. R. T. Jones. Stability of the Travelling Wave Solution of the Fitzhugh-Nagumo System. *Trans. Am. Math.*, 286:431–469, 1984.
- T. Kapitula and K. Promislow. *Spectral and dynamical stability of nonlinear waves*. Springer, New York, 2013.
- A. L. Kay and J.A. Sherratt. On the persistence of spatiotemporal oscillations generated by invasion. *IMA J. Appl. Math.*, 63:199–216, 1999.
- J Keener and J Sneyd. *Mathematical Physiology*, volume 8/1 of *Interdisciplinary Applied Mathematics*. Springer New York, New York, NY, 2009.
- K. Keplinger and R. Wackerbauer. Transient spatiotemporal chaos in the Morris-Lecar neuronal ring network. *Chaos*, 24:013126, 2014.
- M Koenigsberger, R Sauser, M Lambole, J. L Bény, and J. J. Meister.  $\text{Ca}^{2+}$  dynamics in a population of smooth muscle cells: Modeling the recruitment and synchronization. *Biophys. J.*, 87:92–104, 2004.
- Y. A. Kuznetsov. *Elements of Applied Bifurcation Theory*. Springer, New York, 3 edition, 1995.

- 
- J. Lafranceschina and R. Wackerbauer. Impact of weak excitatory synapses on chaotic transients in a diffusively coupled Morris-Lecar neuronal network. *Chaos*, 25:013119, 2014.
- V. Ledoux, S. J. A. Malham, and V. Thümmler. Grassmannian spectral shooting. *Math. Comp.*, 79:2323–2332, 2010.
- C. Liu, L. Chang, Y. Huang, and Z. Wang. Turing patterns in a predator-prey model on complex networks. *Nonlinear Dyn.*, 99:3313–3322, 2020.
- J. D. Logan. *Applied Mathematics*. John Wiley & Sons, Inc., New Jersey., 3rd edition, 2006.
- N. A. Lusamvuku, R. Sercombe, P. Aubineau, and J. Seylaz. Correlated electrical and mechanical responses of isolated rabbit pial arteries to some vasoactive drugs. *Stroke*, 10:727–732, 1979.
- D. P. McCobb and M. L. Zeeman. Bridging Between Experiments and Equations: A Tutorial on Modeling Excitability. In *Computational Neuroendocrinology*, chapter 1, pages 1–79. John Wiley and Sons, 2016.
- M. J. Mclean and N. Sperlakis. Electrophysiological recordings from spontaneously contracting reaggregates of cultured vascular smooth muscle cells from chick embryos. *Exp. Cell. Res.*, 104:309–318, 1977.
- G. S. Medvedev and N. Kopell. Synchronization and transient dynamics in the chains of electrically coupled Fitzhugh-Nagumo oscillators. *SIAM J. Appl. Math.*, 61:1762–1801, 2001.
- H. Meinhardt. *The Algorithmic Beauty of Sea Shells*. Springer, Heidelberg, New York, 3rd edition edition, 2003.
- J. D. Meiss. *Differential dynamical systems*. SIAM, Philadelphia, 1 edition, 2007.

- 
- J. Merkin and M. A. Sadiq. The propagation of travelling waves in an open cubic autocatalytic chemical system. *IMA J. Appl. Math.*, 57:273–309, 12 1996.
- J. H. Merkin, V. Petrov, S. K. Scott, and K. Showalter. Wave-induced chaos in a continuously fed unstirred reactor. *J. Chem. Soc. Faraday Trans.*, 92(16):2911–2918, 1996.
- J. U. Meyer, L. Lindbom, and M. Intaglietta. Pacemaker induced diameter oscillations at arteriolar bifurcations in skeletal muscle. *Prog. Appl. Microcirc.*, 12:264–269, 1983.
- R. N. Miftakhov, G. R. Abdusheva, and D. L. Wingate. Model predictions of myoelectrical activity of the small bowel. *Biol cybern*, 74:167–79, 1996.
- G. K Moe, W. C. Rheinbolt, and J. A. Abildskov. A computer model of atrial fibrillation. *Amer. Heart. J.*, 67:200–220, 1964.
- C. Morris and H. Lecar. Voltage Oscillations in the Barnacle Giant Muscle Fiber. *Biophys. J.*, 35:193–213, 1981.
- J. D. Murray. *Mathematical biology. II Spatial models and biomedical applications*. Springer, 2003.
- J. Nagumo, S. Arimoto, and S. Yoshizawa. An Active Pulse Transmission Line Simulating Nerve Axon. *Proc. IRE*, 50:2061–2070, 1962.
- M. T. Nelson, B. Patlak, J. F. Worley, and N. B. Standen. Calcium channels, potassium channels, and voltage dependence of arterial smooth muscle tone. *Am. J. Physiol.*, 259:C3–C18, 1990.
- L. Olsen-Kettle. Numerical solution of partial differential equations, 2011.
- M. Or-Guil, J. Krishnan, I. G. Kevrekidis, and M. Bär. Pulse bifurcations and instabilities in an excitable medium: Computations in finite ring domains. *Phys. Rev. E*, 64:046212, 2001.

- 
- G. J. Osol and W. Halpern. Spontaneous vasomotion in pressurized cerebral arteries from genetically hypertensive rats. *Am. J. Physiol.*, 254 1 Pt 2:H28–33, 1988.
- S. Pal, M. Banerjee, and S. Ghorai. Spatio-temporal pattern formation in Holling-Tanner type model with nonlocal consumption of resources. *Int. J. Bifurcat. Chaos*, 29:1930002, 2019.
- S. V. Pandit and F. Jalife. Rotors and the dynamics of cardiac fibrillation. *Circ. Res.*, 112:849–862, 2013.
- M. R. Paul, K.-H. Chiam, M.C. Cross, P.F. Fischer, and H.S. Greenside. Pattern formation and dynamics in Rayleigh–Bénard convection: numerical simulations of experimentally realistic geometries. *Physica D*, 184:114–126, 2003.
- J. E. Pearson. Complex patterns in a simple system. *Science A*, 261:189–192, 1993.
- S. Perez-Londoño, G. Olivar, and J. Mora-Florez. Zero-Hopf bifurcation analysis on power system dynamic stability. In *2010 IEEE/PES Transmission and Distribution Conference and Exposition: Latin America (T D-LA)*, pages 765–769, 2010.
- S. K. Petrov, V. and Scott and K. Showalter. Excitability, wave reflection, and wave splitting in a cubic autocatalysis reaction-diffusion system. *Proc. R. Soc. Lond. A.*, 347:631–642, 1994.
- G. Pogátsa. Altered responsiveness of vascular smooth muscle to drugs in diabetes. In *Szekeres L., Papp J.G. (eds) Pharmacology of Smooth Muscle. Handbook of Experimental Pharmacology*, pages 693–712. Springer, Berlin, Heidelberg, 1994.
- Y. C. Poh, A. Corrias, N. Cheng, and M. L. Buist. A quantitative model of human jejunal smooth muscle cell electrophysiology. *PLoS ONE*, 7:e42385, 2012.
- J. D.M. Rademacher, B. Sandstede, and A. Scheel. Computing absolute and essential spectra using continuation. *Physica D*, 229:166–183, 2007.

- J. M. Ramirez, A. K. Tryba, and F. Peña. Pacemaker neurons and neuronal networks: An integrative view. *Curr. Opin. Neurobio.*, 14:665–674, 2004.
- K. Ran, Z. Yang, Y. Zhao, and X. Wang. Transmural pressure drives proliferation of human arterial smooth muscle cells via mechanism associated with NADPH oxidase and Survivin. *Microvasc. Res.*, 126:103905, 2019.
- N. M. Ratan. Importance of Ion Channels in the body, 2018. URL <http://www.news-medical.net/health/importance-of-Ion-Channels-in-the-Body.aspx>.
- W. E. Reynolds, J. E. Pearson, and S. Ponce-Dawson. Dynamics of self-replicating patterns reaction-diffusion systems. *Phys. Rev. Lett.*, 72:2797–2800, 1994.
- S. Rihana, J. Terrien, G. Germain, and C. Marque. Mathematical modeling of electrical activity of uterine muscle cells. *Med. Biol. Eng. Comput.*, 47:665–675, 2009.
- J. Rinzel and G. B. Ermentrout. Analysis of neural excitability and oscillations. In *Koch C. , Segev I. 2nd (Eds), Methods in Neuronal Modeling: From Ions to Network*, pages 251–292. MIT Press, London, 1999.
- F. Sala and A. Hernandez-Cruz. Calcium diffusion modeling in a spherical neuron. Relevance of buffering properties. *Biophys. J.*, 57:313–324, 1990.
- B. Sandstede. Stability of travelling waves. In *Fiedler, B. (Ed.), Handbook of Dynamical Systems II*, pages 983–1055. Elsevier, Amsterdam, 2002.
- B. Sandstede and A. Scheel. Essential instabilities of fronts: bifurcation, and bifurcation failure. *Dynamical Systems*, 16, 2001.
- W. E. Schiesser and G. W. Griffiths. *A Compendium of Partial Differential Equation Models*. Cambridge University Press, 2009.
- J. Schnakenberg. Simple chemical reaction systems with limit cycle behaviour. *J. Theo. Biol.*, 81:389–400, 1979.

- 
- M. A. Shaikh, D. J. N. Wall, and T. David. Macro-scale phenomena of arterial coupled cells: a massively parallel simulation. *J. R. Soc. Interface*, 9:972–987, 2011.
- A. Sherman and J. Rinzel. Model for synchronization of pancreatic  $\beta$ -cells by gap junction coupling. *Biophys. J.*, 59:547–559, 1991.
- H. B. Shi and S. Ruan. Spatial, temporal and spatiotemporal patterns of diffusive predator-prey models with mutual interference. *IMA J. Appl. Math.*, 80:1534–1568, 2015.
- A. Shilnikov. Complete dynamical analysis of a neuron model. *Nonlinear Dyn*, 68:305–328, 2012.
- J. Sneyd, J. Keizer, and M. J. Sanderson. Mechanisms of calcium oscillations and waves: a quantitative analysis. *The FASEB Journal*, 9:14631472, 1995.
- F. Takens. Singularities of vector fields. *Publi. Math. IHES*, 43:47–100, 1974.
- W. C. Tong, C. Y. Choi, S. Karche, A. V. Holden, H. Zhang, and M. J. Taggart. A computational model of the ionic currents,  $\text{Ca}^{2+}$  dynamics and action potentials underlying contraction of isolated uterine smooth muscle. *PLoS ONE*, 6:e18685, 2011.
- L. N. Trefethen and M. Embree. *Spectra and pseudospectra: the behavior of nonnormal matrices and operators*. Princeton University Press, Princeton, 2005.
- K. Tsumoto, H. Kitajima, T. Yoshinaga, K. Aihara, and H. Kawakami. Bifurcations in Morris-Lecar neuron model. *Neurocomputing*, 69:293–316, 2006.
- A. M. Turing. The Chemical Basis of Morphogenesis. *Philos. Trans. R. Soc. B*, 237:37–72, 1952.
- A. V. Ulyanova. Excitability of vascular smooth muscle. In Mani T. Valarmathi, editor, *Muscle Cells*, chapter 2. Intech Open, Rijeka, 2020.

- 
- X. J. Wang and G. Buzsáki. Gamma oscillation by synaptic inhibition in a hippocampal interneuronal network model. *J. Neurosci.*, 16:6402–6413, 1996. doi: J.Neurosci.
- W. Warby. Amur leopard (*panthera pardus orientalis*) at colchester zoo, 2015. URL [https://en.wikipedia.org/wiki/Amur\\_leopard#/media/File:Panthera\\_pardus\\_orientalis\\_Colchester\\_Zoo\\_\(1\).jpg](https://en.wikipedia.org/wiki/Amur_leopard#/media/File:Panthera_pardus_orientalis_Colchester_Zoo_(1).jpg).
- M. Xing, X. Song, Z. Yang, and Yong Chen. Bifurcations and excitability in the temperature-sensitive Morris–Lecar neuron. *Nonlinear Dyn*, 2020.
- H. Xu, M. Sun, and X. Zhao. Turing mechanism underlying a branching model for lung morphogenesis. *PLoS One*, 12:e0174946, 2017.
- H. W. Yang, S. R. Collins, and T. Meyer. Locally excitable Cdc42 signals steer cells during chemotaxis. *Nat. Cell. Biol.*, 18:191–201, 2016.
- T. Zhang and H. Zang. Delay-induced Turing instability in reaction-diffusion equations. *Phys. Rev. E*, 90:052908, 2014.
- Z. Zhao and H. Gu. Transitions between classes of neuronal excitability and bifurcations induced by autapse. *Scientific Reports*, 7:6760, 2017.



# A. Appendix

## A.1 Statement of Contribution

DRC 16



MASSEY UNIVERSITY  
GRADUATE RESEARCH SCHOOL

### STATEMENT OF CONTRIBUTION DOCTORATE WITH PUBLICATIONS/MANUSCRIPTS

We, the candidate and the candidate's Primary Supervisor, certify that all co-authors have consented to their work being included in the thesis and they have accepted the candidate's contribution as indicated below in the *Statement of Originality*.

Name of candidate:	Hammed Olawale Fatoyinbo	
Name/title of Primary Supervisor:	Ass. Prof. Bruce van Brunt	
Name of Research Output and full reference:		
Fatoyinbo, H.O., Brown, R.G., Simpson, D.J.W., van Brunt, B. Numerical Bifurcation Analysis of Pacemaker Dynamics in a Model of Smooth Muscle Cells. <i>Bull. Math. Biol.</i> 82, 95 (2020).		
In which Chapter is the Manuscript /Published work:	Chapter 3	
Please indicate:		
<ul style="list-style-type: none"> <li>The percentage of the manuscript/Published Work that was contributed by the candidate:</li> </ul>	80%	
and		
<ul style="list-style-type: none"> <li>Describe the contribution that the candidate has made to the Manuscript/Published Work:</li> </ul>	The candidate did the bifurcation analysis and drafted the manuscript	
For manuscripts intended for publication please indicate target journal:		
Candidate's Signature:	Hammed Fatoyinbo	
Date:	10/12/2020	
Primary Supervisor's Signature:		
Date:	11 December 2020	

(This form should appear at the end of each thesis chapter/section/appendix submitted as a manuscript/ publication or collected as an appendix at the end of the thesis)

GRS Version 4– January 2019

The codes provided below are available at [github.com/hamfat](https://github.com/hamfat)

## A.2 AUTO-07p Code

To produce the codimension-one and codimension-two bifurcation diagrams for the nondimensionalised model in AUTO continuation software. The followings files are required:

1. **dimless.f**: This file contains model equations, parameter values and initial conditions.
2. **c.dimless**: This file contains AUTO constant parameters
3. **dimless.auto**: This plots the bifurcation diagrams

```
!-----
! "dimless.f"
!-----

SUBROUTINE FUNC(NDIM,U,ICP,PAR,IJAC,F,DFDU,DFDP)
!
!   -----
!
!   IMPLICIT NONE
!
!   INTEGER, INTENT(IN) :: NDIM, ICP(*), IJAC
!
!   DOUBLE PRECISION, INTENT(IN) :: U(NDIM), PAR(*)
!
!   DOUBLE PRECISION, INTENT(OUT) :: F(NDIM)
!
!   DOUBLE PRECISION, INTENT(INOUT) :: DFDU(NDIM,NDIM), DFDP(NDIM,*)
!
!   DOUBLE PRECISION V, N, v1, vca, vL, vK, v2, v4, gca, gL, gK, phin
!
!   DOUBLE PRECISION minf, v3, ninf, C, psi
!
!
!   V = U(1)
!
!   N = U(2)
```

---

```

! bifurcation parameters
    v1 = PAR(1)
    v3 = PAR(2)
! model parameters
    vca = 80.d0;
    vL = (-70.d0/vca);
    vK = (-90.d0/vca);
    v2 = (25.d0/vca);
!v3 = (-11.d0/vca);
    v4 = (14.5d0/vca);
gK = 3.1416E-13;
    gca = (1.57E-13/gk);
    gL = ((7.854E-14)/gk);
C = 1.9635E-14;
    phin = 2.664d0;
psi=((C*phin)/gk)
!model equations and auxiliary functions
    minf = (0.5d0*(1+tanh((V-v1)/v2)));
    ninf = 0.5d0*(1+tanh((V-v3)/v4));
    F(1) = -(gL*(V-vL)+N*(V-vK)+gca*minf*(V-1.d0));
    F(2) = psi*cosh((V-v3)/(2.d0*v4))*(ninf-N);
    END SUBROUTINE FUNC
    SUBROUTINE STPNT(NDIM,U,PAR,T)
!
    -----
    IMPLICIT NONE
    INTEGER, INTENT(IN) :: NDIM
    DOUBLE PRECISION, INTENT(INOUT) :: U(NDIM),PAR(*)

```

```
DOUBLE PRECISION, INTENT(IN) :: T
! initial values for the bifurcation parameters
PAR(1)=-0.5d0
PAR(2)=-0.1375
! initial conditions
U(1)=-0.18484d0
U(2)=0.37227d0
END SUBROUTINE STPNT
SUBROUTINE BCND
END SUBROUTINE BCND
SUBROUTINE ICND
END SUBROUTINE ICND
SUBROUTINE FOPT
END SUBROUTINE FOPT
SUBROUTINE PVLS
END SUBROUTINE PVLS
!-----
! "c.dimless"
!-----
NDIM= 2, IPS =1, IRS =0, ILP = 1
ICP = [1]
NTST= 500 NCOL= 4, IAD = 3, ISP = 1, ISW = 1, IPLT= -1, NBC= 0, NINT= 0
NMX= 1000, NPR= 50, MXBF= 5, IID = 2, ITMX= 8, ITNW= 7, NWTN= 3, JAC= 0
EPSL= 1e-7, EPSU = 1e-7, EPSS = 1e-5
DS = 0.02, DSMIN= 0.0001, DSMAX= 0.005, IADS= 1
NPAR= 25, THL = {11: 0.0}, THU = {}
```

```

!-----
! "dimless.auto" file
! run "auto dimless.auto" in the terminal
!-----

r1=run('dimless')
#r1.writeRawFilename('eq_curve.dat')
r2=run(r1("HB1"),ISP=2,ICP=[1,11],IPS=2)
r2.writeRawFilename('period_curve.dat')
r10=r1+r2

!plot(r10) produce the codimension-1 bifurcation diagram
plot(r10)
print "\n***curve of HB***"
r3=run(r1("HB1"),ISW=2,ICP=[1,2],STOP=[],NMX=2000)+...
...run(r1("HB1"),ISW=2,ICP=[1,2],STOP=[],DS="-",NMX=2000)
#r3.writeRawFilename('HB_curve.dat')
print "\n***saddle-node curves***"
r4=run(r1("LP1"),ISW=2,ICP=[1,2],STOP=[],NMX=500)+...
...run(r1("LP1"),ISW=2,ICP=[1,2],STOP=[],NMX=500,DS='-')
r4.writeRawFilename('SN_curve.dat')
print "\n***curve of periodic orbit***"
t2=run(r1("HB1"),ICP=[1,11],ISW=-1,IPS=2)
t3=run(t2("LP1"),ISW=2,ICP=[1,2,11])
t4=run(t3,NMX=1000,DS='-')+run(t3,NMX=1000)
t4.writeRawFilename('LPC_curve.dat')
plot t4
print "\n***curve of homoclinic orbit***"

```

```
r9=run(r1("HB1"),ISP=2,ICP=[1,11],IPS=2,UZSTOP={11:2500})
print "\n***homoclinic_Highper***"
rHigPer =run(r9("UZ1"),ICP=[1,2],DS='-',NMX=1000)...
...+run(r9("UZ1"),ICP=[1,2],NMX=1000)
rHigPer.writeRawFilename('HOM_curve.dat')
print "\n***codimension-2 diagram***"
r12=r3+r4+t4+rHigPer
r12.writeRawFilename('codimension-2.dat')
plot(r12)
print "\n***Clean the directory***"
clean()
```

## A.3 MATLAB Code

```
%model parameters
global d glbar gkbar gcabar vlbar vkbar vcabar v1 v2 v3 v4 psi a b
d=.0001; %diffusion coefficient
v1=-0.245;
v2=0.3125;
v3=-0.1405;
v4=0.1812;
vkbar=-1.125;
vcabar=1.0;
vlbar=-0.875;
gkbar=1.0;
glbar=0.25;
gcabar=0.4997;
```



```
figure(1)
    %subplot(1,2,1);
mesh(T,X,V,'FaceLighting','gouraud','LineWidth',0.5)
xlabel('\itT\rm')
    ylabel('\itX\rm')
zlabel('\itV\rm')
set ( gca, 'xdir', 'reverse' )
colorbar
subplot(1,2,2);
mesh(T,X,N,'FaceLighting','gouraud','LineWidth',0.5)
xlabel('\itT\rm')
ylabel('\itX\rm')
zlabel('\itN\rm')
set ( gca, 'xdir', 'reverse' )
f=figure(3);
imagesc(x,tsol,V');
%title(sprintf('$v_1$=%4.4f', v1),'interpreter', 'latex')
title(['v_1=',num2str(v1)])
ylabel('T','FontSize', 20, 'interpreter', 'latex')
xlabel('X','FontSize', 20, 'interpreter', 'latex')
colorbar
f.CurrentAxes.YDir='normal';
colormap jet
figure(4)
plot(x,V(:,550))
ylabel('V','FontSize', 20, 'LineWidth', 1.5, 'interpreter', 'latex')
xlabel('X','FontSize', 20, 'LineWidth', 1.5, 'interpreter', 'latex')
```



```

%%%%%%%%%% ODEs %%%%%%%%%%
function xdot = myworkinternal(~,x,M)
global d glbar gkbar gcabar vlbar vkbar v1 v2 v3 v4 psi a b vcabar
V = x(1:M);
N = x(M+1:end);
dx=(b-a)/(M-1);
mu=d/dx^2;
dVdt = zeros(M,1);
dNdt = zeros(M,1);
for i=1:M
    minf=0.5*(1+tanh((V(i)-v1)/v2));
    ninf=0.5*(1+tanh((V(i)-v3)/v4));
    lambda_v=cosh((V(i)-v3)/(2*v4));
    if i==1
dVdt(i)= 2*mu*(V(i+1)-V(i))-(glbar*(V(i)-vlbar)+gkbar*N(i)*(V(i)-vkbar)+...
...gcabar*minf*(V(i)-vcabar));
dNdt(i)= psi*lambda_v*(ninf-N(i));
    end
    if i==M
dVdt(i)= 2*mu*(V(i-1)-V(i))-(glbar*(V(i)-vlbar)+gkbar*N(i)*(V(i)-vkbar)+...
...gcabar*minf*(V(i)-vcabar));
dNdt(i)= psi*lambda_v*(ninf-N(i));
    end
    if i>1 && i<M
dVdt(i)= mu*(V(i+1)-2*V(i)+V(i-1))-(glbar*(V(i)-vlbar)...

```

```

...+gkbar*N(i)*(V(i)-vkbar)+gcabar*minf*(V(i)-vcabar));
dNdt(i)= psi*lambda_v*(ninf-N(i));
    end
end
xdot = [dVdt;dNdt];
end
%%%%%%%%%%%%%%%%%%%%%%%%%%%%%%%%%%%%%%%%%%%%%%%%%%%%%%%%%%%%%%%%%%%%%%%% functions used to obtain the steady state V0 and N0 above %%%%%%%%%
function ica = I_Ca(V)
global gcabar vcabar
    ica=gcabar * m_inf(V)*(V - vcabar);
end
function ik = I_K(V,N)
global gkbar vkbar
    ik=gkbar * N * (V - vkbar);
end
function ileak = I_Leak(V)
global glbar vlbar
    ileak=glbar* (V - vlbar);
end
function VN = dimless(X)
global psi
    V=X(1);
    N=X(2);
    VN(1) = - I_Leak(V) - I_K(V,N) - I_Ca(V);
    VN(2) = psi*lamda(V)*(n_inf(V) - N) ;
end
function out = m_inf(V)

```

```
global v1 v2
out = 0.5*(1+tanh((V-v1)/v2));
end
function out =n_inf(V)
global v3 v4
out = 0.5*(1+tanh((V-v3)/v4));
end
function out =lamda(V)
global v3 v4
out = cosh((V-v3)/(2*v4));
end
```